INTEGRATION OF PRODUCT LIFECYCLE BEHAVIOR INTO COMPONENT DESIGN, MANUFACTURING AND PERFORMANCE ANALYSIS TO REALIZE A DIGITAL TWIN REPRESENTATION THROUGH A MODEL-BASED FEATURE INFORMATION NETWORK

by

Saikiran Gopalakrishnan

A Dissertation

Submitted to the Faculty of Purdue University

In Partial Fulfillment of the Requirements for the degree of

Doctor of Philosophy

School of Aeronautics and Astronautics

West Lafayette, Indiana

May 2022

THE PURDUE UNIVERSITY GRADUATE SCHOOL

STATEMENT OF COMMITTEE APPROVAL

Dr. Michael D. Sangid, Chair

School of Aeronautics and Astronautics

Dr. Nathan W. Hartman

Department of Computer Graphics Technology

Dr. William Crossley

School of Aeronautics and Astronautics

Dr. Weinong Chen

School of Aeronautics and Astronautics

Approved by:

Dr. Gregory A. Blaisdell

Dedicated to my loving parents Usha Gopalakrishnan and Ramakrishnan Gopalakrishnan for their unconditional love, sacrifice and support which has made this thesis possible.

विद्या ददाति विनयं

True knowledge begets humility

ACKNOWLEDGMENTS

First and foremost, I would like to sincerely thank my advisor Dr. Michael Sangid, for mentoring and providing constant support throughout my time here at Purdue University. This journey has been filled with excitement and challenges, with many ups and downs. Throughout the journey, Professor Sangid has always been available to discuss and talk with me, constantly providing words of reassurance and motivation, which has ultimately enabled me to successfully complete my PhD work. I thoroughly admire his passion, dedication and commitment towards research and his students. My weekly meetings with him involved countless number of thought-stimulating discussions and brainstorming sessions which has eventually shaped into contributions presented in this thesis. I hope to carry forward all the valuable research and life skills that I have learnt from Dr. Sangid into the next stages of my life.

This PhD work would not have been possible without the funding provided by numerous organizations. I would like to thank and acknowledge the funding source: National Science Foundation under CMMI 16-51956 and MxD 15-11-08 (Capturing Product Behavioral and Contextual Characteristics through a Model-based Feature Information Network). Additionally, my work was also supported via grants received by Dr. Sangid: Northrop Grumman gift to support digital twin research and IN-MaC (Indiana Manufacturing Competitiveness Center) Faculty Fellow award. I would also like to thank Dr. Sangid for nominating me for Bilsland fellowship which supported the last year of my PhD and for providing me with RA throughout the past 5 years.

My PhD work has involved collaborations and mentorship from several members from Purdue University, outside my lab group. Firstly, I want to thank my doctoral committee members: Dr. Nathan Hartman, Dr. William Crossley and Dr. Weinong Chen for their time and inputs in shaping up this thesis. I want to extend my thanks Dr. Nathan Hartman for co-advising a large portion of my PhD. Next, I would like to extend my thanks to Prof. Rosemary Astheimer and Kevin Del Re from Dr. Hartman's group for the partnership during the MxD 15-11 project. I would also like to thank Alex Miller and Ramon Alvarez from Dr. Hartman's group for their initial work in developing the CAD-based plug-in tool.

I want to extend thanks to all the team members from MxD 15-11-08 project. The help from Daniel Campbell (Capvidia) for supporting the QIF-based schema development, David

Seidensticker (MSC Software) for implementation of structural analysis tool (using MSC's APIs) and materials database integration, and Tom Searles and Clay Records (Materials Data Management) for Granta MI implementation played a crucial role in the framework building stages of my PhD. Additionally, the software license extensions from Granta MI and Capvidia beyond the project duration is greatly appreciated.

I want to extend my thanks to members of the MAI-FEP bulk residual stress program, under principal investigator, Dr. Vasisht Venkatesh (Pratt & Whitney) and program manager, Dr. T.J. Turner (Air Force Research Laboratory) who provided us with the residual stress dataset which was used in Chapter 3 of this work. We would also like to thank Timothy Gabb and Ignacy Telesman from NASA GRC for providing the uniaxial tensile test data for LSHR, which were utilized for crystal plasticity work for crystal plasticity model calibration in Chapter 5.

I was fortunate to be surrounded with a fantastic group of researchers in my lab. I want to thank the current and past members of the ACME^2 lab group for keeping up a positive environment which has played an important role in conducting successful research. I want to extend my sincere thanks to my colleague and postdoc, Dr. Ritwik Bandyopadhyay, who has not only been a great mentor but also a great friend. He has played a significant role in guiding me, both personally and professionally. I want to acknowledge Ritwik for collaborating and mentoring me for the crystal plasticity work presented in Chapter 5 of the thesis. I would like to thank undergraduate researchers Brian Chen, Aidan Molnar, and Ryoma Kawakami for providing valuable programming support during the development of MFIN framework. Beyond work, I have had some great memories with the lab group, which I will cherish for a very long time. The coffee sessions with the lab members will truly be missed.

I have been fortunate to have a large group of friends who have been a great support system. I want to extend my sincere thanks to Sidharth, Sriram, Vinayak, Pia, Zubin, Akansha, Chandnee, Sukshita, and Reena for being there by my side in times of celebration and distress. I would also like to acknowledge my friends back home for constantly inspiring me, especially through the tough COVID period.

Last but never the least, I would like to thank my loving parents, and my entire family. God has been kind to give me a family who has always got my back. Words are not enough to express my gratitude towards my parents who are my role models and best friends. The time here during my PhD has helped me realize the true value of their unconditional love for me. The countless

number of conversations with my mother was the fuel behind the efforts during this PhD. My father is a firm believer of education as the main source of wealth and has always supported my education choices without a question. He was the person who motivated me to pursue a PhD, and I can't thank him enough for that. I dedicate my PhD to them. Next, I would like to thank my loving sister, Kirti, who is like my second mother. She ensured that I was taking good care of myself amidst the busy lifestyle during PhD. My local family in USA - Pinki aunty, Peru uncle, Pranita and Priyanka have been instrumental in this process. They have always made me feel at home here in the US and I am very grateful for their kind love and affection. Finally, I would like thank my uncles (Karthik and Kumar), aunts (Vidya and Kalpana) and my loving grandparents for showering me with care and affection.

TABLE OF CONTENTS

LIST OF TABLES

LIST OF FIGURES

ABSTRACT

There has been a growing interest within the aerospace industry for shifting towards a digital twin approach, for reliable assessment of individual components during the product lifecycle - across design, manufacturing, and in-service maintenance, repair & overhaul (MRO) stages. The transition towards digital twins relies on continuous updating of the product lifecycle datasets and interoperable exchange of data applicable to components, thereby permitting engineers to utilize current state information to make more-informed downstream decisions. In this thesis, we primarily develop a framework to store, track, update, and retrieve product lifecycle data applicable to a serialized component, its features, and individual locations.

From a structural integrity standpoint, the fatigue performance of a component is inherently tied to the component geometry, its material state, and applied loading conditions. The manufacturing process controls the underlying material microstructure, which in turn governs the mechanical properties and ultimately the performance. The processing also controls the residual stress distributions within the component volume, which influences the durability and damage tolerance of the component. Hence, we have demonstrated multiple use cases for fatigue life assessment of critical aerospace components, by using the developed framework for efficiently tracking and retrieving (i) the current geometric state, (ii) the material microstructure state, and (iii) residual stress distributions.

Model-based definitions (MBDs) present opportunities to capture both geometric and non-geometric data using 3D computer-aided design (CAD) models, with the overarching aim to disseminate product information across different stages of the lifecycle. MBDs can potentially eliminate error-prone information exchange associated with traditional paper-based drawings and improve the fidelity of component details, captured using 3D CAD models. However, current CAD capabilities limit associating the material information with the component's shape definition. Furthermore, the material attributes of interest, viz., material microstructures and residual stress distributions, can vary across the component volume. To this end, in the first part of the thesis, we implement a CAD-based tool to store and retrieve metadata using point objects within a CAD model, thereby creating associations to spatial locations within the component. The tool is illustrated for storage and retrieval of bulk residual stresses developed during the manufacturing of a turbine disk component, acquired from process modeling and characterization. Further,

variations in residual stress distribution owing to process model uncertainties have been captured as separate instances of the disk's CAD models to represent part-to-part variability as an analogy to track individual serialized components for digital twins. The propagation of varying residual stresses from these CAD models within the damage tolerance analysis performed at critical locations in the disk has been demonstrated. The combination of geometric and non-geometric data inside the MBD, via storage of spatial and feature varying information, presents opportunities to create digital replica or digital twin(s) of actual component(s) with location-specific material state information.

To fully realize a digital twin description of components, it is crucial to dynamically update information tied to a component as it evolves across the lifecycle, and subsequently track and retrieve current state information. Hence, in the second part of the thesis, we propose a dynamic data linking approach to include material information within the MBDs. As opposed to storing material datasets directly within the CAD model in the previous approach, we externally store and update the material datasets and create data linkages between material datasets and features within the CAD models. To this end, we develop a model-based feature information network (MFIN), a software agnostic framework for linking, updating, searching, and retrieving of relevant information across a product's lifecycle. The use case of a damage tolerance analysis for a compressor bladed-disk (blisk) is demonstrated, wherein Ti-6Al-4V blade(s) are linear friction welded to the Ti-6Al-4V disk, comprising well-defined regions exhibiting grain refinement and high residuals stresses. By capturing the location-specific microstructural information and residual stress fields at the weld regions, this information was accessed within the MFIN and used for downstream damage tolerant analysis. The introduction of the MFIN framework facilitates access to dynamically evolving as well as location-specific data for use within physics-based models.

In the third part of thesis, we extend the MFIN framework to enable a physics-based, microstructure sensitive and location-specific fatigue life analysis of a component. Traditionally, aerospace components are treated as monolithic structures during lifing, wherein microstructural information at individual locations are not necessarily considered. The resulting fatigue life estimates are conservative and associated with large uncertainty bounds, especially in components with gradient microstructures or distinct location-specific microstructures, thereby leading to under usage of the component's capabilities. To improve precision in the fatigue estimates, a location-specific lifing framework is enabled via MFIN, for tracking and retrieval of

microstructural information at distinct locations for subsequent use within a crystal plasticity-based fatigue life prediction model. A use case for lifing dual-microstructure heat treated LSHR turbine disk component is demonstrated at two locations, near the bore (fine grains) and near the rim (coarse grains) regions. We employ the framework to access (a) the grain size statistics and (b) the macroscopic strain fields to inform precise boundary conditions for the crystal plasticity finite-element analysis. The illustrated approach to conduct a location-specific predictive analysis of components presents opportunities for tailoring the manufacturing process and resulting microstructures to meet the component's targeted requirements.

For reliably conducting structural integrity analysis of a component, it is crucial to utilize their precise geometric description. The component geometries encounter variations from nominal design geometries, post manufacturing or after service. However, traditionally, stress analyses are based on nominal part geometries during assessment of these components. In the last part of the thesis, we expand the MFIN framework to dynamically capture deviations in the part geometry via physical measurements, to create a new instance of the CAD model and the associated structural analysis. This automated workflow enables engineers for improved decision-making by assessing (i) as-manufactured part geometries that fall outside of specification requirements during the materials review board or (ii) in-service damages in parts during the MRO stages of the lifecycle. We demonstrate a use case to assess the structural integrity of a turbofan blade that had experienced foreign object damage (FOD) during service. The as-designed geometry was updated based on coordinate measurements of the damaged blade surfaces, by applying a NURBS surface fit, and subsequently utilized for downstream finite-element stress analysis. The ramifications of the FOD on the local stresses within the part are illustrated, providing critical information to the engineers for their MRO decisions. The automated flow of information from geometric inspection within structural analysis, enabled by MFIN, presents opportunities for effectively assessing products by utilizing their current geometries and improving decision-making during the product lifecycle.

1. INTRODUCTION

1.1 Background

Across the product lifecycle stages of a component, from design, manufacturing, in-service use to retirement, enormous amounts of data is gathered and archived, which can be potentially utilized for improved decision making, while designing newer versions of the component or within downstream stages of a specific component's lifecycle [1]. However, typically within industrial practice, the lifecycle information is siloed and archived in disconnected databases, as well as scattered in different file formats. Consequently, it is challenging to seamlessly access, interpret, and utilize relevant information for assessment of components without errors, often-times involving the need for humans to intercede within this loop.

The concept of the digital twin aims to create a digital representation of a serializable component or system, which can be used to predict its future performance based on the current available knowledge [2,3]. To fully realize a digital twin representation of a component requires: (i) state information, which is dynamically or periodically updated, (ii) prognosis, which can come from a range of sources, including data driven models, analytical models, or physics-based simulations [2–4], and (iii) a representation of the physical component in a form in which it can be appropriately interpreted [4]. The state information is constantly evolving throughout the product lifecycle [1]. The current thesis proposes a framework for data exchange, archival, and retrieval, as well as dynamically updating pertinent information throughout the lifecycle of a component to realize the digital twin representation, which can be effectively used for prognosis of the component.

In aerospace components, fatigue failure is prevalent [5,6] due to the dynamic loads experienced during their service. Hence, evaluation of the fatigue life plays a crucial role in component analysis for (i) initial design estimates, (ii) post-manufacturing certification purposes, and (iii) estimating remaining service life of fielded components during maintenance, repair and overhaul stages. Physics-based relationships incorporating the underlying microstructure and micromechanical descriptors of the material can be used within prognosis efforts to reduce the uncertainties within life predictions [7]. Classical fatigue life prediction methods involve regression fits through empirical test data. While the specimens used for these tests are, on average,

representative of the material within the component, they are not specific to a serialized component or its geometry. Based on the underlying physical structure and material, each component responds differently (defined as its behavior) to its encountered environments, such as experienced thermomechanical deformation during the manufacturing process or applied loads during service. Hence, firstly, it is critical to account for a component's precise geometry while estimating the in-service stresses, to improve precision in our estimates during the structural integrity analysis. Secondly, the material performance is dictated by process to structure to property relationships [8]. The material's microstructure is a result of the manufacturing history (processing route) and governs the properties [9]. Hence, by tracking the processing path and resulting microstructure, the ultimate performance of the material, at any instance within the component, can be more systematically determined. Therefore, an efficient methodology for storing and exchanging the material's process-structure-properties information is required, in order to integrate these relationships and apply them towards the evaluation of the component's structural performance.

A structured methodology for storing and updating material information is desired to maintain associations between datasets and enable their seamless exchange across the lifecycle. Digital material databases and external network drive(s) can be used to store and collate material lifecycle data, including manufacturing process parameters, microstructural descriptors, mechanical properties, simulated data, and in-service usage conditions [10–13]. Since these datasets could be created or evolve as the material's lifecycle progresses, dynamically updating the information stored within the database is necessary to facilitate downstream engineering analysis. Moreover, it is crucial to maintain associations between the material datasets and the geometric features of the component.

Product lifecycle metadata can be associated with the component's design geometry through the usage of model-based definitions (MBDs), by using computer-aided design (CAD) models [14–16]. Classically, MBDs have been limited to exchanging geometric form, feature dimensional tolerance, and manufacturing process planning metadata [15,16]. In the present thesis, our objective is to expand MBDs for including and exchanging material information across the lifecycle as shown in Figure 1.1. Material information, not only evolves across the lifecycle, but could also vary spatially across the volume of the component (i.e. location-specific material definitions) [9]. This further necessitates tools to associate the material definition to its geometric location or features within the computer-aided design (CAD) models. To address the gaps and to

develop a framework for enabling digital twin, the following pertinent questions were addressed in this research work:

- How do we expand MBDs to store and retrieve spatially varying material datasets?
- Can we enable dynamic tracking, updating and retrieval of material datasets tied to specific serialized components and their geometric features?
- Is it possible to develop a holistic framework which accounts for the following characteristics: (a) allows retrieval and usage of precise geometric and material state information within structural analysis tools and life prediction models, (b) is expandable for tracking and retrieving other pertinent product lifecycle datasets (and not limited only to material datasets), (c) software agnostic framework to facilitate integration with other commercial engineering software(s) and code(s)?
- Can we develop a methodology to inform location-specific microstructure information within physics-based, microstructure-sensitive fatigue life prediction models?
- By accessing and utilizing precise material state information within predictive analysis via analytical and physics-based models, can we demonstrate improved precision in fatigue life estimates associated to a component?
- Can we develop a workflow for utilizing geometric inspection measurements from manufactured or fielded components to inform precise geometric definitions within structural analysis tools?

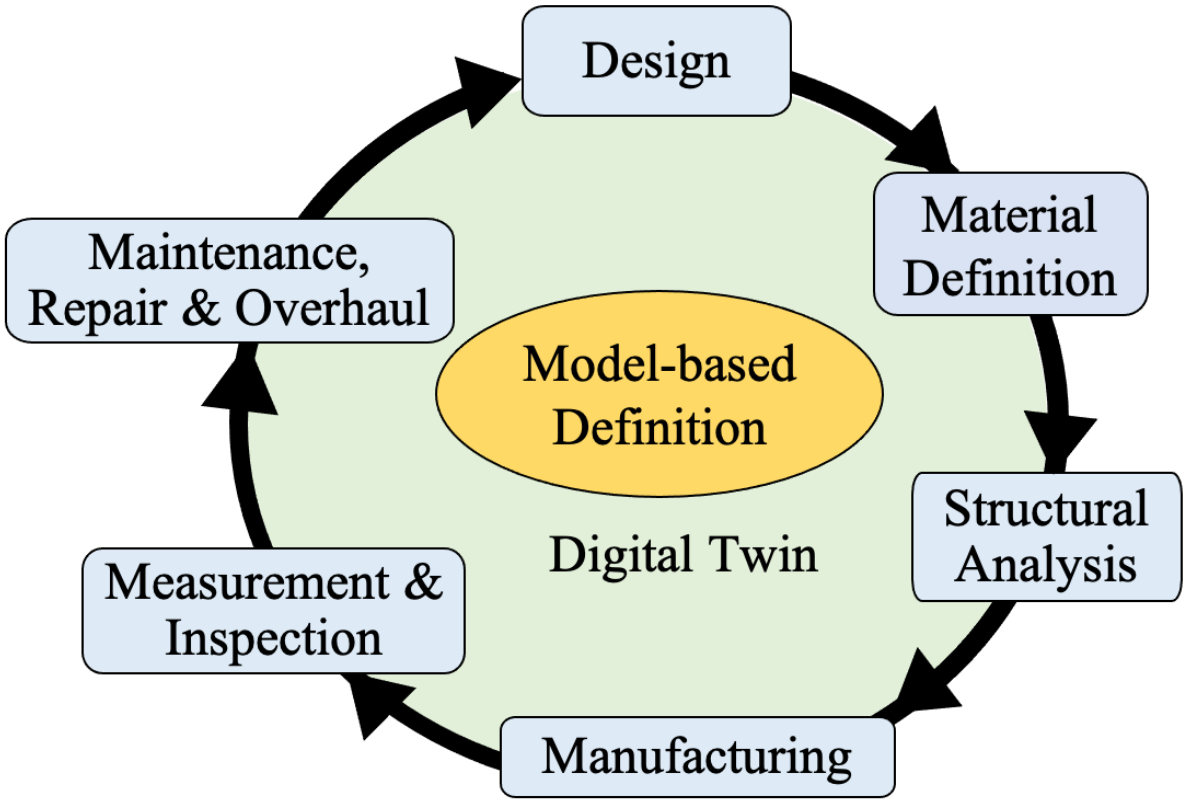

Figure 1.1. Expanding model-based definitions by integrating material definitions across the product lifecycle, in order to facilitate the realization of a component's digital twin.

1.2 Research Contributions

The research contributions in this thesis can be summarized as follows:

(1) Implemented a *data embedding* method (described in Chapter 3) for storing and retrieval of spatially varying material information within CAD models by using point cloud objects.

- Demonstrated a use case to store and retrieve processing-induced residual stress fields within a turbine disk component, for usage within a damage tolerance analysis conducted at critical locations. The part-to-part variations in predicted the fatigue lives owing to variations in residual stress fields has been illustrated (presented in Chapter 3).

(2) Developed a *data linking* framework (model-based feature information network or MFIN) (described in Chapter 4) to enable dynamic tracking, updating and retrieval of material

lifecycle data. The data linking mechanism was achieved by creating a neutral framework to map individual features and spatial locations of a component originating from the CAD model with externally stored and updated metadata in material databases(s) or network drives.

- Demonstrated improved precision in fatigue life estimates obtained via a damage tolerance analysis of a linear friction welded bladed disk component by incorporating manufacturing induced material state information (residual stress fields and microstructural attributes) within the analysis. (Presented in Chapter 4).

(3) Extended the MFIN framework to enable physics-based, microstructure-sensitive and location-specific fatigue life predictions in a component. The MFIN framework was expanded to include data linkages for information pertinent to sub-scale micromechanical modeling (via crystal plasticity finite-element or CPFE analysis).

- Demonstrated improved precision in fatigue life predictions tied to a dual-microstructure heat treated turbine disk component by enabling and realizing a location-specific lifing approach via accounting for local microstructures. The MFIN framework was utilized to access (i) grain size statistics and (ii) the macroscopic strain fields to inform precise boundary conditions for the CPFE analysis. (Presented in Chapter 5).

(4) Developed an automated workflow to utilize geometric inspection measurements within structural analysis tools via the MFIN framework, thereby facilitating analysis of components by using current geometric state.

- Demonstrated the creation of a CAD model (and associated stress analysis) of an in-service turbofan component by utilizing geometric inspection data, thereby capturing any modifications to its surfaces due to foreign object damages. This was achieved by integrating the scanned coordinate measurement data (acquired during a component's maintenance) to surface features via MFIN, which was retrieved and fitted using freeform surfaces (via an external code), followed by finally updating the surface geometries within the nominal CAD model of the component with fitted surfaces (presented in Chapter 6).

2. LITERATURE REVIEW

2.1 Evolution of digital engineering

Traditional component design practice has largely been based on the geometry of the product. Two-dimensional, paper-based drawings have been used to represent the geometric shape and tolerances of an object (with different views as shown in Figure 2.1) with associated component design details for centuries. These drawings have been used to exchange the design definitions through different stages in the product lifecycle, such as manufacturing, quality inspection, and maintenance [17]. Typically, components are manufactured as specified by the geometric shape in the design, followed by physical testing to qualify the components, in order to meet the desired minimum performance per the design intent. This process of physically producing and then qualifying components is associated with multiple manufacturing trials that incur high costs and increased development time [18]. Based on the underlying physical structure and material composition, components respond differently to their encountered environments [19], during manufacturing and service. The material behavior evolved during the processing route of a component, plays a crucial role in determining its final performance capabilities. Inclusion of behavioral information with the geometric shape in the design definition has an opportunity to aid in forecasting the component's performance upfront in the design process, thereby reducing expensive manufacturing trials and enabling the exploration of a larger parameter space for new designs to meet the performance requirements, due in part to its inclusion within the digital artifact rather than in a separate, siloed location.

With the advancement in digital technology, predictive models have been evolving to simulate the manufacturing process and to determine the component behavior. In parallel, the design function has shifted from paper-based, 2D drawings to using 3D Computer-aided design (CAD) models to represent and communicate design definitions [20,21]. Utilizing predictive models to simulate behavior and capturing these definitions in 3D CAD models provides an opportunity to include behavioral information in the earlier stages of design, which provides opportunities to centralize within a secure location versus multiple disparate locations. However, current CAD models (shown in Figure 2.1(b)) are limited to capturing the shape and geometric definitions

(explicit definitions) and have very limited capability to include implicit definitions, such as the behavior developed as a result of the component's structure.

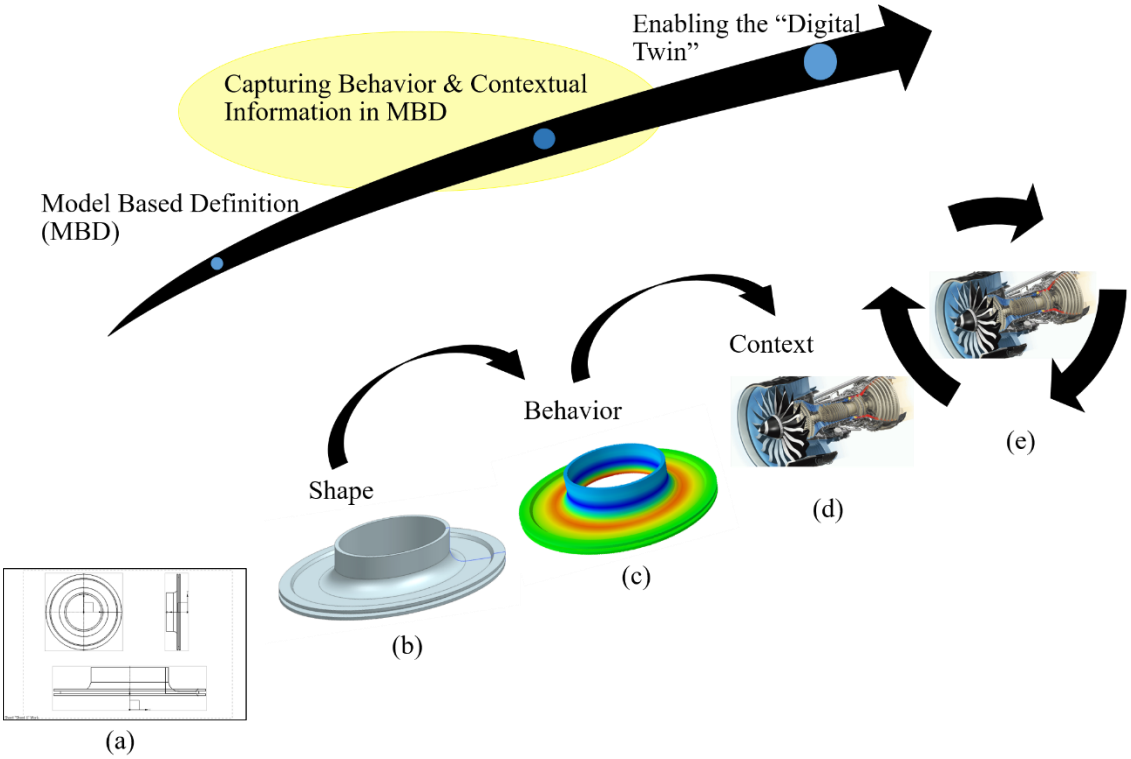

Figure 2.1. The overarching vision to transition towards a digital twin by capturing the behavior definition within the design context. The figure represents this transition in design definition from (a) 2D paper drawing based, to (b) CAD based to (c) MBD-CAD based to (d) Virtual Environment based [22] to (e) Lifecycle based [23].

The use of 3D CAD models to include detailed product definitions, and replace 2D paper-based technical drawings, is also a goal of the concept of model-based definition (MBD). The aim is to use MBD-CAD models to communicate product definitions, in order to improve the quality of the exchanged product information and eliminate errors originating due to manual human intervention and interpretation of product metadata; both of which can lead to significant cost savings and acceleration of the design process cycle [17,20,24] . With this motive, CAD models have been used as an input to manufacturing processes, communicating the desired component geometry and the tolerances applied to its features [25]. However, the purpose of using the model-based approach has been expanding, beyond communication, for supplying the driving inputs

within the downstream manufacturing stages and spanning across the entire product lifecycle [26–29]. With inclusion of the behavioral information within CAD models (Figure 2.1(c)), the level and type of information captured and exchanged using MBD techniques exceed those of a simple geometric model.

Further, the MBD approaches can be expanded to include contextual information, such as the operating environment details or the process environment details. The contextual information from the MBD can provide details for simulating (Figure 2.1(d)) a virtual product environment. Hence, by means of MBDs, we could potentially create a digital prototype of the designed component or the as-designed digital twin, as shown in Figure 2.1(e). These as-designed twin, also known as product twin, can be used to simulate the component to forecast the performance capability during the design stage and prior to the production [4,30]. Since the product lifecycle information tied to component evolves across the product lifecycle, this requires as-designed digital twin to be dynamically updated for creating as-manufactured digital twins post the manufacturing process and as-used digital twin to replicate fielded components. In order to progress towards this vision of realizing digital twin, the current thesis firstly, addresses on closing the gap for storing and exchanging behavioral definitions via CAD models (specifically material definitions). Next, we develop a strategy for dynamically updating material behavioral information associated to geometric features in a CAD model.

2.2 Significance of incorporating processing-induced residual stresses within fatigue life analysis of components

The concept of the MBD can be applied to include manufacturing process-induced residual stresses within design definitions of a component, as the residual stresses influence the component production process and performance such as durability and damage tolerance [31]. Residual stresses influence the fabrication of a component, especially in a multi-stage manufacturing process. Components encounter thermomechanical loads during processes such as forging or heat treatment, that induces permanent localized strain gradients. These strain gradients manifest as residual stress distributions within the component [32]. These stresses are classified as bulk residual stresses or Type I, when they equilibrate over the length scale of the component dimensions. The residual stresses redistribute after each stage during the manufacturing process, and influence the succeeding manufacturing steps [33]. Due to excessive residual stresses,

components can distort during the machining stages, exceeding the geometric tolerances of specific features [34,35]. Incorporating residual stress distributions from process modeling steps within the design definition can provide the residual stress distribution knowledge and enable optimizing the process parameters to avoid part distortion and scrap for a fixed design of the component. Process modeling tools, such as DEFORM [36], simulate the manufacturing process steps to predict these bulk residual stress distributions from each manufacturing step.

Post manufacturing, the residual stress distribution developed within the component, influences its performance, especially the fatigue life of the component [37,38]. For a crack or a flaw at a location within the component, compressive residual stress fields inhibit crack growth and delays fatigue failure, whereas tensile residual stress fields accelerate crack growth and debit the fatigue life. However, residual stresses are not typically included in lifetime analyses. By accounting for residual stresses during the lifing process, more informed decisions can be made about the inspection and maintenance schedules and can even result in life extensions of the components. For instance, John et al. [21] have observed an approximate twofold increase in lifetime based on a damage tolerant analysis by including the 30% retained compressive residual stress from shot peening. Enright et al. have demonstrated the integration of residual stress fields from DEFORM process model with probabilistic damage tolerant analyses, specifically DARWIN (Design Assessment of Reliability with INspection), for life prediction analysis at critical zone locations [39]. Including residual stress fields from models within design definition, and their inclusion for structural analysis and lifing models, requires a method to store and exchange the spatially varying residual stresses in a form that will persist when used within multiple software tools across the lifecycle.

2.3 Significance of enabling microstructure-sensitive and location-specific fatigue life analysis of components

As previously introduced in Chapter 1, the performance of a component and the underlying material is governed by process-structure-property relationship [8]. Hence, by controlling the processing conditions, we could intentionally tailor the material's microstructure to meet the targeted performance requirements and develop next generation components. A dual-microstructure heat treated (DMHT) turbine disk [40–42] is an example of a component produced with distinct microstructures at individual locations to meet the desired location-specific

performance requirements. To maximize fatigue resistance in the bore region of the Ni-based superalloy disk, fine grain microstructures are produced by exposing the bore region to a sub-solvus (below the γ' solvus temperature) heat treatment process. On the other hand, for achieving improved resistance to creep and dwell fatigue at higher temperatures, coarse grain microstructures are produced in the rim region of the disk via a super-solvus heat treatment. For such gradient microstructures, new methodologies are needed for location specific lifing approaches by accounting for the effects of the underlying microstructure.

Traditionally, while lifing a component, the minimum allowable fatigue life in the material is identified through fatigue testing using specimens which are representative of the component. While following this approach, we treat the entire component as a monolithic structure (i.e. assuming all the locations having similar microstructures and mechanical properties) and the fatigue test data, regardless of the origins of the excised test specimens relative to the component location, is combined for statistical analysis as a single population, often-times resulting in large uncertainty bounds [9]. The minimum allowable life to crack initiation is classically identified as either (i) the -3 standard deviations (-3σ) from the mean value of the material's low cycle fatigue life or (ii) the lower bound life corresponding to probability of failure of 1/1000 (i.e. the B0.1 life), which could lead to overly conservative estimates [7,43]. However, to life microstructure-tailored components with gradient microstructures across the volume of the component, opportunities exist to utilize a location-specific fatigue life analysis approach by treating separate datasets, corresponding to the distinct microstructures, in individual regions/locations of the component [9]. The location-specific lifing approach presents the potential to (i) reduce the uncertainties in fatigue life predictions originating from traditional lifing approach and (ii) identify life limiting locations in the component which require special attention during inspection and maintenance or additional considerations for design modifications [9,44].

Microstructure-sensitive fatigue life prediction frameworks via crystal plasticity finite-element (CPFE) simulations, presents opportunities to utilize a physics-based approach to evaluate location-specific fatigue life in a component. Within crystal plasticity [45,46], microstructural grain-level information is utilized and elastic and plastic anisotropies are incorporated while evaluating distributions of strain accumulation and stresses. Energy-based fatigue indicative metrics [47–51] have been proposed to predict the fatigue crack initiation by combining the contributions of both the plastic strain (which captures dislocation motion) and shear stress (the

resistance to the dislocation motion). Bandyopadhyay et al. [49] presented a single energy-based fatigue indicative metric (critical value of accumulated plastic strain energy density or $W^{p}_{criticial}$), applicable for predicting fatigue crack initiation across multiple loading [49] and temperature conditions [50]. However, to effectively utilize this type of modeling approach for conducting location-specific fatigue life analysis of components within a workflow, the results of the manufacturing process and precise microstructural descriptors are required to instantiate the crystal plasticity models. In this work, we create connectivity between component's geometric definitions and its location-specific microstructural information, for use within the crystal-plasticity analysis. Additionally, the individual locations in the component are exposed to varying stresses and strains during service, which is a function of the component geometry, applied loading conditions, and the gradient material structure. These stress/strain states at distinct locations are crucial inputs to inform precise boundary and loading conditions for the sub-scale CPFE analysis for the life analysis of components. Component-scale finite-element (FE) simulations with in-service loading conditions can be utilized to obtain the stress/strain distributions. Hence, we require a methodology to utilize stress/strain fields from component-scale FE analysis for informing boundary conditions within sub-scale CPFE simulations. With this overarching aim, we develop a holistic framework (Figure 2.2), to efficiently assess fatigue life of components with tailored and/or gradient microstructures, by utilizing a microstructure-sensitive computational approach. As shown in Figure 2.2, we start creating a digital twin of the component by including manufacturing induced-material state description and subsequently enable using the information within component lifing.

Figure 2.2. Overarching digital twin framework for conducting location-specific fatigue life analysis of components with direct connectivity to design and manufacturing data workflows and in-service loading states via microstructure-sensitive crystal plasticity-based life predictions.

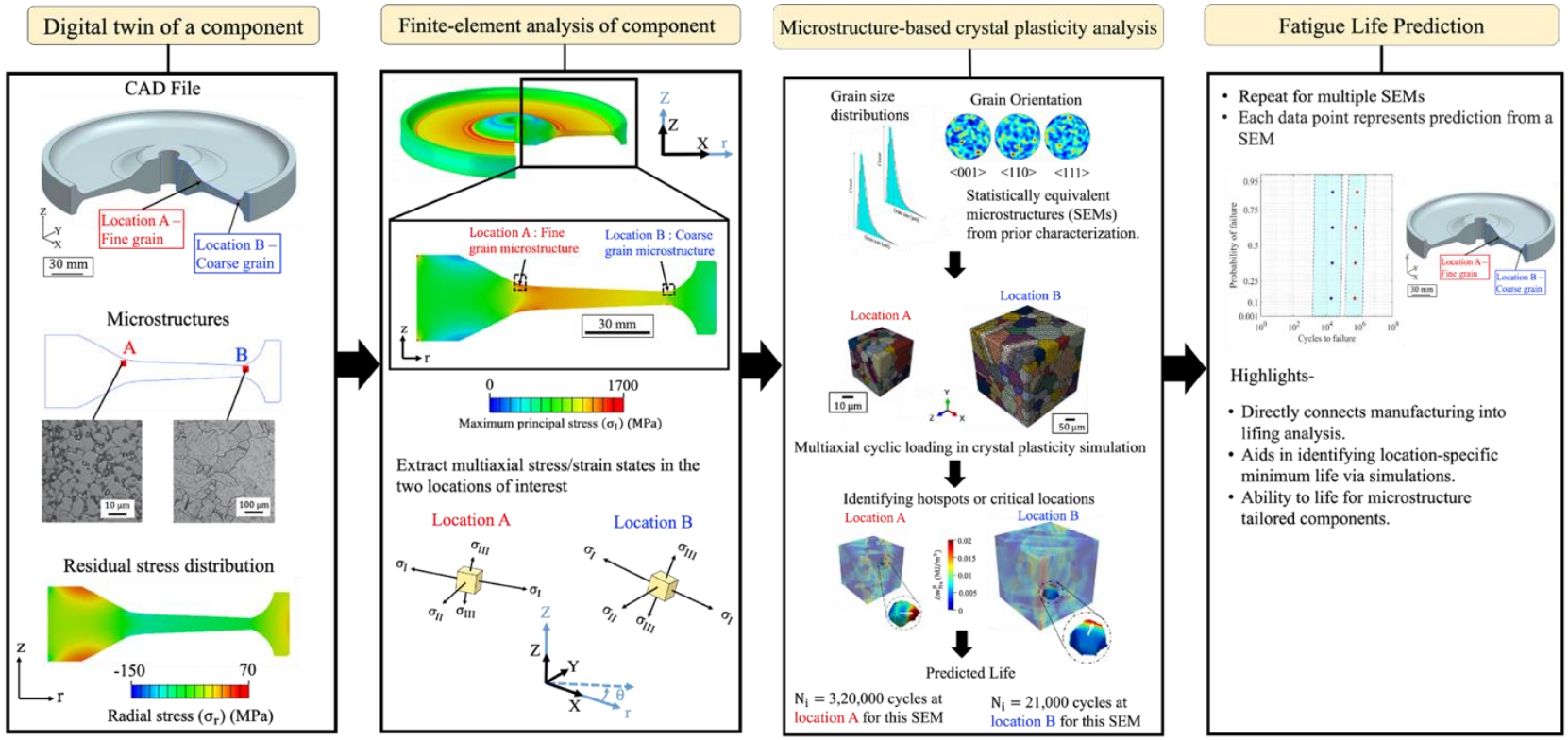
Digital twin of a component
CAD File
Location A – Fine grain
Location B – Coarse grain
30 mm
Microstructures
A
B
10 μm
100 μm
Residual stress distribution
-150
70
Radial stress (σr) (MPa)
Finite-element analysis of component
Location A : Fine grain microstructure
Location B : Coarse grain microstructure
30 mm
0
1700
Maximum principal stress (σI) (MPa)
Extract multiaxial stress/strain states in the two locations of interest
Location A
Location B
Microstructure-based crystal plasticity analysis
Grain size distributions
Grain Orientation
<001>
<110>
<111>
Statistically equivalent microstructures (SEMs) from prior characterization.
Location A
Location B
10 μm
50 μm
Multiaxial cyclic loading in crystal plasticity simulation
Identifying hotspots or critical locations
Location A
Location B
Predicted Life
Ni = 3,20,000 cycles at location A for this SEM
Ni = 21,000 cycles at location B for this SEM
Fatigue Life Prediction
Repeat for multiple SEMs
Each data point represents prediction from a SEM
Probability of failure
Cycles to failure
Location A – Fine grain
Location B – Coarse grain
30 mm
Highlights-
Directly connects manufacturing into lifing analysis.
Aids in identifying location-specific minimum life via simulations.
Ability to life for microstructure tailored components.

2.4 Significance of utilizing current geometric description during structural integrity analysis of components

Components encounter geometric deviations from the design during the manufacturing process, thereby necessitating decision-making regarding their disposition. During quality inspection, the manufactured components are assessed to evaluate if the geometries meet the allowable geometric tolerances and materials specifications. A materials review board (MRB) process [1] is required to analyze and assess out of tolerance components, in order to make decisions regarding their usability and certification. Common dispositions include accepting the part as is, accepting with concessions, repairing the part with secondary manufacturing processes, or scrapping it altogether (Figure 2.3). In some instances, these decisions are based on experience and engineering intuition, while in other cases, time consuming, one-off analyses need to be conducted. Structural analysis can be used to simulate the in-service loading conditions and evaluating the performance capabilities of these manufactured components, by utilizing their precise geometries post manufacturing. However, the structural analysis tools currently require manual creation of the geometric models to instantiate the manufactured components via interpreting physical measurements from the quality inspection process, which can be time-consuming, error prone, and is often forgone to meet production schedule needs.

For capturing the deviations in the surface geometry of a component, coordinate measuring machines (CMM) can be utilized to acquire position coordinates by scanning physical surfaces [52]. Reverse engineering techniques for fitting surfaces to point cloud coordinate measurement data has been developed extensively [53,54]. Non-uniform rational B-spline (NURBS)-based fitting approaches enable capturing complex surface profiles efficiently by allowing local control of the shape [55–57]. These fitting algorithms are usually standalone code(s), which require input from the relevant CMM datasets. In doing so, it is crucial to track the measured surface in the component and the applicable CMM dataset, for ultimately creating the geometric model of the component. In the present work, we utilize a methodology to create connectivity between the CMM datasets and measured surfaces by means of MBDs (Figure 2.3), with the overarching aim of facilitating assessment of components while using their current geometric description within the product lifecycle.

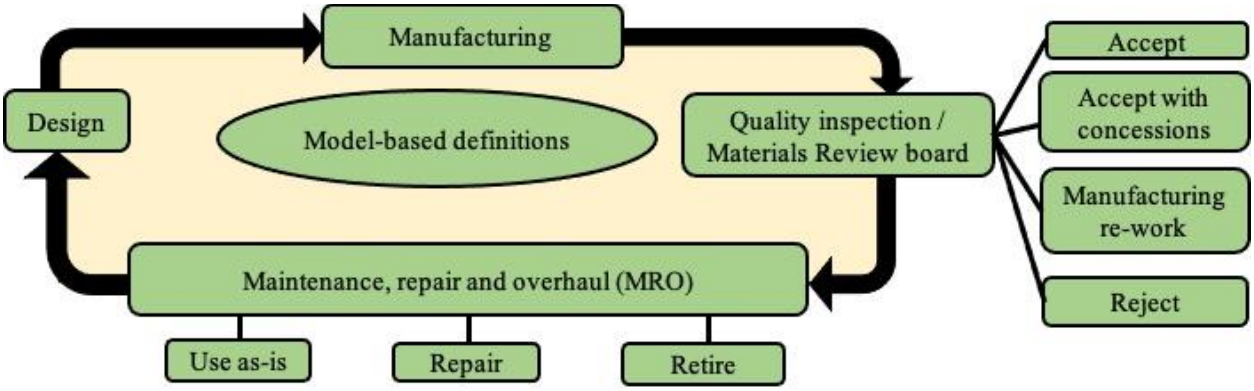

Figure 2.3. Vision of utilizing model-based definitions for exchanging data across the product lifecycle in order to enable more informed decision-making regarding the disposition of a component.

3. DATA STORING OR EMBEDDING APPROACH

The contents of this chapter were published in Gopalakrishnan S, Hartman NW, Sangid MD. Integrating materials model-based definitions into design, manufacturing, and sustainment: a digital twin demonstration of incorporating residual stresses in the lifecycle analysis of a turbine disk. Journal of Computing and Information Science in Engineering (2021) 21(2).

For integrating material datasets to spatial locations within a CAD model, initially, a CAD-based tool was implemented to store and retrieve metadata using point objects, which is described in this chapter. The tool enables importing externally stored metadata into the CAD software's environment, thereby facilitating storage and retrieval of metadata at spatial locations within a CAD model. The initial developments of the tool are presented in [58], which was extended and implemented in the current work. The methodology and software framework for the data embedding tool are described in Section 3.1 and 3.2, respectively. The developed tool has been illustrated with a use case (introduced in Section 3.3) for storage and retrieval of bulk residual stresses developed during the manufacturing of a turbine disk component, for downstream usage within damage tolerance analysis of the component. The results and discussion for this chapter is presented in Section 3.4.

3.1 Embedding Methodology Background

For associating metadata to a component's feature locations, a tool has been developed to create spatial points within the CAD model to store the metadata. Points have been used to store data as they are fundamental geometric objects that can be used to create other geometric entities such as lines, arcs, surfaces, and solids. This enables storing the metadata with precision on fine topological features such as a vertex, on the component edges, and surfaces or even within the bulk volume. Within the CAD environment, each point object is defined by its location coordinates (x,y,z). The tool has been developed to store metadata as name value pairs attached to these point objects, which defines the attribute name and the value of the attribute. Once stored, the location of each of the points within the geometric space of the model acts as a spatial index for the associated metadata. The point objects along with the stored metadata values are henceforth referred to as attribute markers in the current chapter. An attribute marker can store multiple metadata attributes. For instance, multiple material definitions that apply to a particular location

can be associated using a single point. This capability can be applied for storing the components of tensorial quantity, such as residual stresses. The data types that can be stored currently using the tool are numbers and textual information. Attribute markers follow a schema which is as follows: *[(x position), (y position), (z position), (Name of Attribute 1), (Value of Attribute 1), (Name of Attribute 2), (Value of Attribute 2) … (Name of Attribute n), (Value of Attribute n)*]. The attribute names are user defined and can comprise alphanumeric data with spaces, whereas the attribute values must be a numeric value of floating-point data type. The tool has been developed to allow importing and storing datasets, which are structured by nature, and by following this schema, they enable querying and searching for data retrieval.

3.2 Software Framework

The embedding tool has been developed as a plug-in for the CAD tool, executed by the user while launching the CAD software (Figure 3.1(a)). The integration of the embedding tool with the CAD software has been performed using the CAD tool's Software Development Kit (SDK), which allows making use of the command-structure functions specific to the CAD tool. The only CAD-dependent functionalities used for integration are the loading and unloading process of the plug-in, while opening and closing the CAD software, respectively. Thus, the embedding plug-in can be easily switched and used with a different CAD tool by using the CAD tool's specific SDK's functionalities. The current implementation of the tool is shown for Siemens NX 10.0 CAD tool. Once the tool is loaded within the CAD software, the user can interact with the model to include external datasets by storing and retrieving the stored metadata directly from the CAD model.

The workflow for the metadata storage process using the tool is represented by the flow diagram shown in Figure 3.1(b). The process is initiated by the selection for a data storage option. The tool allows two methods of importing metadata. For small sets of data, attribute markers can be created manually by clicking the location where the markers apply within the CAD model. On the other hand, larger sets of metadata can be imported using the bulk data import option. The bulk import method creates a collection of attribute marker points or a point cloud, each with its associated metadata set. In order to utilize this method of storage, the imported data must be structured following the attribute marker schema (described in Section 3.1) in a comma space value (CSV) file. While creating the CSV file and defining the spatial coordinates of the attribute

markers, if there are differences in the coordinate systems between the CAD model and the external software / data sources where the attribute marker datasets originate, a suitable correction using translations and/or rotations must be applied manually to ensure consistent storage of the spatial metadata within the component's CAD model. During the import process, the CSV file is imported from the database and the tool generates attribute markers from the available datasets. In the current study, material behavioral definitions across the entire component geometry have been captured using the bulk import mechanism.

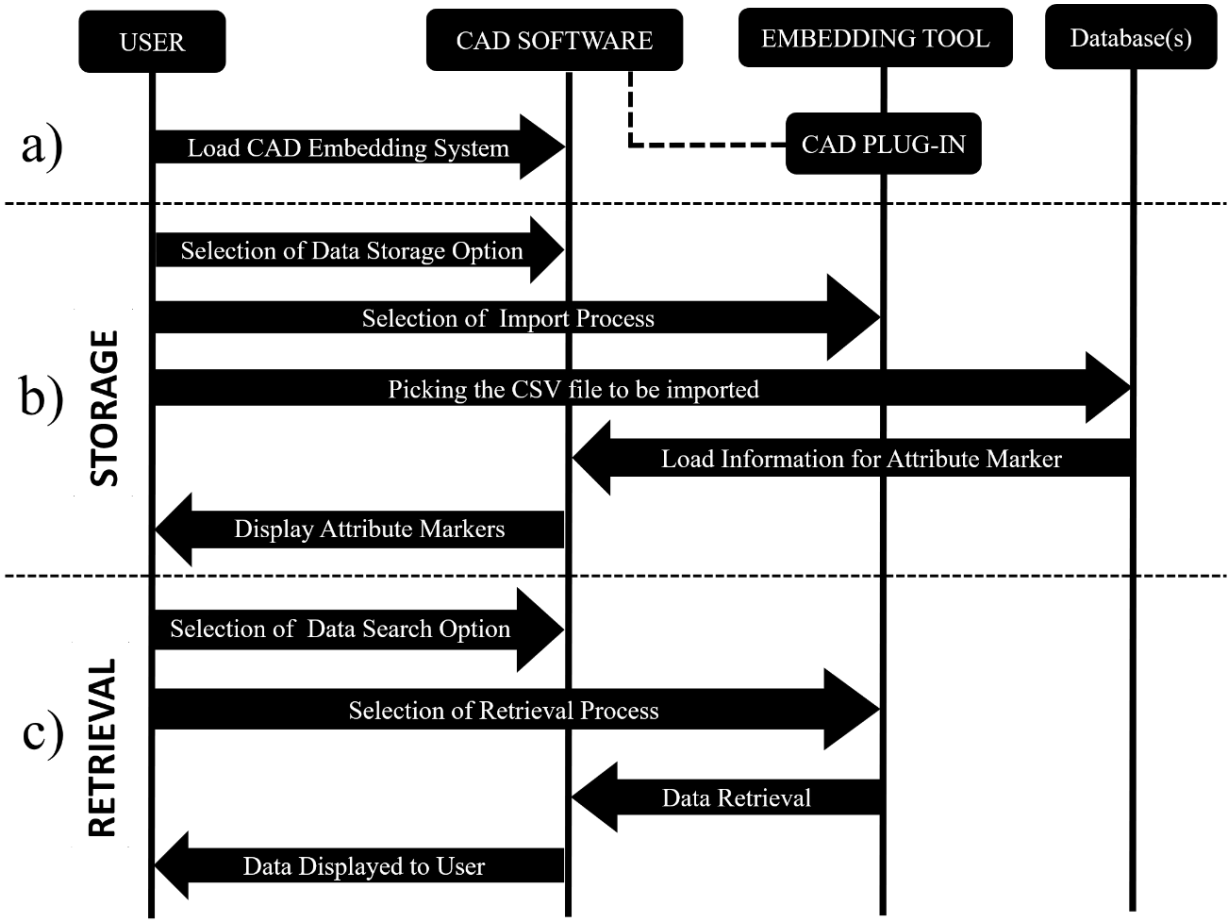

Figure 3.1. A flowchart describing the CAD-based embedding tool's software architecture, including the: (a) integration of the tool with the CAD software, (b) data storage process, and (c) data retrieval process.

The search and retrieval of stored metadata can be initiated using the attribute marker entities via one of the following options: either the attribute name or the attribute marker location.

The metadata retrieval workflow has been presented in Figure 3.1(c). To search based on attribute names, the embedding tool filters and extracts all the spatial locations which have the particular attribute defined, and to extract attribute values from a specific location within the model, the tool executes a Python script that searches for an attribute marker using its location coordinates within the CAD model, with the attribute markers being displayed using the CAD tool. For locations within the model where there is no stored metadata, the current implementation extracts and returns the nearest attribute marker. The extraction capability of the tool enables communicating the location-specific metadata directly using the CAD model, which provides a significant advantage since many embedded attribute values are typically lost or corrupted during data translation using neutral data formats.

3.3 Residual Stress Use Case

In order to illustrate how the developed tool enhances a CAD model to store material behavioral information and starts forming a model-based definition, a use case has been implemented for storage and retrieval of bulk residual stresses [32] generated during the manufacturing process of a turbine disk. Residual stresses directly influence the component's production process and performance such as its durability and damage tolerance [31]. By taking residual stresses into account during the damage tolerance analysis, more informed decisions can be made about the inspection and maintenance schedules and can even result in life extensions of the components [59,60]. Hence, the goal here is to associate residual stress fields to locations within the component's CAD model and exchange the stored residual stresses for damage tolerance analyses, directly using the CAD model. For implementing the use case, various tools/software(s), data sources, and codes have been utilized along with the embedding tool. The flow of data between them is shown in Figure 3.2. From a prior Metals Affordability Initiative Foundational Engineering Program (MAI-FEP) study [61], residual stress data have been acquired from both experimental characterization, as well as from a process modeling tool (DEFORM), both of which are stored within the CAD model using the embedding tool. Additionally, in order to produce in-service stresses in the component for damage tolerance analysis, a finite-element analysis tool has been used to simulate the structural characteristics of the component. Herein, the CAD model provides the component geometry for the analysis and the resulting in-service stress fields are further stored within the CAD model using the embedding tool. Finally, both the stored

residual stresses and in-service stresses are retrieved from the CAD models via the embedding tool and utilized within a damage tolerance analysis code. With the overarching aim of implementing the use case, the following sections describes the component model creation, residual stress data acquisition techniques, and data preparation for storing using the tool.

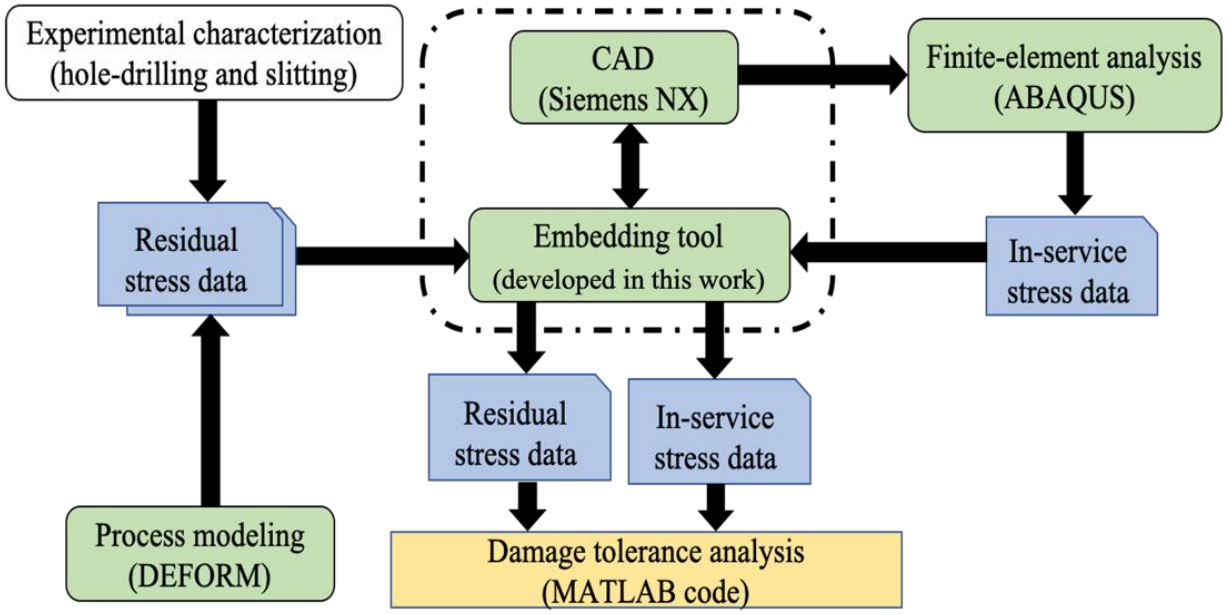

Figure 3.2. A schematic representing the flow of data between various tools/software(s), codes, and other data sources for implementing the use case.

3.3.1 Turbine disk CAD model

The first step was to create a CAD model, representing the geometric definition of the turbine disk. Figure 3.3(a) represents the trimetric view of the turbine disk component model. A disk is an axisymmetric component (Figure 3.3(c)), which is to say the geometry is symmetric about the z-axis passing through the centroid of the disk and shown as a 3D model in Figure 3.3(b)). This CAD model represents the as-designed nominal disk geometry.

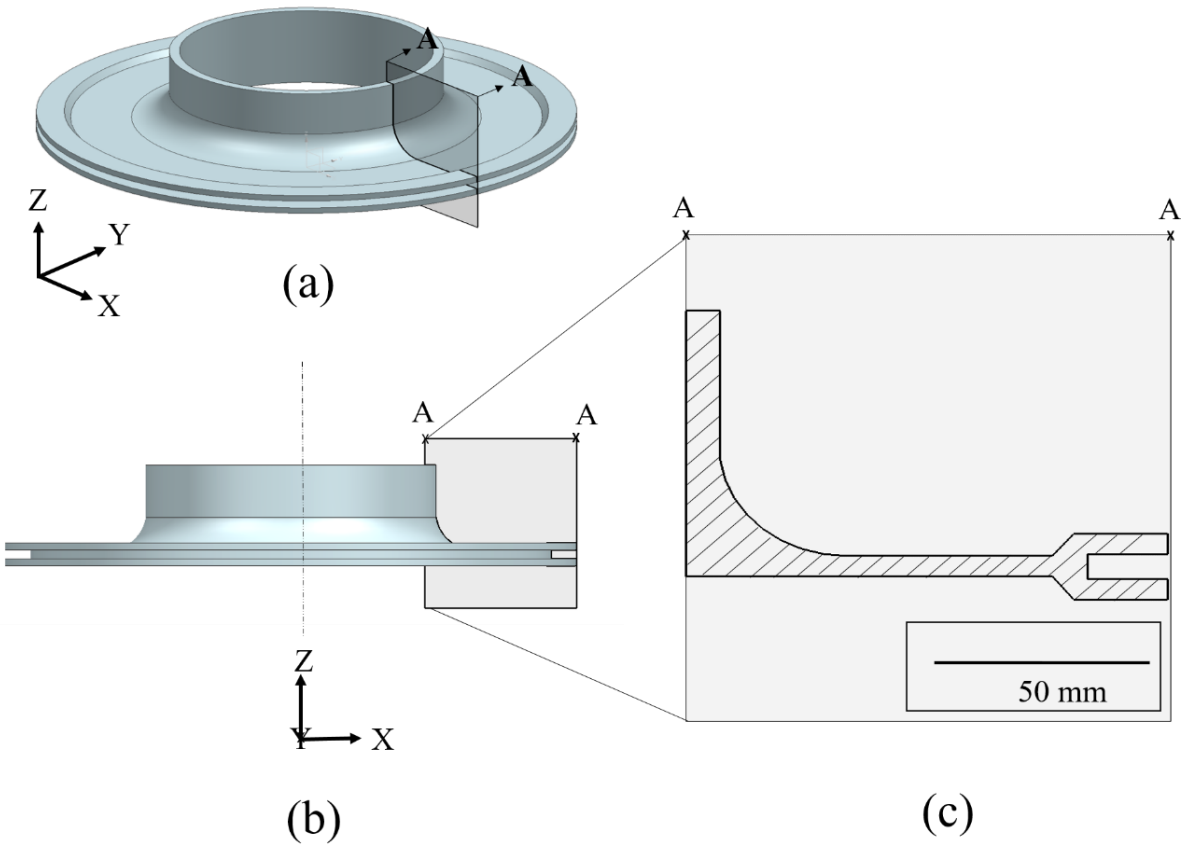

Figure 3.3. Views of the turbine disk model, namely the (a) trimetric view, (b) front view, and (c) 2D axisymmetric view. The section view A-A shows the 2-D axisymmetric view of the turbine disk.

3.3.2 Residual stress data acquisition and import dataset preparation

The residual stress data has been acquired using experimental characterization techniques within the MAI-FEP program [61], namely hole-drilling and slitting, performed at feature locations 1-11 and 2-3, respectively (as defined in Figure 3.4), within the disk. Process modeling, using DEFORM, has been used to determine the full field residual stresses across the entire component. Further, cases of variations in the residual stress distribution, arising due to uncertainties in the process modeling [62], have been also been generated. These residual stress datasets have been structured following the attribute marker schema and stored at locations (as displayed in Figure 3.4) within the CAD model of the disk.

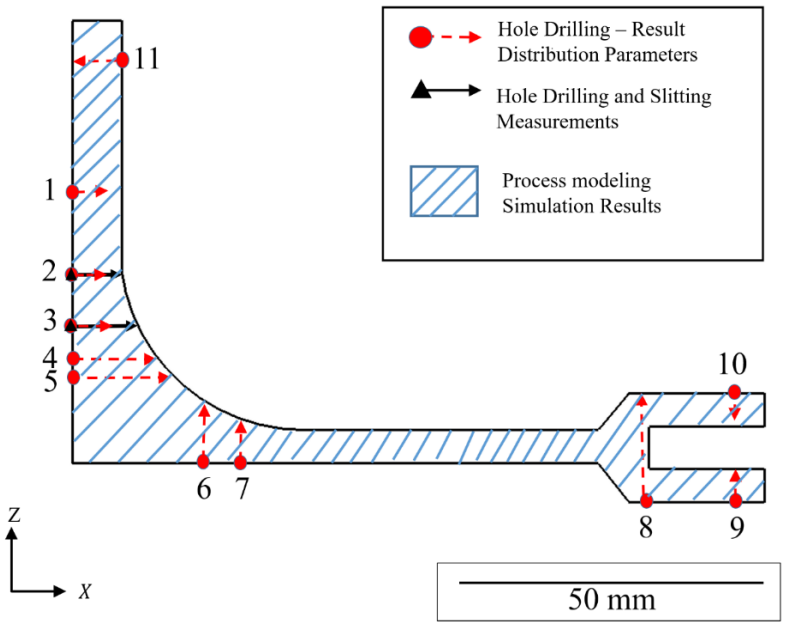

Figure 3.4. Locations in the CAD model of the turbine disk, where residual data are being stored, as represented on the 2D axisymmetric view of the disk.

Residual stress Data Acquisition: Experimental Characterization

The first characterization method that has been used to acquire residual stress data is hole-drilling. Hole-drilling is a mechanical characterization technique used to determine the near-surface residual stresses as a function of depth. The technique involves drilling of a hole in steps from the component surface along the thickness direction, which leads to relaxation of the residual stresses and deforming of the component accumulated during initial manufacturing. A strain gage rosette is placed on the surface, to measure the associated deformation at each step. The schematic of the hole-drilling setup is shown in Figure 3.5(a). The measured deformation is used to back calculate the in-plane residual stress components, originally present, at the hole location from the surface.

Hole-drilling measurements have been performed on a physical turbine disk component at locations 1-11, as shown in Figure 3.4, at positions around the disk's axis at 15°, 105°, 195° and 285° to capture the variation in the measured residual stresses around the 3D component. In feature locations 1-5 and 11, distribution parameters of hoop ($\sigma_{\theta\theta}$), axial (σ_{zz}), and shear ($\sigma_{\theta z}$) components of the residual stress have been obtained, whereas in locations 6-10, statistics of radial (σ_{rr}), hoop ($\sigma_{\theta\theta}$), and shear ($\sigma_{r\theta}$) stress components have been obtained. This dataset has been

organized, with distribution parameters for each stress component as a scalar entry, as follows: *[x,y,z, Mean (Hoop Stress), Numeric value, Standard Deviation (Hoop Stress), Numeric value, Mean (Axial Stress), Numeric value, Standard Deviation (Axial Stress), Numeric value, Mean (Shear Stress), Numeric value, Standard Deviation (Shear Stress), Numeric value]* at locations 1-5 and 11 and *[x,y,z, Mean (Radial Stress), Numeric value, Standard Deviation (Radial Stress), Numeric value, Mean (Hoop Stress), Numeric value, Standard Deviation (Hoop Stress), Numeric value, Mean (Shear Stress), Numeric value, Standard Deviation (Shear Stress), Numeric value]* at locations 6-10 . Further, at locations 2 and 3 (Figure 3.4), the measured axial residual stress component (σ_{zz}) is stored as a function of distance from the surface. Following the schema, the dataset has been created in a CSV file as follows: *[x,y,z, Axial Stress (HOLE-DRILLING), Numeric Value]*, wherein y=0 and z=constant for each feature location with varying x position in the dataset.

Slitting analyses has been used as the second technique to generate residual stress data for the turbine disk component. Similar to hole-drilling, slitting also uses a strain relaxation approach to measure the associated deformation. Unlike drilling of holes, slitting involves cutting of slits from the surface, in steps along the thickness direction with a strain gage placed on the end surface orthogonal to the slit to measure the associated deformation (Figure 3.5(b)). The measured deformation is used to back calculate the originally present axial residual stress (σ_{zz}) component as a function of slit depth. Slitting has been performed on the turbine disk, starting at locations 2 and 3, as shown in Figure 3.4. Following the schema, the dataset has been created in a CSV file as follows: *[x,y,z, Axial Stress (SLITTING), Numeric Value]* wherein y=0 and z=constant for each feature location with varying x position in the dataset.

Residual Stress Data Acquisition: Process Modeling

The manufacturing processing route of the turbine disk that includes forging, heat treat, and machining operations has been simulated to determine the induced residual stress distributions using DEFORM [36], as part of the MAI-FEP [61]. The inputs to the simulation include the initial billet geometry, process parameters, material properties, and the final nominal geometry shape (Figure 3.5(c)). The analysis has been performed using axisymmetric quadrilateral elements. The mesh included 2756 elements with average mesh size of 0.7 mm. For each of these elements, four residual stress components, namely the radial stress (σ_{rr}), hoop stress ($\sigma_{\theta\theta}$), axial stress (σ_{zz}), and shear stress (σ_{rz}), are generated. The element centroids from the process model are used to create

attribute markers, in which the four residual stress components are stored. Since there was no coordinate system mismatch between the CAD model and the process model, the coordinates of elemental centroids can be directly used to create the attribute markers. A MATLAB script has been written to create the import dataset for the embedding tool from the process modeling results file (DEFORM keyword file). Following the schema, the attribute markers dataset in a CSV file have been created as follows: *[x,y,z, Radial Stress, Numeric Value, Hoop Stress, Numeric Value, Axial Stress, Numeric Value, Shear Stress, Numeric Value]*, wherein x,y,z are the elemental centroid positions.

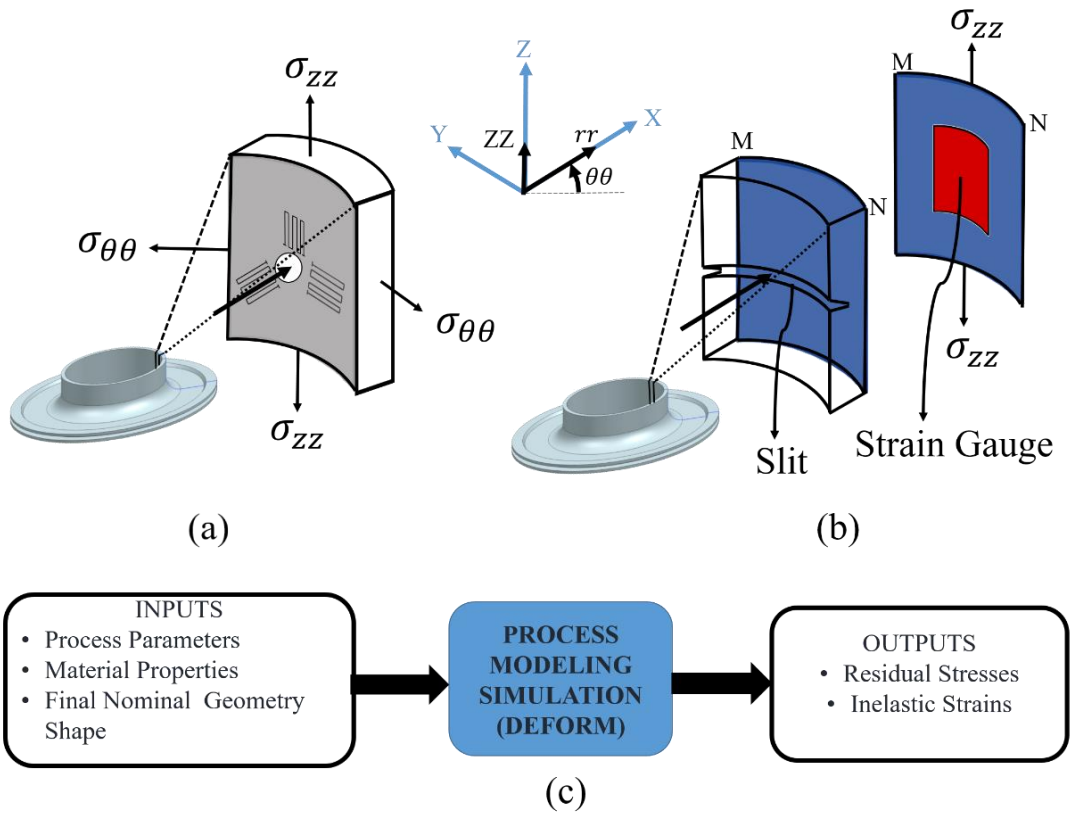

Figure 3.5. Residual stress data acquisition techniques: (a) schematic of the hole-drilling experiment, (b) schematic of slitting experiment, and (c) flow diagram representing the DEFORM process modeling.

Residual Stress Data Acquisition: Process Modeling Variations due to Model Uncertainty

In order to demonstrate potential part-to-part variations that can be forecasted in the as-designed digital twins or tracked among individual components of the as-built digital twins, variations in the residual stresses were studied based on the reported uncertainties of the available dataset [62]. Three cases of varying residual stress distributions have been created, in addition to the available nominal residual stress distribution for this study, to represent cases of part-to-part variations. To create these updated residual stress distributions, the nominal radial stress values were initialized as pre-defined stress fields with perturbations at locations L1 and L2 (as shown in Figure 3.6(a)) within an ABAQUS finite element model, followed by a relaxation step to redistribute and equilibrate the stress fields to generate new residual stress distributions. All the surfaces of the 2D axisymmetric disk model were constrained from displacing in the normal direction, similar to a heat treatment process analysis. The choices of percentage changes for the perturbation were made, such that the change in the final radial residual stresses from the nominal values, after running the analysis step, were within the radial stress uncertainty bounds reported for a location between L1 and L2 in [62]. The updated final radial residual stress percentage changes for the three generated cases at location L1 were 87%, -20.35% and 67.26% and at location L2 were 159%, 109.09%, -172%. The contour plots of the original nominal radial residual stress distribution, and the three instances of distributions arising due to model uncertainty (analogous to part-to-part variation), are represented in the Figure 3.6(a) and Figure 3.6(b)-(d), respectively.

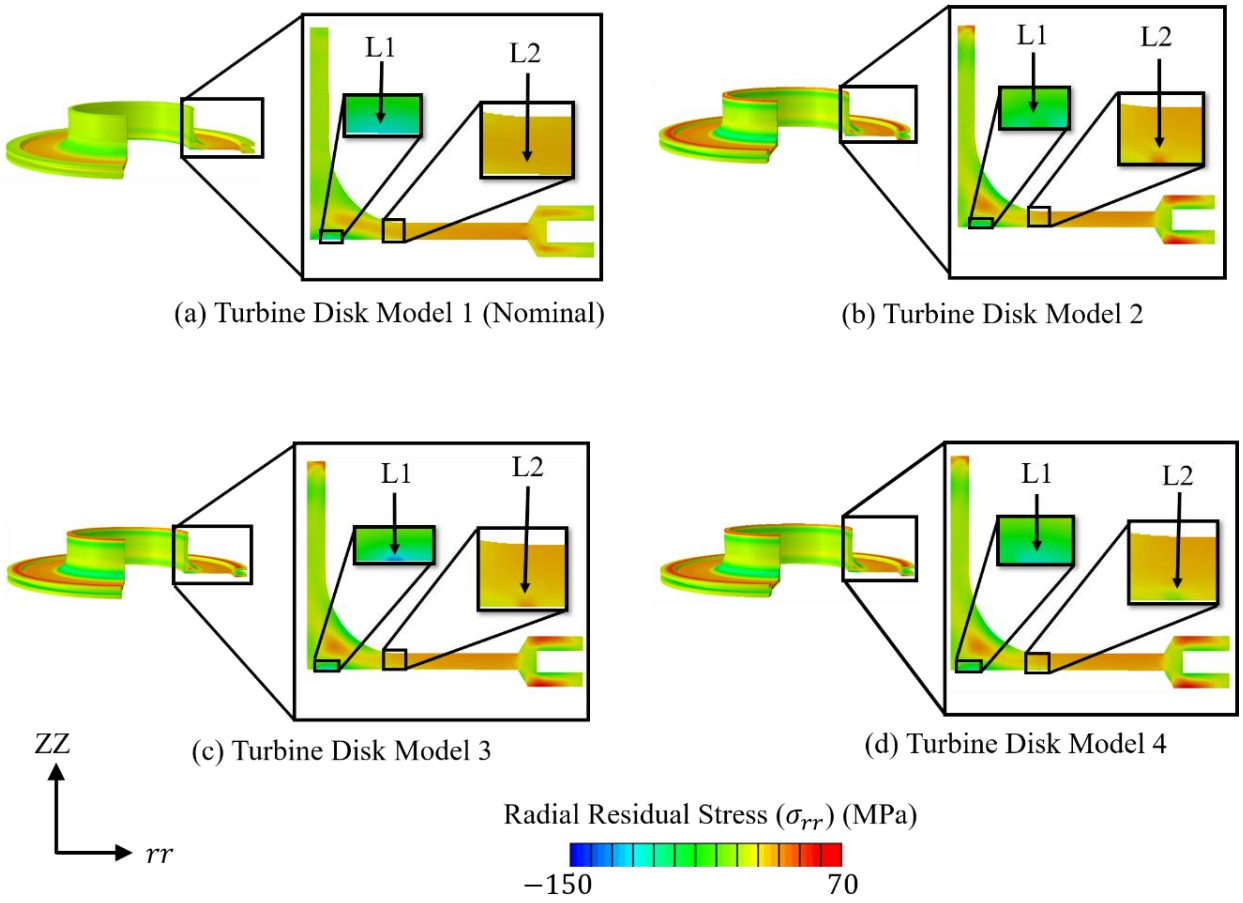

Figure 3.6. Visualization of the predicted radial component (σ_{rr}) of residual stress datasets, with variations arising due to process modeling uncertainties highlighted at locations L1 and L2: (a) Nominal residual stress distribution from DEFORM simulation defined as Turbine Disk Model 1; (b), (c), (d) Three cases of varying residual stress distributions generated to represent process modeling variations termed as Turbine Disk Model 2, Turbine Disk Model 3 and Turbine Disk Model 4, respectively.

3.4 Results and Discussion

3.4.1 Inclusion of residual stress fields within CAD model of turbine disk

The residual stress datasets, that have been acquired and re-organized (Section 3.3.2) as per the attribute marker schema (described in Section 3.1), have been imported and stored within the CAD model of the turbine disk using the embedding tool. The four cases of residual stress fields, representing part-to-part variability, have been stored within four instances of CAD models, as shown in Figure 3.7(a)(i-iv) based on the nominal turbine disk geometry, using the bulk data import method in the developed tool. The detailed representation of the enhanced CAD model of

the disk with nominal residual stresses (Figure 3.7(a) (i)) obtained from process modeling and characterization techniques is shown in Figure 3.7(b). The attribute markers are represented as '+', which is the default representation of a point object in the CAD software used in this study. In the process of including the residual stresses, the pre-processing steps involved (a) preparation of the CSV import file with point object information and (b) importing the data to create point objects within the CAD model, both being computationally feasible and taking less than two minutes. After storing the residual stress datasets, the native CAD model's file size increased moderately, from 166 kilobytes to 742 kilobytes, while remaining as a sufficiently small file size to promote data exchange.

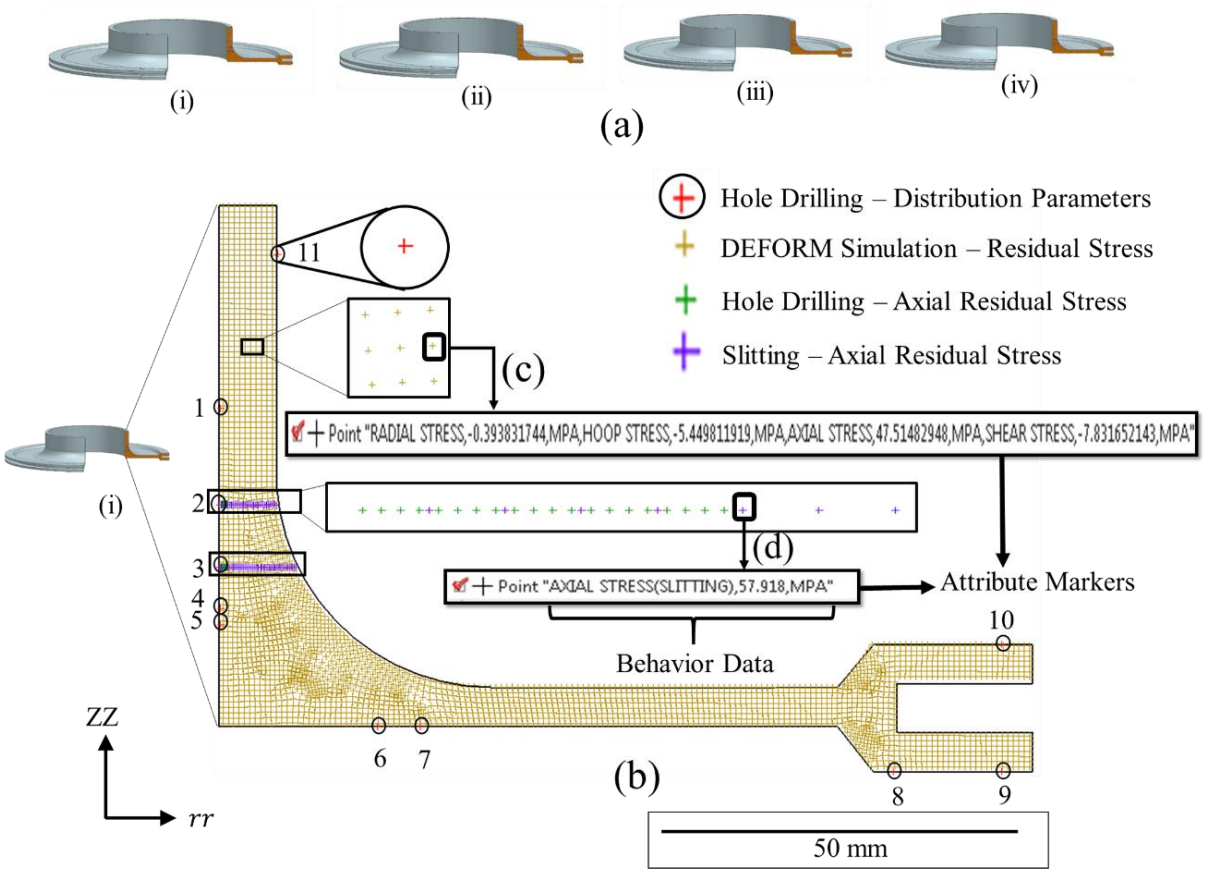

Figure 3.7. (a) Four instances (cases) of the turbine disk CAD model stored with residual stress definitions from: (i) Turbine Disk CAD Model 1 (nominal residual stresses from the process modeling) and (ii), (iii), and (iv) Turbine Disk CAD Model 2-4, respectively with residual stress data to represent part-to-part variations; (b) 2D Axisymmetric view of the 3D CAD model of the turbine disk with attribute markers storing the nominal residual stress data; (c) Example of an attribute marker with residual stress data from process model, following the schema structure (attribute name followed by attribute value, in pairs, storing multiple attributes); and (d) Example of an attribute marker with residual stress data from experimental characterization (Slitting), following the schema structure (attribute name followed by attribute value, at a measurement location).

Attribute markers have been created across the component volume to store residual stress fields from process modeling for all of the 2D axisymmetric components (Radial Stress (σ_{rr}), Hoop Stress ($\sigma_{\theta\theta}$), Axial Stress (σ_{zz}), Shear Stress (σ_{rz})) of the stress tensor (shown in Figure 3.7(c)), enabled by the capability of the framework to store multiple attributes at a single location. This capability has also been used to capture the variations in measured residual stress components from hole-drilling at feature locations 1-11, by creating attribute markers on the surface of the disk at these feature locations. The use of point objects allows storing of metadata with fine precision. For instance, the measured gradient of the axial stress component (σ_{zz}) near the surface at locations 2 and 3 have been captured by creating attribute markers at the hole drilling measurement locations. To store axial residual stress (σ_{zz}) from slitting, 37 attribute markers have been created within 7.62 mm from the surface – one such marker shown in Figure 3.7(d). To store the near surface residual stresses from hole-drilling, 20 attribute markers have been created within a 0.9652 mm width from the surface. The demonstrated ability to store experimentally measured data, alongside the predicted model data, is necessary for the verification, validation, and uncertainty quantification procedures to build trust in the predictive models [63] and is needed to certify the usage of individual components whose design relies on modeling results. This demonstrated ability also becomes critically important for changing business models across product portfolios with increasingly long lifecycles, particularly as it relates to sourcing and provisioning maintenance and sustainment services.

3.4.2 Incorporation of residual stress definitions in fatigue life analysis

The stored residual stress fields can be retrieved from the CAD models using the presented tool and utilized, along with the stresses generated within the disk during its service, for damage-tolerant based fatigue life analysis. During service, turbine disks encounter varying rotation speeds and are subjected to fatigue loading. In order to obtain the in-service stresses generated in these disks, a finite element (FE) simulation has been performed. The analysis has been performed for the maximum load case, while assuming the minimum applied load to be zero, i.e. when the disk is at rest (hence the fatigue stress ratio is R=0). The model used for this analysis, with the loads, boundary conditions, and the mesh are as shown in Figure 3.8(a). The inner bore region of the disk has been imposed with a displacement constraint in the radial direction ($u_{rr} = 0$) and the upper surface has been constrained in the axial direction ($u_{zz} = 0$) to simulate the constraints imparted

by the shaft on the disk. For this simulation, the only load that has been considered is the load applied due to spinning of the disk. A centrifugal load has been applied on the disk with a spin speed of $\omega = 15{,}000\, rpm$ [64]. The outer blade loads and shrink fit loads due to attaching the disk to the shaft, have been ignored. Linear elastic, isotropic material properties of IN718, which are the Young's Modulus $E = 170$ GPa and Poisson's ratio $(\nu) = 0.3$ at 600 ℃ [64], as well as the density $(\rho) = 8220\ \mathrm{kg/m^3}$, have been applied to the disk section. Linear quadrilateral elements have been used to mesh the model with element size of 0.7 mm and 2765 elements, similar to process modeling simulation (Section 3.2.2).

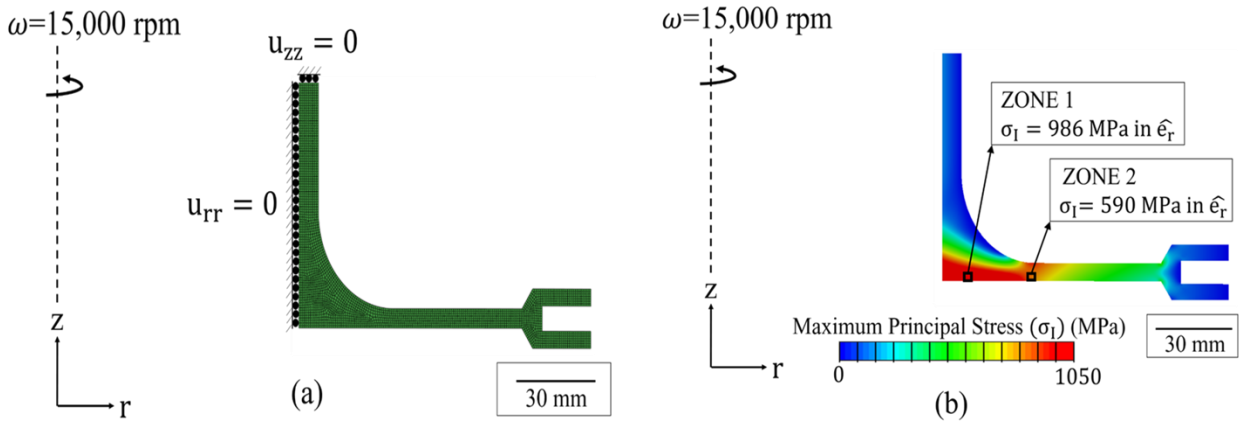

Figure 3.8. Finite element model of the in-service disk: (a) 2D axisymmetric model geometry with quadrilateral mesh elements, centrifugal load, and boundary conditions and (b) Maximum principal stress distribution generated in the disk, from in-service rotation, marked with two selected high stress zones for damage tolerant based lifing analysis.

The maximum principal stress ($\sigma_{I,max}$) distribution within the disk, obtained from the FE analysis is as shown in Figure 3.8(b). In order to store these in-service stresses within the turbine disk model, so as to extract and use them for life analysis, a new CAD instance of the disk was created. From the analysis model, the location coordinates of FE centroids have been computed using the nodal coordinates. The elemental centroid locations along with the maximum principal stresses at each of these elements, form the attribute markers to be imported and stored within the new CAD model instance. To account for the difference in coordinate systems between the FE model and the CAD model (as discussed in Section 3.2), a manual correction has been applied to the position coordinates of the attribute markers using suitable rigid body translations, prior to

importing the dataset. Finally, by using the embedding tool, these attribute markers with $\sigma_{I,max}$ have been imported and stored at these locations within the disk.

In order to perform fatigue life prediction analysis based on damage tolerant approach, two zones have been selected from the high stress regions within the disk (shown in Figure 3.8(b)). The maximum principal stresses in these zones are $\sigma_{I,max} = 986\ MPa$ in zone 1 and $\sigma_{I,max} = 590\ MPa$ in zone 2. In each of these zones, a blunt tip crack with the shape of a U notch of initial length $a_i = 0.10\ mm$, that can be missed during crack inspection [65], has been assumed to be present. The analysis has been formulated such that the maximum principal tensile stresses will lead to opening of the crack, following mode I crack growth. Since the directions of $\sigma_{I,max}$ in these zones are along the radial direction ($\widehat{e_r}$), the crack is assumed to be growing along the axial direction of the disk ($\widehat{e_z}$), such that the tensile maximum principal stresses at these zone locations act as the crack opening stresses. The estimated life for this crack to grow to a critical final crack length a_f has been computed. The final length (a_f) for each zone has been determined as the length at which stress intensity factor (K_I) [66] reaches the fracture toughness (K_{IC}) ($K_{IC} = 85\ MPa\sqrt{m}$ [64]). To estimate the number of cycles (N_f) for the initial crack length (a_i) to grow into a final crack length (a_f), a formulation incorporating both the residual stresses and the service stresses has been used [67].

The Paris law (Eq. (3.1)) provides the relationship during stage II crack growth, between the rate of crack propagation (da/dN) and effective stress intensity factor (ΔK_{eff}), which is the driving force for the crack growth. C, n are Paris constants for IN718, with values taken as $2.83\ X\ 10^{-17}\ \frac{\left(\frac{mm}{cycle}\right)}{MPa\sqrt{mm}}$ and 3.213 respectively at R ~ 0 at elevated temperature [68].

$$\frac{da}{dN} = C(\Delta K_{eff})^n \tag{3.1}$$

The Walker model [69] modifies the effective stress intensity range (ΔK_{eff}) in the Paris law (Eq. (3.1)) as shown in Eq. (3.2), to account for the effects of changes in the R ratio on the crack growth rate. Using this formulation, the effect of residual stress has been incorporated in the stress ratio R (shown in Eq. (3.3)), by linear superposition of the maximum principal applied stresses (i.e. $\sigma_{I,min}$ corresponding to the minimum applied load and $\sigma_{I,max}$ corresponding to maximum

applied load) with the residual stress component (σ_{RS}) along the direction of the maximum principal applied stress. Eq. (3.3) is valid for $R \geq 0$ and takes the value of 0 for cases when $R < 0$. In the present analysis, $\sigma_{I,min} = 0$ and $\sigma_{I,max}$ is obtained from the FE analysis. m is the material dependent Walker exponent (m = 0.5) [70].

$$\Delta K_{eff} = K_{max}(1 - R)^{m} \tag{3.2}$$

$$R = \frac{\sigma_{I,min} + \sigma_{RS}}{\sigma_{I,max} + \sigma_{RS}} \tag{3.3}$$

K_{max} is the stress intensity factor corresponding to maximum load, which has also been superimposed with residual stress as shown in Eq. (3.4)**,** wherein $F(a/w)$ is the geometric correction factor, w is the width of the section and a is the crack length.

$$K_{max} = (\sigma_{I,max} + \sigma_{RS})F\left(\frac{a}{w}\right)(\pi a)^{\frac{1}{2}} \tag{3.4}$$

$F(a/w)$ varies for the crack placed in each of the zones and is a function of a and w. The width of the two sections in the zones analyzed are $w_1 = 27.21$ mm and are $w_2 = 5.89$ mm, respectively. A FE approach was used to obtain the geometric correction factor for the turbine disk, for details please refer to Appendix A. Using the critical stress intensity factor, K_{IC}, and appropriate geometric correction factor, the final crack length has been calculated for each of the zones as $a_{f,Zone1} = 0.6742$ mm and $a_{f,Zone\,2} = 0.6832$ mm.

By substituting Eq. (3.2)-(3.4) in Eq. (3.1) and rearranging dN in terms of da, we can obtain the expression to compute the life in each zone for the crack to grow from the initial to final length by integrating between a_i to a_f (as shown in Eq. (3.5)).

$$N_f = \frac{1}{\left(C\left(\sigma_{I,max} + \sigma_{RS}\right)(1 - R)^{m}\right)^{n}} \int_{a_i}^{a_f} \frac{da}{\left(F\left(\frac{a}{w}\right)(\pi a)^{\frac{1}{2}}\right)^{n}} \tag{3.5}$$

For extracting $\sigma_{I,max}$ and σ_{RS} from the CAD models, the location-based retrieval method of the developed tool has been used. The spatial coordinates of the geometric location ahead of the

initial (assumed) crack were searched in each of the two zone locations, from the CAD model with predicted in-service stresses and the four CAD models containing residual stress fields, in which the radial stress component (σ_{rr}) values were located. In zone 1, the σ_{RS} values obtained from the four turbine disk models are: σ_{RS} = -113 MPa, σ_{RS} = -14 MPa, σ_{RS} = -136 MPa, σ_{RS} = -37 MPa, respectively. Whereas, in zone 2, the σ_{RS} values obtained from the four turbine disk models are: σ_{RS} = 22 MPa, σ_{RS} = 57 MPa, σ_{RS} = 46 MPa, σ_{RS} = -16 MPa, respectively. For the case of this simplified analysis, the residual stress field did not evolve or redistribute for the four CAD models, as the crack was propagating. Since the turbine disk CAD models each have the same nominal geometry, the coordinate systems are the same between the models. Hence, the metadata from a particular location has been extracted without any associated issues in mismatch between the coordinate systems. After obtaining all the required stress fields, Eq. (3.5) is used to calculate the predicted life for the crack to grow to a critical length in the presence of the predicted residual stress fields. The crack growth (a) vs number of cycles (N) for the two zones are as shown in Figure 3.9.

As shown in Figure 3.9(a) and Figure 3.9(b), the variations in residual stresses from the process modeling efforts, analogous to part-to-part variations, have resulted in variability or scatter in the estimated life at the two zones of interest. The inclusion of predicted behavior definitions within the design definition, and its exchange using the CAD models for forecasting component performance, has been enabled by the developed tool. By doing so, the potential for a network of models that define the component's behavior under particular operating conditions exists, which would begin to form the as-designed digital twin of the turbine disk by closing the loop between design, manufacturing and use. After the disk components are retired from application, the collection of digital material behavioral attributes embedded in the CAD models contribute as a source of knowledge for design, repair, or re-design activities. By comparing the performance of the as-built disks, the variations can be evaluated for two purposes:1) to inform the decision-making during design and manufacturing of the newer disk component, and 2) to update and improve the accuracy of existing predictive models used in the digital twin framework. By analyzing a representative sample of disks according to similar techniques, after they have been removed from use at end of life (as-used), additional behavioral and contextual data can be gathered to increase the accuracy and validity of the product's model-based definition.

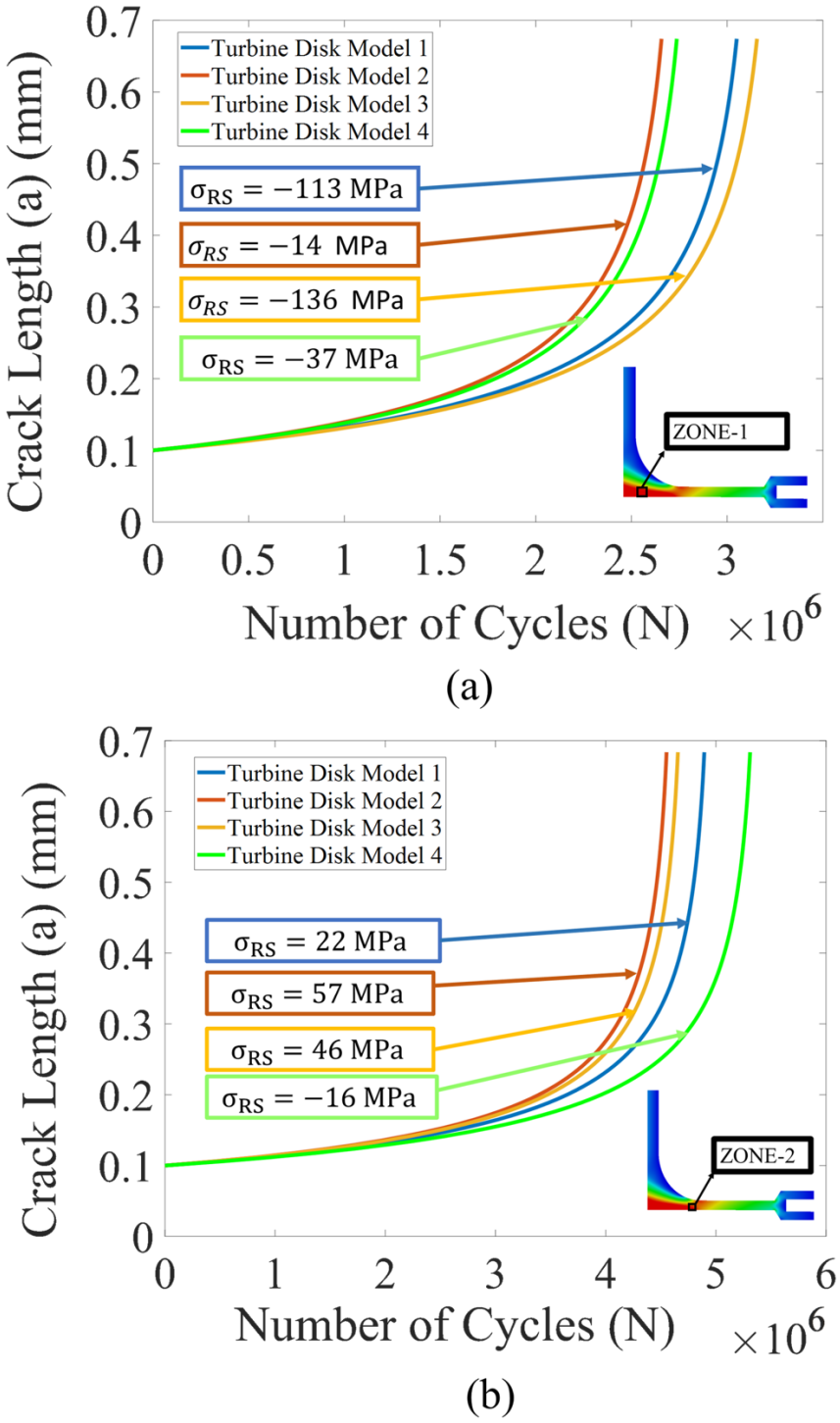

Figure 3.9. Crack length versus number of cycles in the two critical locations: (a) Zone 1 and (b) Zone 2, including the resulting variability in performance based on the part-to-part variation of the residual stress fields.

The use case presented in this section demonstrated the capability of the developed tool to integrate material behavioral definitions into CAD models during the design stage in order to enable the as-designed digital twin. However, this capability of integrating models and exchanging stored lifecycle definitions (as shown in Figure 3.10), from one model to another, can be incorporated to form the as-built digital twins or virtual replica of a produced component [71]. During the manufacturing of turbine disk components, geometric variations are inevitable, originating from the manufacturing process variability. The geometric variations in the manufactured disks can be directly measured and modeled by creating varying geometric instances of the CAD models, representing serialized part numbers for each disk of the as-built geometry and the model-based definition of the residual stress distributions (given the geometric variation). By being able to associate material characterizations to geometric definitions in specific places on the topology of the model, the ability to track that connection through the lifecycle becomes easier and less prone to error.

Using the procedure to evaluate the location-specific, damage-tolerant fatigue life, in-service inspection schedules can be formulated uniquely for each manufactured disk - governed by their underlying residual stress distributions. For example, inspection and maintenance intervals are typically planned and performed at 50% of the remaining predicted life [72]. Based on the knowledge of the as-built geometry and corresponding model-based definition of residual stress for this geometry, a reasonable interval for inspection and maintenance can be identified with a reduced level of uncertainty for each serialized disk (Figure 3.10). As shown in the present use case, the embedding tool can enable this propagation of process models (in this case residual stress analysis) to downstream performance analysis (e.g. damage tolerance analysis of the fatigue lifetime).

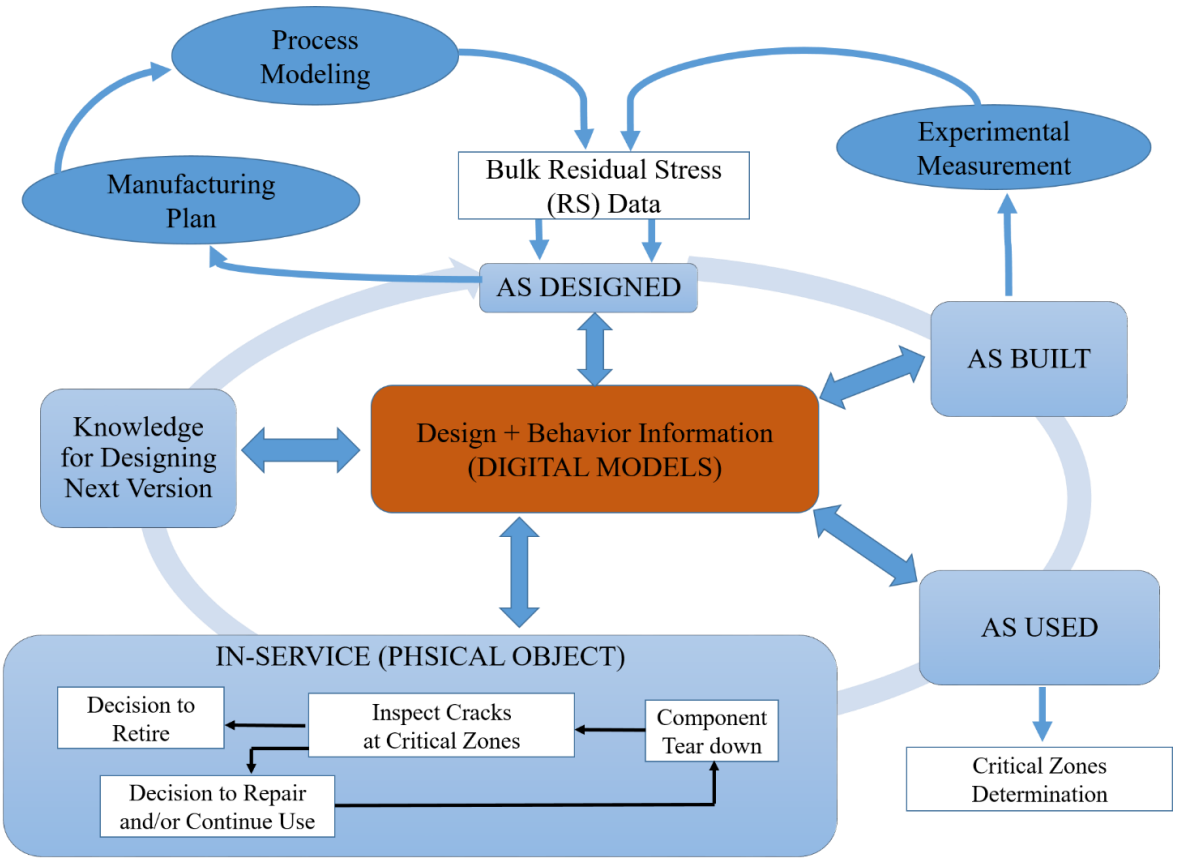

Figure 3.10. Diagram representing the flow of data across the product lifecycle using digital models.

4. DATA LINKING FRAMEWORK VIA A MODEL-BASED FEATURE INFORMATION NETWORK (MFIN)

The content of this chapter were published in Gopalakrishnan S, Hartman NW, Sangid MD. Model-based feature information network (MFIN): a digital twin framework to integrate location-specific material behavior within component design, manufacturing, and performance analysis. Integrating Materials and Manufacturing Innovation (2020) 9(4):394-409.

For creating dynamic connectivity to materials information as the information evolves continuously or periodically across the product lifecycle, the earlier developed data embedding approach presents a few key challenges. Firstly, the embedding methodology would require the creation of new instances of MBD-CAD models, for capturing each new revision/update to a component's material data. This might result in a collection of a large number of MBD-CAD instances over the entire product lifecycle and would require manual version controlling to precisely retrieve relevant information for downstream analysis. Furthermore, from a collection of stored MBD-CAD models, an instance could either contain the updated material information from a newer stage of a serialized component's lifecycle or could also contain definitions associated to another serialized version of the same component. There exists no systematic means to interpret the context of information captured in each of the MBD-CAD instances and is highly dependent on how the data is structured and stored. In order to address these challenges, a framework with data linking mechanism has been developed, namely the model-based feature information network (MFIN). Herein, we still use the earlier developed point cloud methodology to associate material definitions to spatial locations within the component, however the material information is stored and updated externally within a materials database software and linked to individual locations in the CAD model by means of the developed linking strategy, presented in this chapter in Section 4.1. Additionally, the access to material datasets within structural analysis tools is also enabled via the MFIN framework, which is presented in Section 4.2. A use case to demonstrate the MFIN framework has been presented in Section 4.3, followed by discussion regarding the scope of MFIN framework to ultimately enable digital twin in Section 4.4.

4.1 MFIN Framework Methodology

The MFIN framework has been created by expanding an existing model-based definition capability for storing and exchanging quality inspection data, provided by an ANSI standard, namely the Quality Information Framework (QIF) 2.1 [73]. The primary focus in this section is to describe the MFIN framework and illustrate the implementation of the MFIN to enable storing, retrieving and updating of material definitions and structural analysis information, with an emphasis on location-specific material data. With the motive of introducing the implemented framework, the current section describes: (a) necessary background on the existing QIF framework and its data structure, followed by (b) expansion of the framework to develop linking mechanism between features and externally stored material datasets and analysis information.

The premise for choosing QIF as the baseline for developing the MFIN is due to the advantages offered by the framework to define feature specific information. QIF is a data model in the form of a neutral file format, namely extensible markup language (XML) (herein saved as a ".qif" file), which is obtained by converting the model definition of a component in a CAD model to an equivalent definition in XML. In the current demonstration, Siemens NX 11.0 CAD tool [74] is used, while the framework is general to integrate any commercial CAD tool. The translation of CAD to QIF is performed using a tool, namely MBDVidia [75], which converts the geometry, geometric features, geometric tolerances, and metadata associated to these features (including manufacturing information (PMI) [73]) to the XML definitions. Being a neutral file format, which is both human and machine readable, the QIF file can be used as an input for providing both the component geometry and associated metadata to several applications and systems. The data structure and mechanism used by QIF to leverage storing, indexing, and retrieving feature specific information has been utilized to expand the framework to develop the MFIN – to include additional product lifecycle data. Lastly, the QIF data model is supported by the International Organization for Standardization (ISO 23952:2020) as a recognized standard for authoring, storing, and exchanging information [76].

Within the QIF file, the structure and organization of the data elements and their associated datatypes is defined by its XML schema documents (XSD documents) [73], similar to other standard XML documents. The data within the QIF file is governed by two categories of schemas, namely QIF libraries and QIF applications. The QIF libraries schema contain structure of the data elements to define the product's geometry (e.g. points, curves, surfaces, etc.), topology (e.g.

vertices, edges, faces, etc.), as well as the features which are defined using the geometry (e.g. hole, pocket, thread, fillet, etc.). Whereas, the QIF applications schema is intended to describe the structure of the data elements for the product lifecycle metadata, which currently include schemas only for capturing inspection and measurement datasets. For extending the framework to include additional product lifecycle metadata and creating the MFIN, the existing QIF applications schema were appended with new schemas to define the structure of the data elements, which are collectively referred to as MFIN application schemas. All the XML data elements, which are generated following the QIF libraries schema and MFIN applications schema are grouped together within a top level element, namely, the QIFDocument [73], which creates a single QIF XML document (from here on referred to as MFIN XML).

In order to create logical relationships between the product lifecycle metadata and the associated features within the MFIN XML, a mechanism used by the existing QIF framework is to index data elements with unique identifiers. Firstly, in order to enable serialization and tracking of the datasets applicable to each individual component, the schema defines a unique identifier to its corresponding MFIN XML document. These identifiers are generated during the creation of MFIN XML as Universally Unique Identifiers (UUID) objects made of 128-bit numbers that follows the RFC 4122 standard [77]. An example of UUID is "25244977-74f1-4ba8-adea-2f7ef0367888". Secondly, every data element within each MFIN XML is indexed with a local identifier using a positive integer that take values incrementally as new data elements are added. These local identifiers can be used for cross referencing a data element within other data elements. Following this approach, each feature receives a local identifier used for referencing the specific feature within a product lifecycle metadata element, in order to establish a relationship between the metadata and the feature. Finally, the collection of local identifiers of all the metadata elements, with reference to a specific feature, form a network of lifecycle data mapped to all possible features, which can be used for tracking and extracting the feature specific datasets.

While creating new MFIN application schemas to include new metadata, an important factor to be considered is the choice of storing metadata externally in databases, local hard drives, or network drives. The associations between externally stored datasets and features within the MFIN XML have been created using a data linking mechanism. The choice of storing datasets externally and creating linkages to the MFIN as opposed to storing datasets directly within the MFIN has been made due to the following advantages. Firstly, it enables a dynamic capability

wherein the externally stored data can be updated, and the revised data can be tracked and retrieved at any given point of time. Secondly the voluminous data across the lifecycle can lead to an oversized single file, while storing directly, which can be avoided by linking data and creating a smaller sized MFIN file that is easier to share and exchange. Within the overall MFIN framework, provision for different definitions of a linkage have been accommodated, such as using a web hyperlink for cloud storage, file path of the files stored in local hard drives or network drives, or data identifiers specific to a database utilized for storing the datasets. For the current implementation, materials information is stored in material database software and information pertinent to structural analysis is stored on a local hard drive. Correspondingly, two new schemas have been created, namely (i) *MFINMaterialDefinition.xsd* and (ii) *MFINAnalysis.xsd*, to facilitate the necessary data linkages.

(i) The *MFINMaterialDefinition.xsd* schema defines the data structure based on the methodology for organization of datasets that prevails in the material database tools. A common structure within material database tools were the use of Graphical User Interface IDs (GUIDs) to reference individual material records and "Attribute IDs" to reference individual material datasets within each record. Hence, the *MFINMaterialDefinition* schema has been defined to create material definition linkages by grouping the material GUIDs and Attribute IDs with the corresponding local identifiers of features within the MFIN. This linking strategy enables using the flexibility of storing material datasets of different datatypes such as tabular, functional form, images or raw data files within the materials database. Furthermore, the data linkages are independent of the schema or the structure in which the datasets are organized and stored, since they are only dependent on the data identifiers. A common structure or schema is preferable to record and pass the material datasets without ambiguity, especially across supply chains. For instance, in the case of multiple material vendors, the material datasets and pedigree information can be stored following a common structure to ensure seamless tracking and reviewing of datasets. User-defined schemas can be created to structure and store datasets in the material databases and these datasets can be seamlessly exchanged across the lifecycle via the data linkages enabled by the MFIN. Additionally, the access restrictions typically applicable to material datasets, can be controlled by the access control filters in the materials database tool, while the MFIN only provides the paths to the data. The new schema has a provision for including metadata related to access control restrictions, user details, date and time of linkage creation for tracking purposes.

(ii) The *MFINAnalysis* schema defines a new *MFINAnalysis* element, which is created within the MFIN XML, for each performed analysis. In each of these data elements, the sub-elements primarily include the linkages for the analysis input file and the overall results file, which are stored either in the local hard drive (a link defined by the file path) or within the materials database (a link using a material GUID and the corresponding attribute ID). Being a data linkage, these files can be of any format either depending on the analysis software being used or customized result files generated by the user. Furthermore, within the schema, metadata elements capturing the type, date, and time of the analysis have been included.

In order to create new data linkages in MFIN XML, as well as retrieving information using the existing linkages, application program interfaces (APIs) or MFIN APIs have been created for enabling programming against the developed schemas. The current framework uses Python scripts to link to the developed APIs, thus the framework is software tool agnostic and can work with a multitude of commercial softwares. For every data element within the schemas, an API has been generated in the form of a Python class, using an automated process of generating source code binding [78]. Using the MFIN APIs, wrapper code(s) were developed for creating new linkages and retrieving datasets using existing linkages, which have been used for integrating the MFIN framework with materials database tool and structural analysis tool [79].

4.2 Integration of materials information and structural analysis within MFIN

The integration of materials databases within the MFIN framework was implemented and tested with two materials database tools, namely Granta MI [80] and MSC MaterialCenter [81]. Both databases have their own APIs to enable programmatic storing and retrieval of materials datasets. For the current demonstration, Granta's materials database is used. A wrapper code has been developed using Granta's APIs to generate a user interface, which facilitates browsing the database and selection of the material definitions, in order to create material definition linkages (i.e. the material record GUID and the Attribute IDs) to exchange via the MFIN APIs within the MFIN XML.

Material definitions apply to the bulk of the component, hence requiring the creation of linkages to volumetric features within the MFIN. The currently available volumetric feature definitions comprise of typical geometries originating from the CAD tools, which are defined using its bounding surface entities (e.g. a cube is defined using its bounding faces made of edges

and vertices). However, since the material definitions could potentially vary spatially across the volume of a component, a new mechanism to define these features has been adopted within the MFIN framework. The approach uses datum points to define these features, since points (i) are the most fundamental objects in 3D modeling and (ii) enable defining individual locations within the volume for defining location-specific properties. The MFIN schema defines the PointClouds to generate the datum points, which do not necessarily get used for defining the geometry but can be used for the material definition associated with each point. In order to programmatically create the point features, a code has been created using the MFIN APIs, which accepts input point datasets (i.e. its spatial coordinates, X, Y, Z). These point datasets are supplied using a text file or a comma-space valued (CSV) file to the program. Hence, the process of creating material definition linkages to the spatial locations within the component is a semi-automated process, such that the material datasets for the selected spatial points are identified using the previously described wrapper code to browse and select the material definitions from the materials database. As opposed to generating the point clouds programmatically while creating data linkages, alternatively, the creation of datum points can also be accomplished with the original CAD model, which are translated while generating the MFIN XML.

The integration of the MFIN framework with finite-element (FE) analysis tools enables the exchange, storage, and retrieval of structural analysis results based on the component geometry and material definitions within the MFIN. The overall software architecture for this data integration is shown in Figure 4.1. The integration of structural analysis within the MFIN framework was implemented and tested with two FE tools, namely MSC Patran/Nastran [82,83] and Dassault's ABAQUS [84]. The APIs specific to the FE tools have been used to complete the implementation and ensure the importing/exporting functionalities of data. For the current demonstration, Dassault's ABAQUS is shown.

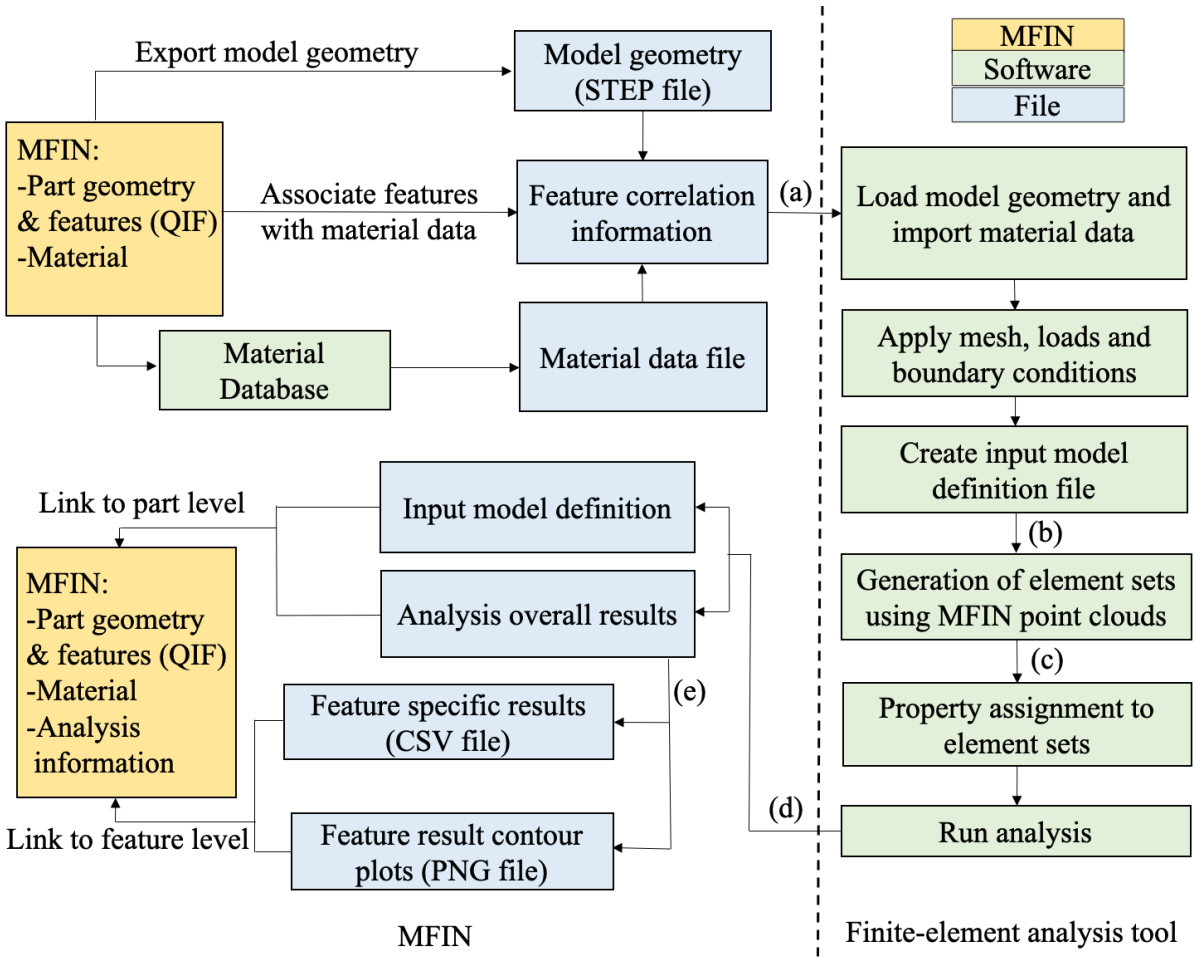

Figure 4.1. Software architecture for integration of the MFIN with a FE analysis tool, with programmatic steps to (a) import analysis model geometry and material data within the FE tool, (b) overlay point features on the analysis model mesh, (c) extract and incorporate material data linked to the point features within a user defined material model, (d) exporting analysis input and results files from the FE tool, and (e) generate feature specific results.

The analysis model generation process has been developed as a semi-automated process, to retrieve the component geometry and material definitions from the MFIN XML (as shown in Figure 4.1(a)). The process is initiated from the FE analysis tool, using a user input form that requires two inputs, namely (a) the location of the MFIN XML file and (b) the MFIN UUID. First, the model geometry is retrieved from the MFIN for importing within the FE tool. Due to the current limitations with the FE tool to directly import the model geometry using a QIF file format, an alternative neutral file format, namely ISO STEP AP 214 [85] has been used. The STEP file is generated by translating the native CAD file, which has been done using the in-built STEP translators in Siemens NX 11.0 CAD tool and linked to the MFIN XML via the file's location.

Next, the materials definition linkages within the MFIN are utilized to dynamically retrieve the materials data from the database in a CSV file format. For each materials data file that gets generated, the corresponding feature information (including point features) is retrieved from the MFIN for use within the structural analysis tool. Both the features and the material data file paths are grouped and stored in a feature correlation file, which informs the relationship between the spatial position and the material datasets within the imported STEP geometry.

After importing the model geometry and material data files within the FE tool, the analysis model is manually meshed, loads and boundary conditions are applied, following which an input model definition file (INP file) is generated. For incorporating location-specific material definitions in the analysis, firstly, the point cloud features are programmatically extracted from the feature correlation file and overlaid on the analysis model mesh (shown in the step in Figure 4.1(b)). Afterwards, the mesh elements are mapped to the nearest point feature from its centroid position, thereby picking and applying the material data linked to the corresponding point feature in semi-automated fashion. Based on the analysis requirements, a customized script is to be used (shown in the step in Figure 4.1(c)), to utilize the location-specific material data within the material model. Since the retrieval and utilization of materials information within the analysis is programmatically executed via the MFIN point clouds with minimal human involvement, the MFIN enhances the analysis process by reducing chances for human in the loop errors, as well as significantly decreasing the time for generation of an analysis model.

At the end of an analysis, the input file (INP file) and the overall results file (ODB file) are exported from the FE tool (as shown in the step in Figure 4.1(d)) and archived by creating new linkages within the MFIN, following the *MFINAnalysis* schema. Additionally, if feature specific result files and plots are extracted using the overall results file (shown in Figure 4.1(e)), linkages are generated to the corresponding features within MFIN XML. Once the linkages for analysis information are created within the MFIN, these datasets can be retrieved and used for lifecycle analysis, as illustrated with a use case in the next section.

4.3 Use Case: Analysis of a Ti-6Al-4V compressor blisk

A linear friction welded (LFW) [86] bladed-disk component, also referred to as blisk, is demonstrated as a use case for the MFIN framework to include spatially varying material definitions for incorporating within damage tolerant analysis. The intent is to emphasize that the

presented methodology for including and exchanging location-specific material information can be utilized to provide material state information across a component to inform life predictions. For the present use case, a Ti-6Al-4V blisk is used based on its geometric complexity and location specific material state near the weld. The LFW process results in steep thermal gradients across the weld region, leading to the generation of spatially varying microstructures and residual stresses across the weld region [86–89]. While the current section presents a demonstration of the MFIN applicability, the material's data is obtained from past studies published in the literature [89–91]. Using the MFIN framework, the microstructural information and residual stresses is spatially linked within the component's geometric model for subsequent damage tolerance analysis. One of the fundamental tenets of the digital twin is that by including this updated material state definitions, the resulting uncertainty in the subsequent lifing analysis can be reduced. Accordingly, a comparison has been performed to demonstrate the variations generated in the resulting fatigue life with and without using location-specific material definitions.

First, a blisk component with 48 blades was created as a CAD model, with approximate geometric dimensions similar to [92]. Since the blisk sections are axisymmetric about the *z* axis, $1/48^{th}$ of the blisk was modeled, as shown in Figure 4.2(a)-(c). For the axisymmetric portion of the component, three features were defined: the disk, weld region, and blade as shown in Figure 4.2(c). The disk section was modeled as a 2D sketch in *x*-*z* plane as shown in Figure 4.2(d), which was revolved by 7.5° about the *z* direction. The weld region and the blade region were modeled as shown in Figure 4.2(e) and Figure 4.2(f), respectively. Within the weld region, a datum reference frame X-Y-Z has been defined, which is used for defining location-specific material definitions. The origin of this new reference frame is situated at the center of the weld region, with the X axis orthogonal to the weld interface (Figure 4.2 (e)). The CAD file was converted into derivative QIF (i.e. the MFIN XML) and STEP file formats.

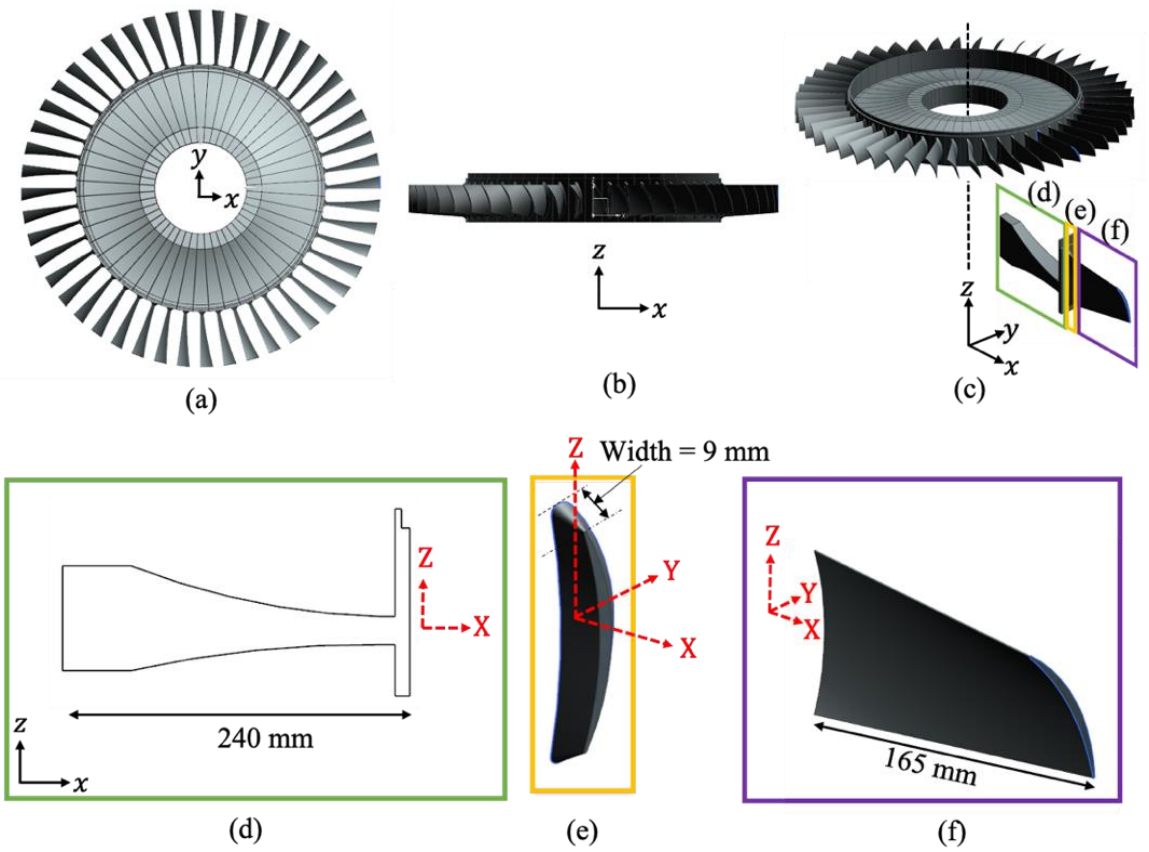

Figure 4.2. CAD model of the blisk component with different views, namely the (a) top view, (b) front view, (c) trimetric view along with 1/48th axisymmetric sector marked with the three features in the blisk, namely, (d) the disk region, (e) the weld region, and (f) the blade region.

A customized material record of Ti-6Al-4V was created within the Granta MI database and comprised of physical, elastic, and mechanical properties of the material, as well as spatially varying information across the component, which include residual stress field and the average grain size of the material relative to the LFW (based on characterization data reported in [89]). After optimal parameters were determined for linear friction welding of Ti-6Al-4V to Ti-6Al-4V plates [89], the average grain sizes (d_{avg}) for the globular α-phase was characterized at 7 locations across the weld region [89], as shown in Figure 4.3(a) and Figure 4.3(c). The average grain sizes, d_{avg}, of the microstructure were 1.65 μm at the weld interface and 9.62 μm, 8.90 μm, 11.06 μm, respectively, moving away from both sides of the weld center in a symmetric fashion [89] and these values were archived in the database. For the disk and the blade regions, a uniform d_{avg} value of 11.06 μm has been defined. Finally, the residual strain distributions characterized

in [89] were used to create the residual stress components ($\sigma_{xx}(X)$, $\sigma_{yy}(X)$, $\sigma_{zz}(X)$, for which the details are described in Appendix B), as a function of the distance from the weld interface (X axis), as shown in (Figure 4.3(b)).

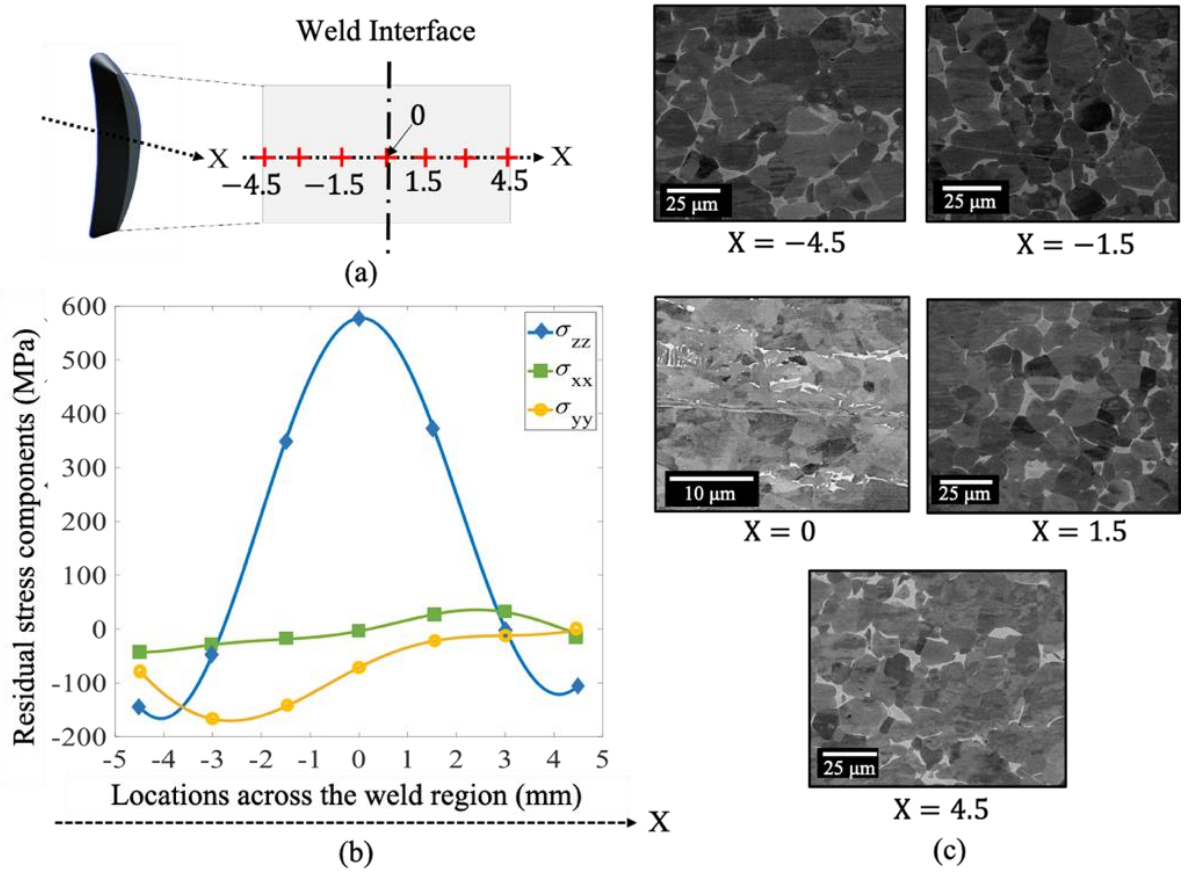

Figure 4.3. Spatially varying material definitions stored within the materials database and linked to the weld region in the MFIN using point features: (a) weld region with 7 locations linked to the average grain size information, (b) residual stress components (σ_{xx}, σ_{yy}, σ_{zz}) as a function of locations across the weld region in X direction, (values for the 7 locations shown here with markers), and (c) corresponding microstructure images (shown here for 5 of these locations).

By including the process induced residual stresses and microstructural information, more precise damage tolerant assessment of components can be determined [59,60]. First, the in-service stresses in the blisk were obtained using a structural analysis via the FE method, in which the average grain size information of the Ti-6Al-4V material is used to inform the constitutive response of the material. A simple elastoplastic material model has been chosen based on the Johnson-Cook [93] type hardening rule as shown in Eq. (4.1), wherein the flow stress ($\overline{\sigma}$) is a

function of the equivalent plastic strain ($\bar{\varepsilon}$) and temperature (T). The parameters A, B, n, m, T_{room}, and T_{melt} correspond to the yield stress, strain hardening coefficient, strain hardening exponent, temperature exponent, room temperature, and melting temperature, respectively, whose values used for Ti-6Al-4V [90,91] are shown in Table 4.1.

$$\bar{\sigma} = (A + B\bar{\varepsilon}^{n})[1 - \left(\frac{T - T_{room}}{T_{melt} - T_{room}}\right)^{m}] \quad (4.1)$$

Table 4.1. Material properties of Ti-6Al-4V at room temperature (T_{room} = 298 K) stored within materials database and linked to MFIN XML of the blisk component.

Material definition attributes	Attribute values
Density (ρ) (kg/m^3) [90]	4420
Young's Modulus (E) (GPa) [90]	114
Poisson's ratio (ν) [90]	0.33
Friction stress or resistance (A_{HP}) (MPa) [90]	783.14
Hall-Petch strengthening coefficient (K_{HP}) ($MPa.\mu m^{1/2}$) [90]	503.34
Strain hardening coefficient (B) (MPa) [90]	563.1
Strain hardening exponent (n) [90]	0.45
Temperature exponent (m) [90]	0.7
Melting temperature (T_{melt})(℃) [90]	1668
Paris' law coefficient (C) ($\left(\frac{mm}{cycle}\right) / MPa\sqrt{mm}$) [91]	$3.98\ X\ 10^{-17}$
Paris' law exponent (n) [91]	6.88
Walker exponent (m) [91]	0.57

The grain size dependency has been incorporated in Eq. (4.1) wherein the yield stress (A) follows a Hall-Petch [94,95] relationship as shown in Eq. (4.2). The friction stress (A_{HP}) and the Hall-Petch strengthening coefficient (K_{HP}) values for Ti-6Al-4V [90] are shown in Table 4.1.

$$A = A_{HP} + K_{HP} d_{avg}^{-\frac{1}{2}} \tag{4.2}$$

Two FE models have been created: (Model 1) considering a constant average grain size for the entire blisk of 11.06 μm and (Model 2) incorporating location-specific grain size information across the weld region. The variations in the average grain size and the corresponding yield stress (A) (computed using Eq. (4.2)) across the weld region, for the two models, are shown in Figure 4.4(a). Herein, the A values are computed dynamically by extracting the d_{avg} values from the database using the MFIN linkages while creating the analysis model.

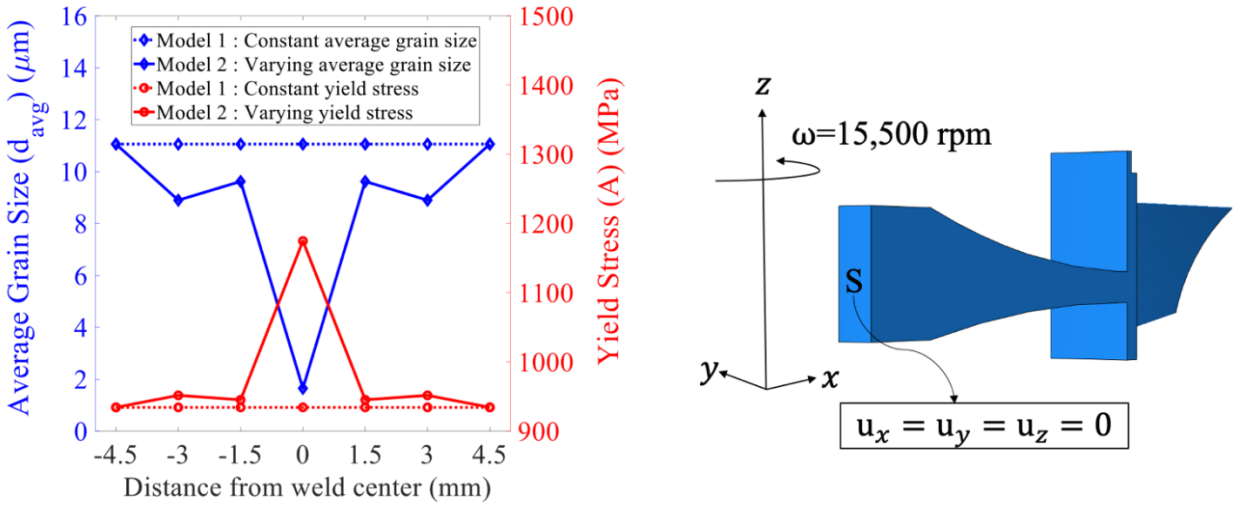

Figure 4.4. Material definitions, applied loading, and boundary conditions for the finite-element analysis model: (a) for Models 1 and 2, the average grain size (d_{avg}) and the corresponding Johnson-Cook model's yield stress (A) parameter defined at different locations across the weld region and (b) axisymmetric model of blisk with centrifugal load about the z axis and fixed displacement boundary conditions defined on the disk region's inner surface labelled as S.

The compressor blisk was simulated from its rest condition to an overspeed condition above its typical maximum rotational speed [64] during service for the present demonstration. To acquire the maximum loads, a static analysis has been performed on an axisymmetric sector of the blisk ($1/48^{th}$ of the blisk), as shown in Figure 4.4(b). A centrifugal load has been applied on the blisk about the *z* axis, with a spin speed of $\omega = 15{,}500$ rpm at room temperature (Figure 4.4(b)). The shrink fit loads, due to the interference fit between the shaft and the blisk, have been ignored in the current analysis. For the boundary conditions, a displacement constraint has been applied on the inner surface S of the bore, in all the three directions ($u_x = u_y = u_z = 0$) (Figure 4.4(b)). Firstly, due to the complexity in the blisk geometry, especially in the weld region (which is also of primary interest in this study), a mesh constituting quadratic tetrahedral elements has been used for this region (the use of quadratic elements also provides higher resolution due to additional integration points as compared to linear elements). Further, to ensure a conformal mesh near the interfaces between disk and weld as well as weld and the blade region (i.e. to avoid distorted tetrahedral elements in the disk and blade region near their interfaces with weld region), linear hexahedral elements were defined throughout for the disk and the blade regions. Hence, a combination of hexahedral and tetrahedral elements has been used for the entire blisk. Based on a sensitivity analysis performed by running a series of simulations by decreasing the mesh element size until the maximum principal stresses in the locations within the weld region did not change with further element size reduction (i.e. a converged mesh), linear hexahedral mesh elements of average size 0.5 mm were determined and used in the disk and blade regions, while quadratic tetrahedral mesh elements of average size 0.7 mm were determined and used for the weld region. Additionally, due to the different mesh types used, tie constraints have been applied between the interfacial regions of the disk and weld, as well as the blade and weld. Lastly, the residual stresses were not included in the FE model; for simplicity, this information is reserved for the damage tolerant analysis that follows.

At the end of the FE analysis, the analysis input and output files for Models 1 and 2 have been stored in a local hard drive and archived as file linkages within the MFIN. The stress fields were extracted for all the three regions of the blisk component, and the maximum principal stresses (σ_I) were computed for each element for both the models (shown in Figure 4.5(a)). The σ_I values were stored within the Granta database along with the associated centroidal positions of the elements. In order to visualize the variation in the maximum principal stress distribution across

the weld region, between the two models, a line scan along X direction (shown in Figure 4.5(a) and same as shown in Figure 4.3(a)) was performed to probe values, which is shown in Figure 4.5(b). The values were probed at 0.5 mm interval, wherein the maximum principal stress at a particular location was picked from the nearest elemental centroid position. The increasing trend observed in maximum principal stresses along X for both Models 1 and 2 (Figure 4.5(b)) was as expected since (i) the applied centrifugal load is a function of radius and it increases as we move radially outward (i.e. along +X direction) and (ii) the blisk section area is thinner as we move from disk to weld to blade region. Between Models 1 and 2, since the average grain size variations and correspondingly the variations in yield stress are maximum at the center of the weld region (Figure 4.5(a)), one would expect to observe significant differences in the maximum principal stresses at this location (i.e. at X = 0). However, in the present loading scenario, the locations near the weld center does not experience yielding and since the grain size dependency in Model 2 is active only after yielding, the differences observed in resulting stresses between the two models are not necessarily highest at the weld center. Furthermore, yielding is experienced in the locations within the weld region closer to the blade region. Although, at these locations, the variations in σ_I (Figure 4.5(b)) between Models 1 and 2 are small in magnitude, as they possess minor variations in their yield stress as shown in Figure 4.5(a). However, due to equilibrium after the FE simulation, the differences in the maximum principal stresses between Models 1 and 2 are observed at other locations near the weld center (between X = 0 and X = 3).

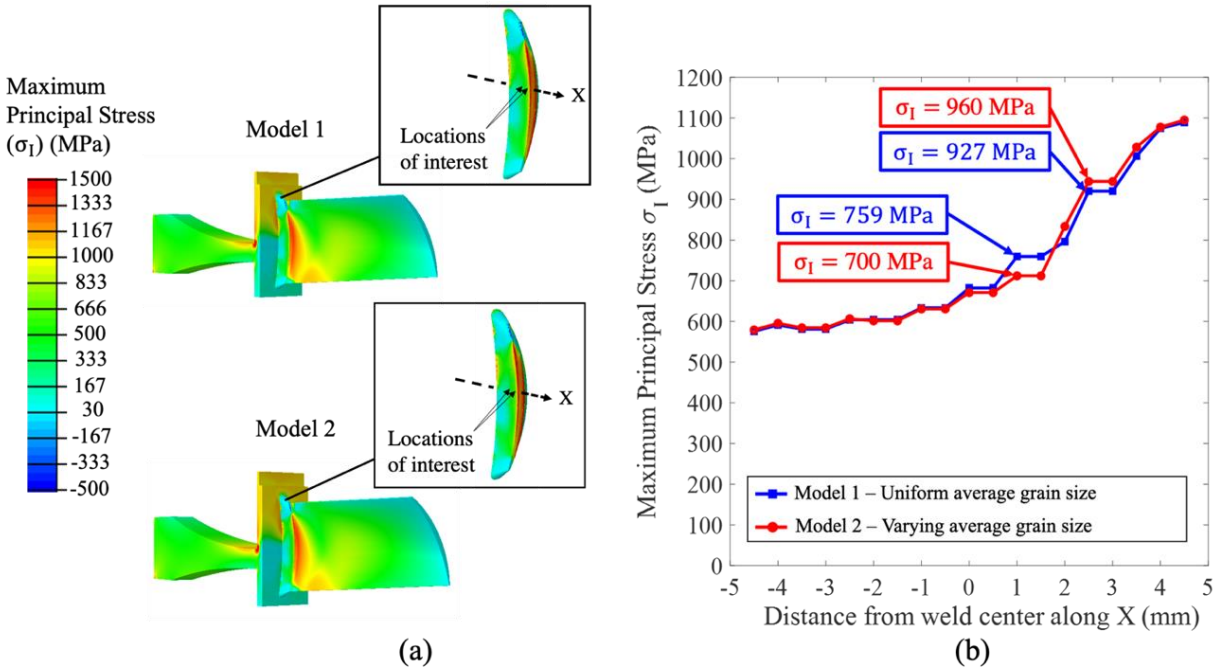

Figure 4.5. Maximum principal stress (σ_I) distribution generated in the blisk component: (a) contour plots for the entire blisk component using Models 1 and 2 (i.e. without and with using average grain-size information, respectively). The stress variation in the two models is very subtle and to articulate this minor difference, (b) shows the variation in σ_I across the weld region (along the X axis) for Models 1 and 2. The values of σ_I at the two locations of interest for damage tolerance analysis have been highlighted wherein the direction of σ_I is also oriented along the X axis.

A conventional damage-tolerance analysis [65] was followed (similar to the formulation in Section 3.4.2), which is typically performed at locations with high stress within the component, that are deemed as critical. At the selected locations, the presence of a crack is assumed, with an initial length a_i representing the largest flaw that can be missed during the inspection process. The crack is oriented perpendicular to the applied stress direction, such that the crack grows under the applied stress, following mode I crack growth. Typically, the number of life cycles for the crack to grow to a final crack length a_f, corresponding to the crack length at which the stress intensity (K_I) factor reaches the critical value related to the fracture toughness of the material (K_{IC}), is computed as the number cycles to failure. Conventionally, engine components are pulled out of service and inspected for a crack and if its length reaches 0.76 mm (1/33 of an inch), the component is retired and if otherwise, the components are returned back to service[96]. Hence, in the current

analysis, the number of cycles for the initial crack to grow to this standard length (herein $a_f = 0.76mm$) has been estimated, which can be used to decide and plan the inspection interval for the component under consideration.

Two locations have been selected from the FE analysis (shown in Figure 4.5(a) and Figure 4.5(b)) for placement of a crack. The first location was chosen wherein the difference in the maximum principal stresses between the two models (Model 1 and 2) was maximum. Hence, within the weld region, a location which is at a distance of 1 mm from the weld center along the X direction was selected, with values of σ_I being 759 MPa and 700 MPa for Model 1 and Model 2 (oriented along the X direction) (Figure 4.5(b)), respectively. The second location for the analysis was selected at a location wherein the tensile residual stress component is maximum along the maximum principal stress direction. For this purpose, a location at a distance of 2.5 mm from the weld center along the X direction (shown in Figure 4.5(b) with σ_I values of 927 MPa and 960 MPa for Model 1 and Model 2, respectively) was selected, wherein the direction of maximum principal stress was along +X and the corresponding component of residual stress (σ_{xx}) (shown in Figure 4.3(b)) was maximum. An embedded elliptical crack is assumed to be present at the selected locations, with initial length $a_i = 0.10\ mm$ (semi-minor axis length) and constant semi-major axis length of $c = 0.76$ mm. In both these locations, the direction of σ_I is to be oriented orthogonal to crack faces (representing an opening mode). Since the direction of the maximum principal stress is along the +X direction at both the locations, the crack plane is oriented parallel to the weld center plane (as shown in Figure 4.6(a) and Figure 4.6(b)), at a distance of 1 mm and 2.5 mm, respectively, along the X axis and propagating along the Z direction.

For estimating the number of cycles to final crack length (N_f) while incorporating residual stresses along with in-service stresses, the formulation presented in Eq.(3.5) has been used. The σ_{xx} component of the residual stress has been used as σ_{RS} for both locations of interest (since σ_I is along X). The values of σ_{RS} has been computed by first retrieving the functional form $\sigma_{xx}(X)$ from the materials database and evaluating for both the locations of interest (i.e. X = 1 and X = 2.5), with values $\sigma_{RS} = 16.68$ MPa and $\sigma_{RS} = 35.59$ MPa, respectively. For an embedded elliptical crack in the current case study, an approximate geometric correction factor from [97], has been utilized, which is applicable for crack lengths a much smaller than the width of crack growth plane such as in the current case. The Walker exponent (m) and Paris constants (C and n) for Ti-6Al-4V at $R \sim 0$ and at room temperature have been used for the present analysis. Finally,

the crack length (a) versus the number of cycles (N) has been plotted for each of the locations as shown in Figure 4.6(a) and Figure 4.6(b). In each of these plots, the fatigue life curves have been generated for both the cases - with and without using location specific material definitions.

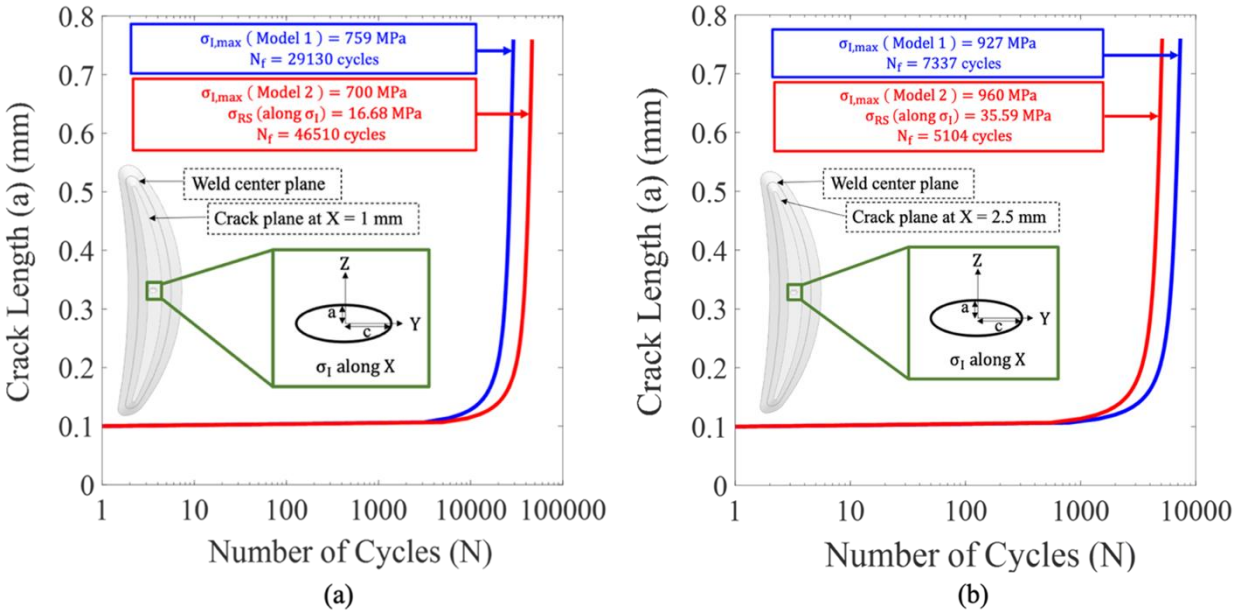

Figure 4.6. Variation in the crack length (a) versus number of cycles (N) between the two cases, without (shown in blue) and with (shown in red) using spatially varying average grain size and residual stress information for locations at a distance of (a) 1 mm and (b) 2.5 mm from the weld center along the +X direction.

4.4 Discussion

In Figure 4.6, the variation in the estimated fatigue life, (N_f), while including location-specific material information (i.e. average grain size and residual stresses) within the damage-tolerance analysis has been shown. For the two locations within the weld region considered in this analysis, we have demonstrated cases of overly conservative prediction (shown in Figure 4.6(a)) and potentially inaccurate prediction (shown in Figure 4.6(b)) of fatigue life while not including the location-specific material information in the analysis. In the present illustration, the uncertainty in estimating the number of cycles and corresponding inspection interval for a component in service, could be potentially reduced by including location-specific material information. The access to location-specific material information and its inclusion within the lifing analysis has been achieved by utilizing the data linkages enabled by the MFIN framework. The location-specific

definitions in the present use case were an outcome of the manufacturing process of the compressor blisk component, i.e., representing the underlying material state within the component at the end of its manufacturing. The inclusion of process-induced material state information, and its usage in performance analysis, demonstrates the usage of process-structure-property-performance relationship. Model 1 is the historical approach, which treats each portion of the blisk component as a monolithic structure in its approach to analysis. In Model 2, specific material location information is captured, via the MFIN framework, thus enabling a higher degree of precision in the design, production, inspection, and sustainment of the blisk. While the demonstration case is intended to provide a simple proof of concept, the MFIN framework enables the use of more sophisticated physics-based models by providing connectivity and therefore accessibility to pertinent process history induced materials information (undertaken in Chapter 5). By using the location-specific linking strategy presented in this work, the necessary material state information can be linked to specific component features, which reduces the uncertainty in our predictive models by harnessing the history and state of the material.

It is important to note that there are two viewpoints for defining the digital twin. One viewpoint suggests the requirement of a physical asset as a necessary ingredient prior to creating a digital twin, whereas the other viewpoint suggests that a digital twin or a digital prototype can be created before the physical production of a component or a system [4]. Other than this primary difference, both viewpoints share potential applications and benefits of the digital twin, which includes the usage of information at various stages throughout the life cycle and the fusion of modeling and simulation with physical testing and measurements. In this work, we did not necessarily want to exclude either definition, as our primary intent is to describe and illustrate the MFIN framework. For the present use case, we have illustrated the digital twin from an as-designed stage. Hence, the microstructural and residual stress state information have been included in the nominal part definition of the component. Additionally, the MFIN framework can be used to create digital twins after the production of the component, by following a similar approach including state information from the post-production stages.

The use of data linking approach meets the requirement for several critical elements, necessary for creating a digital twin. Specifically, the approach creates dynamic connectivity to material datasets, enabling tracking and providing updated data regarding the material state at any given point in the lifecycle of the component. The availability of the current material state

information can be utilized to make future predictions of the component's performance. In this work, the material data linkages have been used to provide material information to a commercial FE analysis code, for performing an analysis. Within the digital twin framework, the access to other commercial engineering software/code(s) which are useful for design and analysis of a component can be achieved by using necessary schemas and wrapper code(s). Herein, the material data linkages can be utilized to inform the material information pertinent to a component using an approach similar to the presented work.

Further, the methodology of linking, tracking and retrieving material data can be expanded to other datasets produced during different stages of the product lifecycle. Since the linkages are created between a feature and the information applicable at the feature, a network of lifecycle data applicable to the feature can be created by the MFIN. This starts to form a complete digital thread [98] of lifecycle data, which is necessary for supplying relevant information and creating the digital twin of the component. Hence, the MFIN framework would potentially complement data management systems, such as product lifecycle management systems [99], which are used to store product lifecycle data, by serving as a portal to access, exchange, and utilize feature specific lifecycle metadata. For retrieval of datasets specific to a feature, a user-interface can be developed (as shown in a schematic in Figure 4.7(a)), wherein the desired datasets can be retrieved using its feature's unique identifier. For instance, during the maintenance and repair of the component, an image of the component with a crack developed during its service, in a specific location (shown in an illustration in Figure 4.7(b) and Figure 4.7(c)) can be linked and accessed using the MFIN. During the design of the newer version of the component, the prior knowledge from the digital twins of predecessor components can be used to identify critical feature locations and explore newer opportunities to design and develop manufacturing processes for achieving desirable properties at these critical locations in the component.

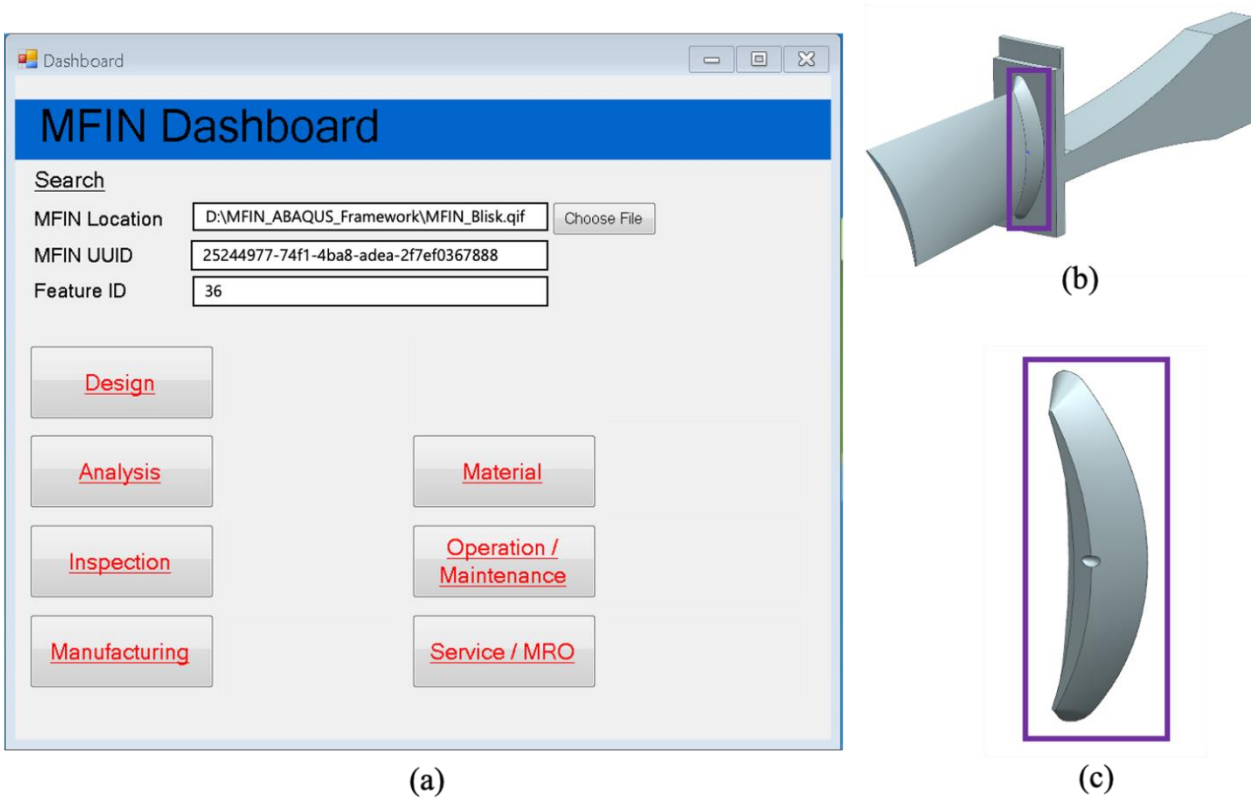

Figure 4.7. An illustration of using (a) a graphical user interface which can be created for the MFIN, to retrieve specific lifecycle data (for example maintenance data) applicable to either a specific feature and/or its component, by specifying its feature ID and UUID, respectively, leading to either (b) the retrieval of an image of the entire component (part level search) or (c) retrieval of an image of a feature (feature level search) with a crack detected during its maintenance and repair inspections.

5. ENABLING MICROSTRUCTURE-SENSITIVE LOCATION-SPECIFIC FATIGUE LIFE ASSESSMENT OF COMPONENTS VIA MFIN FRAMEWORK

The contents of this chapter have been submitted for publication in Gopalakrishnan S, Bandyopadhyay R, Sangid MD. A framework to enable microstructure-sensitive location-specific fatigue life analysis of components and connectivity to the product lifecycle. Submitted, under review (2022).

In the previous chapter, we introduced the MFIN framework, and demonstrated a simplified use case for incorporating location-specific material data within a damage tolerance analysis of a component. The dynamic linking capabilities for accessing location-specific material information within the MFIN framework can be leveraged for use within physics-based predictive analysis, thereby incorporating the local microstructural knowledge for fatigue life analysis of components. In this chapter, we extend the MFIN framework to dynamically track and retrieve location-specific (i) microstructural definitions, and (ii) in-service stresses/strains fields (from component level-FE analysis), for use within a crystal plasticity-based fatigue life prediction model. We present the expansion of the MFIN framework to create data linkages with information pertinent for crystal plasticity finite-element (CPFE) analysis in Section 5.1. We demonstrate location-specific lifing of a dual-microstructure heat treated (DMHT) turbine disk. The component geometry, manufacturing processing, and material's microstructural description are described in Section 5.2. The crystal plasticity-based fatigue life prediction framework is described in Section 5.3. A component-level FE analysis to simulate in-service stress/strain states is detailed in Section 5.4. Finally, we present the predictions of material allowable fatigue life, the location-specific fatigue life of the component, and considerations for the utilization of this overarching framework in Section 5.5.

5.1 Expanding MFIN framework to include information pertinent to CPFE analysis

In Figure 5.1, to provide a visual overview of the MFIN framework, we have summarized the types of information which can be potentially included, at both the component level and at the location-specific level. At the component level, we can capture the as-designed geometric definitions of the component and its features (from nominal CAD model), processing history,

loading conditions during service and deviations in the part geometry post manufacturing (from as-built CAD models) (presented later in Chapter 6). In Section 4.1 of Chapter 4, we presented the newly developed application schemas to define data linkages to externally stored (i) material datasets and (ii) datasets pertinent to finite-element (FE) analysis of the component. At the location-specific level, we had demonstrated linking and retrieval of microstructural attributes and mechanical properties in Chapter 4. In this chapter, we develop a new schema to include information relevant to sub-scale crystal plasticity finite element (CPFE) analysis for connectivity to specific locations within the component.

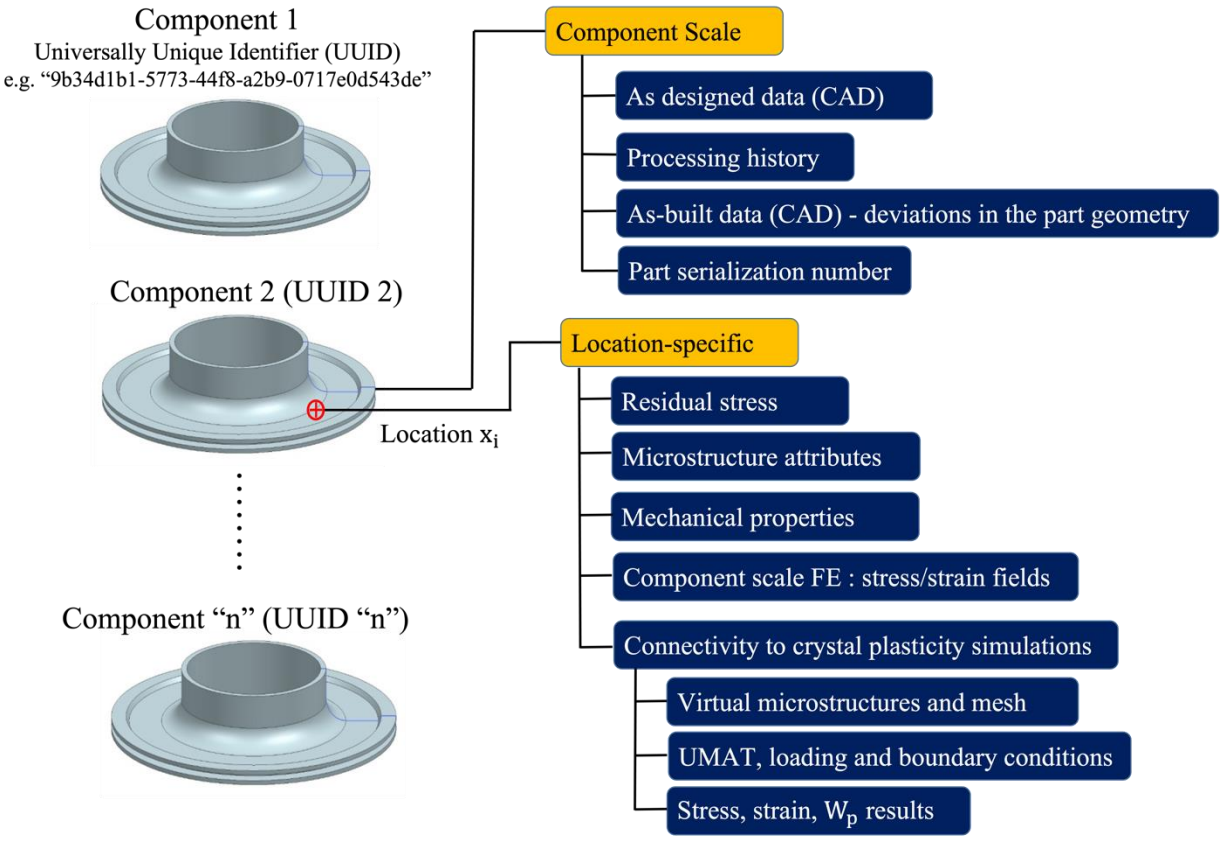

Figure 5.1. Information captured within the digital twins of serialized components and their individual locations via MFIN.

Hence, we have created a new MFIN application schema ("*MFINCPFEAnalysis.xsd*"). The "*MFINCPFEAnalysis*" element within the MFIN XML is linked to specific locations via point

features (using their corresponding local identifier). The sub-elements within the "*MFINCPFEAnalysis*" element have provisions to capture linkages to (i) the virtual discretized (fully meshed) microstructure (in .inp file format), (ii) grain-level information (i.e., files with grain identifiers, including grain orientations or Type II residual stresses), (iii) user-defined material sub-routine or UMAT file (.f file format) applicable for the CPFE analysis, (iv) boundary conditions to be enforced for the CPFE simulation, and (v) the resulting micromechanical field variables extracted from the CPFE analysis (Figure 5.1). A programmatic process has been developed to utilize component-level FE analysis results via the MFIN XML, to inform location-specific boundary conditions within CPFE analysis. Based on the location of interest (given by its position coordinates) within the component, the wrapper code extracts stresses/strain fields from the "*MFINAnalysis*" element and updates the sub-element capturing the corresponding CPFE boundary condition within the "*MFINCPFEAnalysis*" element. Hence, the MFIN framework enables hierarchical exchange of location-specific FE analysis results for conducting location-specific CPFE analysis, which has been demonstrated for fatigue life assessment of a DMHT turbine disk component.

5.2 Dual-microstructure heat treated (DMHT) disk: Component, material and methods.

To demonstrate location-specific fatigue life analysis of microstructure tailored components via the MFIN framework, we present a use case for lifing a dual microstructure heat treated turbine disk. In this section, firstly, the manufacturing process of the disk and characterization conducted in [40]. Next, we present the creation of the CAD model (and corresponding MFIN XML instance) of the component and the microstructure definitions across the disk. Finally, we describe creation of virtual microstructures for conducting location-specific crystal plasticity analysis.

5.2.1 Processing route and material characterization

The DMHT disk was manufactured via a powder metallurgy processing route followed by a specialized heat-treatment process [40,41,100,101] to produce fine grains in and surrounding the bore regions of the disk and coarse grains in and surrounding the rim regions. The disk component utilized for the present study was developed by NASA, and the production of the disk was conducted at PCC Wyman-Gordon Forgings (initial forging and machining) and Ladish Company

Inc. (specialized heat treatment) [40,41]. Initially, the LSHR powder of particle sizes < 55 μm was hot compacted and extruded into billets. The billets were isothermally forged, followed by machining, to obtain the disk with an outer diameter of approximately 30 cm, a maximum bore thickness of 5 cm, and a maximum rim thickness of 3.8 cm [40,41]. An initial sub-solvus heat treatment was conducted at 1135℃ for 2 hours, followed by air cooling to produce uniform grains across the disk with sizes ranging between $5-10\ \mu m$ [40,41]. Next, the dual microstructure heat treatment was performed, wherein a temperature gradient was maintained between the bore and the rim region by means of placing a heat sink [40,41] in the bore region. This resulted in the bore region with fine grain microstructures ($5-10\ \mu m$) and the rim region with coarse grain microstructures (30 – 80 μm) [40,41].

Grain size distribution and texture for LSHR at different regions of the disk were characterized using the electron backscattered diffraction (EBSD) technique by Gabb et al. [40]. The characterization was conducted at multiple locations within the transition zone in the DMHT disk, which is a region spanning between the bore and the rim region as we move radially outward, wherein the microstructure changes from fine grains to coarse grains. The average grain size for the transition zone near the bore region was 5.8 μm, with as-large-as (ALA) grain size of 22 μm [40]. The average grain size for the transition zone near the rim region was quantified to be 55 μm, with ALA grain size of 413 μm [40]. The characterized grain sizes in the near-bore region were reported to be similar to the bore region, and likewise, for the near-rim region to the exterior rim region [40]. Hence, in this work, we have consistently utilized an average grain size of 5.8 μm at the bore and the near-bore region and an average grain size of 55 μm across the rim and the near-rim region. The grain sizes followed lognormal distributions for both the bore and the rim region [40]. Additionally, in the central portion of the transition region, an average grain size of 38 μm was characterized, with ALA grain size of 410 μm [40]. Throughout the disk, we have defined a random texture, based on the characterization of LSHR reported in [40,102]. Within the MFIN XML, data linkages are created between these three regions and the associate grain size attributes, which are used for the crystal plasticity-based fatigue life predictions. However, we would like to emphasize that the framework allows for defining an unlimited number of regions; hence, more refined gradient structures can be realized. Moreover, the approach can be extended to incorporate other microstructure artifacts, such as grain boundary structure, precipitate distributions, and the likelihood of pores or inclusions, obtained via characterization [42] or modeling [103].

5.2.2 Creation of CAD model of the disk

For the geometric definition of the component, a CAD model of the DMHT turbine disk was created. We utilized the approximate geometric dimensions reported in [40] and also summarized in Section 5.2.1 to create a 2D axisymmetric section of the disk (shown in Figure 5.2(a))). The axisymmetric section was revolved about the Z-axis to generate the 3D CAD model of the DMHT disk as shown in Figure 5.2(b) and (c). The microstructural features are defined in the three regions (bore/near-bore, transition, and rim/near-rim) using semantic notes in the CAD model tagged to datum points within these regions, as shown in Figure 5.2(a). The CAD model and the associated notes were translated into MFIN XML file using the process described in Section 4.1 of Chapter 4. For this study, we have chosen two distinct locations, Location A (fine grain microstructure) in the bore region and Location B (coarse grain microstructure) in the rim region, as shown in Figure 5.2(a) and (b), respectively, with their associated microstructures - to conduct crystal plasticity-based fatigue life predictions. The locations were selected where the highest stress during service is expected (also verified later in Section 5 via component-level FE analysis) since there is a sharp change in the cross-section of the disk.

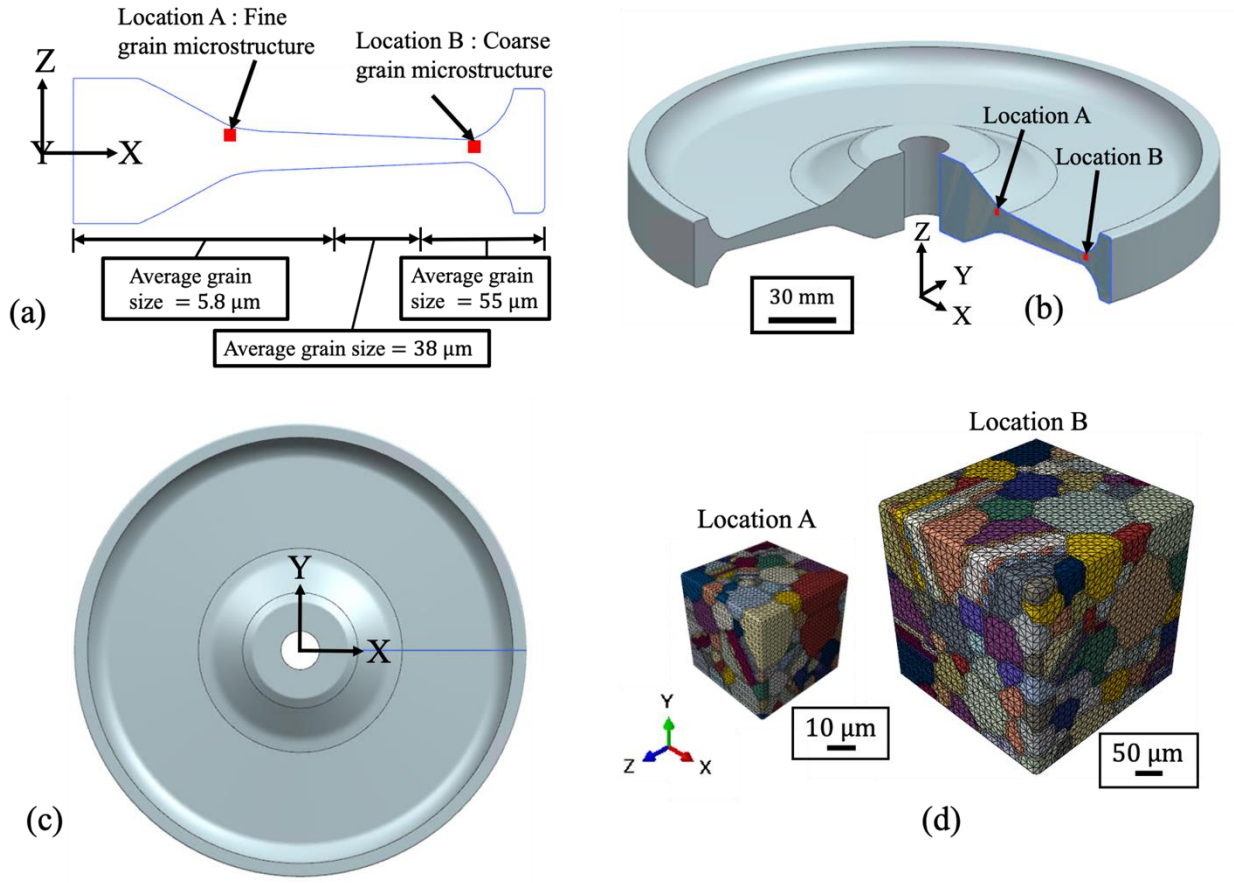

Figure 5.2. Dual-microstructure heat treated (DMHT) turbine disk component: (a) 2D axisymmetric cross-section of the disk shown with average grain size information varying from fine grains (average grain size = 5.8 µm) in the bore region to coarse grains (average grain size = 55 μm) in the rim region, (b) CAD model of the disk with a 270° trimetric view, (c) top view of the entire CAD model of the disk, and (d) discretized virtual microstructures corresponding to locations A and B.

5.2.3 Generation of location-specific discretized virtual microstructures

We utilized the grain size statistics reported by Gabb et al. [40] and summarized in Section 5.2.1, to create 3D synthetic virtual microstructures for both Location A (fine grain microstructure) and Location B (coarse grain microstructure). The detailed process for utilizing microstructure descriptors (grain size, texture, twin area fraction) and creating virtual microstructures, followed by mesh generation via a DREAM.3D pipeline is explained in [104]. Following this approach, we have generated multiple virtual microstructures, referred to statistically equivalent microstructures (SEMs), corresponding to each location, by ensuring that the grain sizes are statistically equivalent to the characterized values in [40]. For Location A (fine grain microstructure), 8 SEMs have been

generated with average grain size of 5.8 μm and the SEM domain size was 35 μm x 35 μm x 35 μm. For Location B (coarse grain microstructure), 8 SEMs have been generated with the SEM domain size was 325 μm x 325 μm x 325 μm. For both locations, each SEM consists of approximately 230 grains, based on a sensitivity study with respect to number of grains within the simulation volume and boundary conditions to fatigue life distribution [51]. Linear tetrahedral (C3D4) mesh elements were utilized to discretize the SEMs and the element sizes were chosen based on mesh sensitivity analysis conducted in [105], wherein a suitable choice of refined mesh satisfied the following criteria, $\frac{average\ element\ size}{average\ grain\ size} \leq \frac{3\ \mu m}{48\ \mu m} = 0.063$. In our case, an average element size of 0.33 μm was chosen for Location A and an average element size of 2.99 μm was chosen for Location B, which is in accordance with the criteria. The SEMs were linked to individual locations in the component via MFIN XML and utilized for conducting crystal plasticity finite-element simulations.

5.3 Crystal plasticity-based fatigue life prediction framework

Calibration of the model is necessary to conduct fatigue life predictions at two levels: (i) the crystal plasticity (CP) model parameters and (ii) the critical value of the fatigue indicator metric, known as the critical accumulated plastic strain energy density ($W^{p}_{critical}$). In Section 5.3.1, we introduce the crystal plasticity model utilized for this work, boundary conditions for CPFE, followed by the calibration of CP model parameters. Next, we elucidate the fatigue life prediction model using $W^{p}_{critical}$ in Section 5.3.2. Finally, we present the calibration of $W^{p}_{critical}$ parameter using experimental life datasets via a Bayesian inference approach in Section 5.3.3.

5.3.1 Crystal plasticity constitutive model and parameter calibration

The crystal plasticity model used in this work is based on the continuum mechanics description of slip via dislocation glide. The total deformation gradient ($\mathbf{F}$) at a material point can be described using a multiplicative decomposition into an elastic part ($\mathbf{F^e}$) (which captures the elastic stretching and rotations) and a plastic part ($\mathbf{F^p}$) (which captures the plastic deformation via crystallographic slip) as shown in Eq. (5.1).

$$\mathbf{F} = \mathbf{F^e}.\mathbf{F^p} \tag{5.1}$$

The velocity gradient ($\mathbf{L^p}$) associated with the plastic part of the deformation is related to $\mathbf{F^p}$ using Eq. (5.2).

$$\mathbf{L^p} = \dot{\mathbf{F}}^{\mathbf{p}}(\mathbf{F^p})^{-\mathbf{1}} \tag{5.2}$$

Further, $\mathbf{L^p}$ can be described using shear strain rate ($\dot{\gamma}^j$), slip direction $\mathbf{s^j}$ and slip plane normal $\mathbf{n^j}$ associated with the j^{th} slip system and summed over all the active slip systems using Eq. (5.3).

$$\mathbf{L^p} = \sum_{\mathbf{j=1}}^{\mathbf{12}} \dot{\gamma}^j \, (\mathbf{s^j} \otimes \mathbf{n^j}) \tag{5.3}$$

The shear strain rate ($\dot{\gamma}^j$) can be related to resolved shear stress (τ^j) on the j^{th} slip system using Hutchinson flow rule [106] and has a power law relationship as shown in Eq. (5.4).

$$\dot{\gamma}^j = \dot{\gamma}_0^j \left| \frac{\tau^j}{g^j} \right|^n \operatorname{sgn}(\tau^j) \tag{5.4}$$

$\dot{\gamma}_0^j$ and n are the initial shearing rate and the inverse strain rate sensitivity exponent, respectively. The reference stress (g^j) or the resistance to shearing offered by the slip system, which also evolves with plastic deformation, is described using a Taylor-type hardening law as shown in Eq. (5.5). g_0 is the initial slip resistance and ρ^j is the total dislocation density. The terms μ, b, and h_n represent the shear modulus, the Burgers vector, and a kinetics-based scaling parameter, respectively.

$$g^j = g_0 + b\mu\sqrt{h_n \rho^j} \tag{5.5}$$

The evolution of ρ^j is captured via a Kocks-Mecking [107,108] relationship (Eq. (5.6)), which constitutes a dislocation storage term, k_1, and a dislocation annihilation term, $k_2(\dot{\varepsilon}, T)$.

$$\dot{\rho}^j = \left|\dot{\gamma}^j\right| (k_1\sqrt{\rho^j} - k_2(\dot{\varepsilon}, T)\rho^j) \tag{5.6}$$

Finally, the constants k_1 and $k_2(\dot{\varepsilon}, T)$ are related using Eq. (5.7) [109] with the temperature T and the applied strain rate $\dot{\varepsilon}$. This relationship is applicable for dislocation glide mediated plasticity wherein $10^{-5} s^{-1} \leq \dot{\varepsilon} \leq 10^3\ s^{-1}$. Here, Γ_{act} is the activation energy term, k is the Boltzmann constant, $\dot{\varepsilon}_0$ is the reference strain rate, and D is a scaling constant.

$$\frac{k_2(\dot{\varepsilon}, T)}{k_1} = \frac{h_n b}{\Gamma_{act}}\left[1 - \frac{kT}{Db^3}\ln\left(\frac{\dot{\varepsilon}}{\dot{\varepsilon}_0}\right)\right] \tag{5.7}$$

Hence, in the crystal plasticity model, there are eleven parameters, which are to be calibrated using the experimental data. These include plasticity terms $\dot{\gamma_0}$, n, $g(0)$, $\rho(0)$, k_1, Γ_{act}, D, and h_n and the anisotropic elastic constants C_{11}, C_{12},C_{44}.

Prior to calibration of crystal plasticity model parameters, we introduce the two different types of boundary conditions (shown in Figure 5.3) for the CPFE analyses in this study. Firstly, for the purposes of calibration of the CP model parameters and critical value of the fatigue indicator metric, we utilize uniaxial boundary conditions for simulating the experimental test conditions as shown in Figure 5.3 (a). The normal displacements are constrained in three mutually orthogonal faces of the SEMs, corresponding to X=0, Y=0 and Z=0, respectively. A non-zero normal displacement is specified along the Y direction. The remaining two surfaces of the SEMs are unconstrained and act as free surfaces in the simulation. Next, for conducting the CPFE simulations based on the hierarchical component analysis to aid in the location-specific fatigue life predictions of the DMHT disk component, we utilize multiaxial displacement boundary conditions as shown in Figure 5.3 (b). As opposed to applying non-zero displacements along Y direction alone (i.e., on one of the surfaces) in the uniaxial displacement boundary conditions, we apply non-zero displacements on three mutually orthogonal surfaces (Figure 5.3(b)), along the X, Y and Z directions. Hence, all the six faces of the SEM are constrained in this case. The choice of displacements is determined via component-level FE analysis, by simulating the in-service loading conditions and retrieving location-specific strain states in the component (explained in Section 5.4).

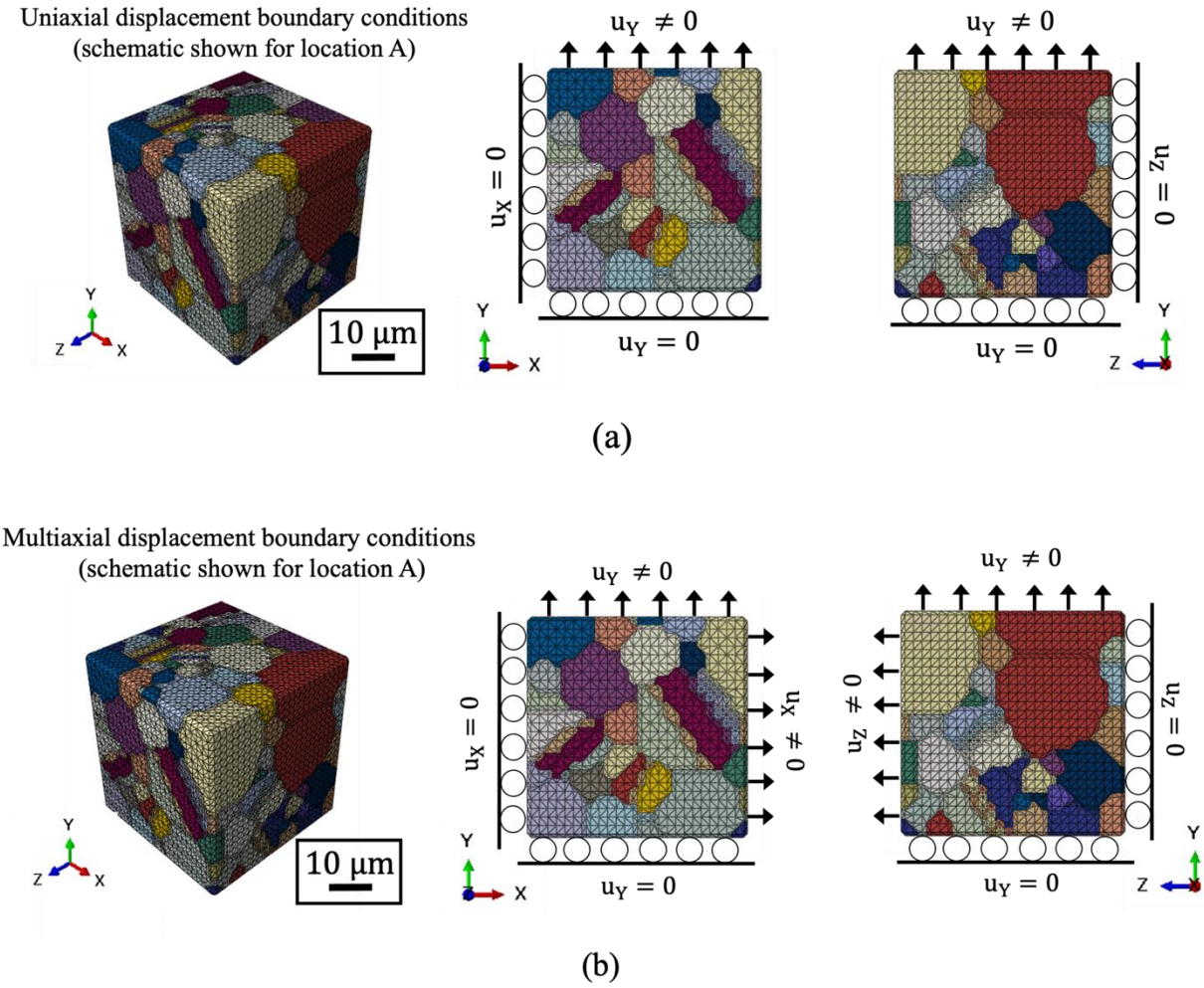

Figure 5.3. Boundary conditions for the crystal plasticity finite element simulations of the discretized microstructures: (a) uniaxial displacement boundary condition to simulate experimental loading conditions and (b) multiaxial displacement boundary conditions to simulate the applied strain state at individual locations in the component.

Linear tetrahedral (C3D4) elements are used to mesh the SEMs, which provides a conformal mesh but offers drawbacks. The values of micromechanical field variables from CPFE analysis is prone to spurious numerical oscillations arising from (i) volumetric locking [110], (ii) lack of mesh refinement near the grain boundaries resulting in steep gradients in field variables across grains, or (iii) poor quality of tetrahedral elements near grain boundaries and twin boundaries. To compensate for these aspects, a slip-system based averaging scheme, namely non-local averaging was proposed [51]. At each of the integration points of the finite elements, we consider three mutually orthogonal directions corresponding to the slip direction, slip plane normal,

and a transverse direction for the j^{th} slip system, which bound a cuboidal volume about a center coinciding with the integration point. The micromechanical field variables are averaged over all the elements whose centroids lie within the bounding volume. Since we are dealing with a FCC material, we have 12 active slip systems (i.e., j=12) and hence twelve such bounding volumes are considered for each integration point for averaging. Finally, after computing average values corresponding to each of the twelve bounding volumes, the maximum value amongst the averages is assigned as the slip-system averaged quantity of the micromechanical variable at the integration point of interest. In our current analysis, we have used an averaging volume of 5 - 3 - 3 elements along the slip direction - plane normal - transverse direction, which was determined via a sensitivity study in [50]. The averaging volumes are truncated to ensure the non-local average is contained within a single grain, e.g. does not cross a grain boundary. Additionally, to avoid spurious values in the micromechanical fields due to boundary effects, for all the CPFE analyses in this study, the micromechanical field values near the boundary conditions (approximately 5-element thickness) are discarded.

The fatigue analyses in this study are focused on a single isothermal temperature, 427℃, and due to the availability of data, the CP model parameters are calibrated at 593℃ with appropriate scaling laws to account for temperature dependencies. For each the fine grain and coarse grain microstructures, the CP model parameters, ($\dot{\gamma}_0$, n, g(0), $\rho(0)$, k_1, Γ_{act}, D, and h_n), were separately calibrated using uniaxial monotonic stress-strain data (Figure 5.4). The elastic constants, (C_{11}, C_{12},C_{44}), of LSHR are based on reported values in [111]. The starting point for the calibration of g(0), $\rho(0)$, k_1, for each of the fine grain and coarse grain microstructures, are based on a Kocks-Mecking approach (details included in Appendix). Additionally, the values of Γ_{act}, D, h_n, $\dot{\gamma}_0$, and n are considered to be independent of grain size, and hence constant for both microstructures. The model parameters were iteratively adjusted until a match between the experimental stress-strain curves and the crystal plasticity model was achieved (as shown in Figure *5.4*(a) and (b)). The elastic constants C_{11}, C_{12},C_{44} are temperature dependent, and hence, the values obtained at 593℃ were scaled up by 5.05% based on [102], to obtain applicable values at 427℃. The yield stress was reported to be insensitive between 427℃ and 593℃, hence the values of g(0) calibrated at 593℃ was utilized at 427℃. Lastly, the parameter h_n is also temperature dependent, however, we have assumed it to be insensitive to temperature changes between 427℃ and 593℃. The final calibrated values of the model parameters for LSHR applicable at 427℃, is

summarized in Table 5.1, which were subsequently stored in a CSV file and linked to locations A and B in the DMHT disk via the MFIN XML.

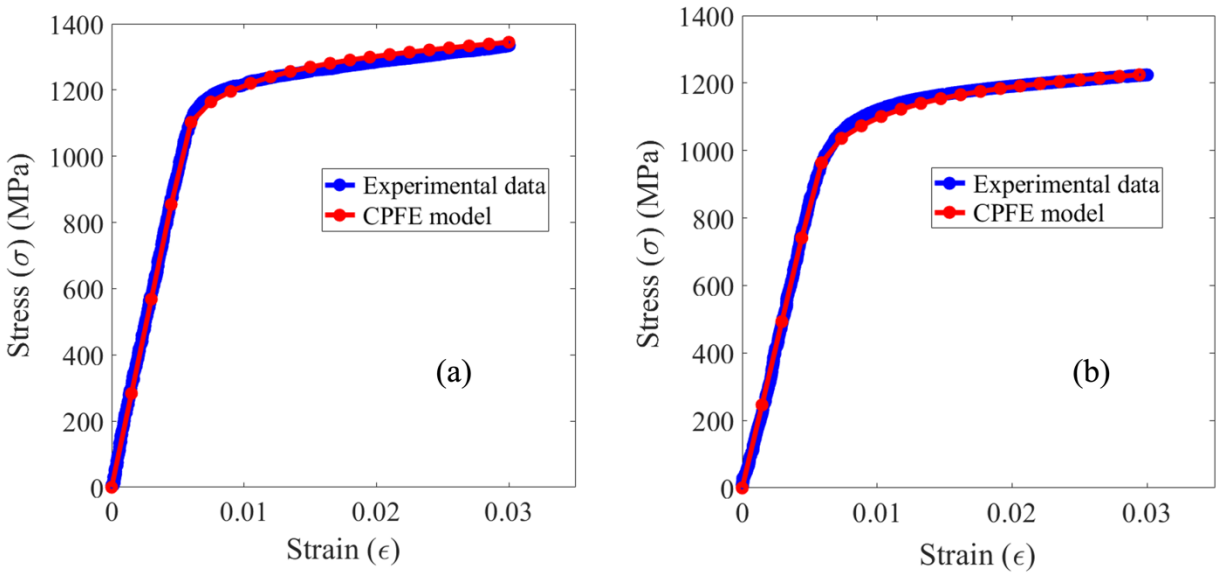

Figure 5.4. Comparison of experimental and simulated macroscopic stress–strain curves from a SEM using calibrated crystal plasticity parameters for LSHR at 593°C for (a) fine grain microstructure and (b) coarse grain microstructure.

Table 5.1. Calibrated values of CP model parameters for LSHR at 427℃ corresponding to the fine grain and coarse grain microstructures.

Parameter	Fine grain microstructure	Coarse grain microstructure
C_{11} (GPa)	257.899	228.035
C_{12} (GPa)	103.352	91.384
C_{44} (GPa)	77.273	68.233
$\dot{\gamma}_0$	0.0001	0.0001
n	40	40
$g(0)$ (MPa)	460	386
$\rho(0)$ $(1/mm^2)$	10^6	10^6
k_1 (1/mm)	$7 \text{ X } 10^5$	$4.5 \text{ X } 10^5$
h_n	0.09	0.09
Γ_{act}	$2.88 \text{ X } 10^{-3}$	$2.88 \text{ X } 10^{-3}$
D (MPa)	53280	53280

5.3.2 Fatigue life prediction model using critical value of plastic strain energy density ($W^p_{critical}$)

A single critical value of an energy-based fatigue metric is used to predict fatigue life. From historical origins [112], the work done by external forces during fatigue loading contributes to an elastic portion of energy (which is recoverable on unloading) and an internal plastic work (non-recoverable upon unloading). A portion of the internal plastic work is stored within the material, and this contributes to the formation of dislocation structures and sub-structures. Here at the meso-scale, we utilize the stored portion of the internal plastic work for predicting fatigue life relative to microstructural features, as the accumulated plastic strain energy density [49], which has been

experimentally validated, c.f. Ref. [50,113,114]. From the CPFE analysis, plastic strain energy density at a material point (x) within a SEM, is computed by accounting for contributions from individual slip systems. For the y^{th} loading cycle, the incremental plastic strain energy density ($\Delta w_y^p(x)$) is computed using Eq. (5.8).

$$\Delta w_y^p(x) = \oint \left(\sum_{k=1}^{12} \tau^k(x,t)\, \dot{\gamma}^k(x,t) \right) dt \tag{5.8}$$

The accumulated plastic strain energy density $w_y^p(x)$ over the y loading cycles is computed by summing over the accumulated cycles, $\Delta w_y^p(x)$, as shown in Eq. (5.9)

$$w_y^p(x) = \sum_{i=1}^{y} \Delta w_i^p(x) \tag{5.9}$$

A reduced number of cycles (N_s) is explicitly simulated, which is sufficient for the dislocation configurations in the material and the macroscopic hysteresis loop to stabilize and corresponds to a saturation in the values of $\Delta w_y^p(x)$. To identify a reasonable choice for N_s, a SEM corresponding to the coarse grain microstructure was simulated for 20 cycles. After the simulation was completed, $\Delta w_y^p(x)$ were extracted, followed by averaging via non-local averaging scheme described in Section 5.3.1. Finally, we extract and plot Δw_y^p values at a critical location $x = x^*$ (Figure 5.5), which corresponds to the location with the maximum value of the accumulated plastic strain energy density. The values of $\Delta w_y^p(x^*)$ saturate after a few loading cycles. A similar analysis was repeated for the fine grain microstructure as well. Based on this analysis, all the CPFE simulations in the remainder of the work were performed for 14 cycles (N_s=14 cycles) and the values of $w_{N_s}^p(x^*)$ and $\Delta w_{N_s}^p(x^*)$ were extracted and utilized for life predictions. After N_s, the increment in plastic strain energy density $\Delta w_y^p(x^*)$ is constant, with the values equal to $\Delta w_{N_s}^p(x^*)$. The extracted CPFE values associated with each SEM, are linked to the corresponding location within the DMHT disk, via the MFIN framework.

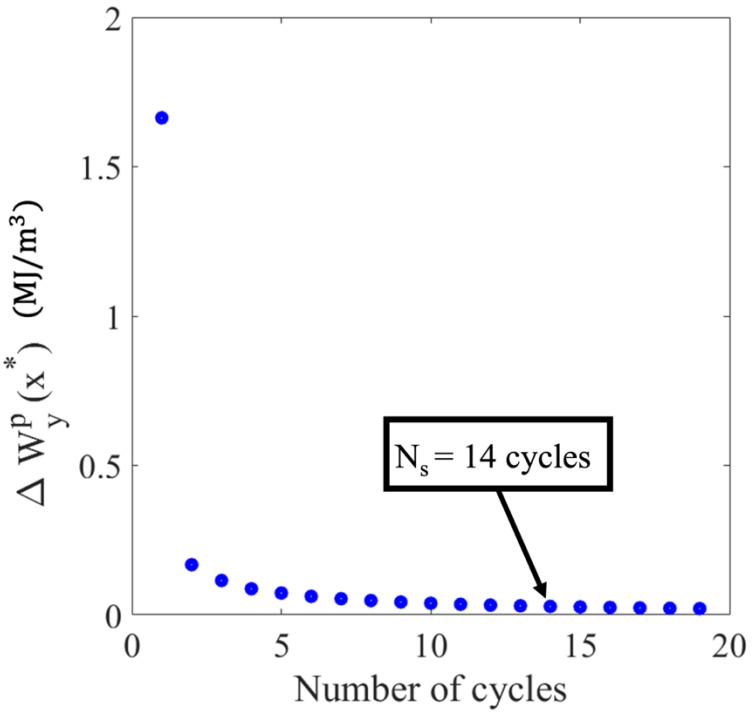

Figure 5.5. Saturation of plastic strain energy density per cycle evaluated at the critical location x* (shown for a SEM corresponding to the location with coarse grain microstructure).

The critical value of the accumulated plastic strain energy density $W^p_{critical}$ corresponding to a predicted fatigue life, N_f, is based on linear extrapolation using $\Delta w^p_{N_s}(x^*)$ from N_s to the experimentally reported fatigue life distributions (N_f^{exp}) [40] as shown in Eq. (5.10).

$$W^p_{critical} = w^p_{N_s}(x^*) + (N_f^{exp} - N_s)\Delta w^p_{N_s}(x^*) \tag{5.10}$$

The $W^p_{critical}$ value, which is postulated to be a material property, is calibrated based on a set of experimental results using a Bayesian inference approach.

5.3.3 Calibration of accumulated plastic strain energy density ($W^{p}_{critical}$) using Bayesian inference approach

There is inherent scatter associated with fatigue life, which has been attributed to variability in the microstructure features [115]. In the current framework, the statistical variability in the microstructural features is captured by creating various instantiations of virtual microstructures, SEMs. Each SEM will result in a calculated $w^{p}_{y}(x)$ evolution and an associated predicted lifetime to crack initiation, which can be compared to a series of experimental test specimen results. We calibrate a the value of $W^{p}_{critical}$ using a Bayesian inference approach (please refer [49] for full details), based on the set of SEMs simulation results compared to the distribution of the experimentally determined cycles to failure. To calibrate $W^{p}_{critical}$ for each of the coarse grain and fine grain microstructures, CPFE simulations were performed under loading conditions similar to uniaxial cyclic loading conditions (Figure 5.3(a)) utilized in the experiments reported in [40]. The experimental fatigue tests were conducted at an applied strain range $\Delta\varepsilon$=0.6 %, fatigue load ratio R=0, and at 427℃. For each of the two types of microstructures, tests were conducted on six specimens and the fatigue life data was reported in [40]. Hence, for calibrating $W^{p}_{critical}$, we utilize six fatigue life data points and 8 SEMs, per microstructure.

By rearranging Eq. (10) and replacing N_f^{exp} with predicted life $N_f^{predict}$, we can describe $N_f^{predict}$ as a function of $W^{p}_{critical}$ as shown in Eq. (11). This equation depicts the fatigue life prediction model used in this work. The values of $w^{p}_{N_s}(x^*)$ and $\Delta w^{p}_{N_s}(x^*)$ are obtained from CPFE simulations for each SEM and $W^{p}_{critical}$ is the parameter in Eq. (5.11) which is to be calibrated.

$$N_f^{predict} = \frac{W^{p}_{critical} - w^{p}_{N_s}(x^*)}{\Delta w^{p}_{N_s}(x^*)} + N_s \tag{5.11}$$

The predicted fatigue life and experimental life can be related using Eq. (5.12) [49], wherein the term δ accounts for the errors originating from experiments and the limitations in the crystal plasticity model to capture the underlying physics. The term δ can be described using a normal distribution with zero mean and a standard deviation (s) [49]. Hence, the parameter set for the Bayesian calibration process is described as $\alpha = \{W^{p}_{critical}, s\}$.

$$N_f^{exp} = N_f^{predict} + \delta \tag{5.12}$$

The inputs required for Bayesian calibration include experimental observation (i.e., the fatigue life data) and prior distributions for the model parameters α. The output of the Bayesian calibration process is the posterior distributions for α. The calibration process is separately conducted for coarse grain and fine grain microstructures. Finally, the expected values of $W_{critical}^{p}$ is extracted from the posterior distributions and utilized for fatigue life prediction.

Initially, we assume uniform prior distributions ($\pi_0(\alpha)$)**,** which is systematically updated based on a Bayesian inference method using experimental observations (D) and likelihood function $\pi(D|\alpha)$. The posterior distribution $\pi(\alpha|D)$ can be evaluated using Bayes' theorem as shown in Eq. (5.13).

$$\pi(\alpha|D) = \frac{\pi(D|\alpha)\pi_0(\alpha)}{\pi(D)} = \frac{\pi(D|\alpha)\pi_0(\alpha)}{\int \pi(D|\alpha)\pi_0(\alpha)d\alpha} \tag{5.13}$$

The likelihood term $\pi(D|\alpha)$ in the denominator of Eq. (5.13) can be expressed using Eq. (5.14). The term t is the product of number of SEMs (n_1) times the number experimental data points (n_2).

$$\pi(D|\alpha) = \frac{1}{(2\pi s^2)^{\frac{t}{2}}} \exp\left(-\frac{SSE(\alpha)}{2s^2}\right) \tag{5.14}$$

$SSE(\alpha)$ is the sum of square errors for the parameter set α, which is described using Eq. (5.15). In the present work, for both the coarse grain and fine grain microstructures, we have 8 SEMs (i.e., n_1=8) and 6 experimentally reported [40] fatigue life data points (i.e., n_2=6).

$$SSE(\alpha) = \sum_{i=1}^{n_1}\sum_{j=1}^{n_2}\left(N_i^{exp} - N_j^{predict}(\alpha)\right)^2 \tag{5.15}$$

However, while evaluating the posterior distributions of the parameter set α using Eq. (5.13), computation of the integral term in the denominator term can be challenging. To overcome this challenge, a Markov chain Monte-Carlo (MCMC) sampling approach is used. Please see [49]

for detailed description of the MCMC approach. A brief overview of the MCMC approach, pertinent to the current work, is explained in Appendix D. The posterior distributions of $W^{p}_{critical}$ was obtained using the Bayesian calibration, as shown in Figure 5.6. These results correspond to converged MCMC solutions, wherein the value of the convergence metric R_{α_r} [49] was closest to 1. The posterior distributions of $W^{p}_{critical}$ follows a normal distribution. For the fine grain microstructure (average grain size of 5.8 μm), we obtained mean value of $W^{p}_{critical}$=11,984.8 MJ/m^3 and standard deviation of $W^{p}_{critical}$ =1,264.6 MJ/m^3. Whereas, for the coarse grain microstructure (average grain size of 55 μm), we obtained the mean value of $W^{p}_{critical}$=488.6 MJ/m^3 and standard deviation of $W^{p}_{critical}$=69.4 MJ/m^3. The value of $W^{p}_{critical}$ is higher for the fine grain microstructure than the coarse grain microstructure. It has been reported [116–118] that the fatigue crack initiation life in certain materials is higher for fine grains than coarse grains, under low plastic strain amplitudes and ambient temperatures, since coarser grains are more prone to the formation of persistent slip bands (PSBs) [118,119] leading to strain localization. The metric $W^{p}_{critical}$ is postulated as a material property which is analogous to fatigue strength to crack initiation and is inherently related to the energy utilized to form stable dislocation structures and sub-structures such as PSBs. Hence, the observed trend in $W^{p}_{critical}$ with average grain size is consistent. Future work could be conducted to explore the exact relationship between $W^{p}_{critical}$ and average grain sizes.

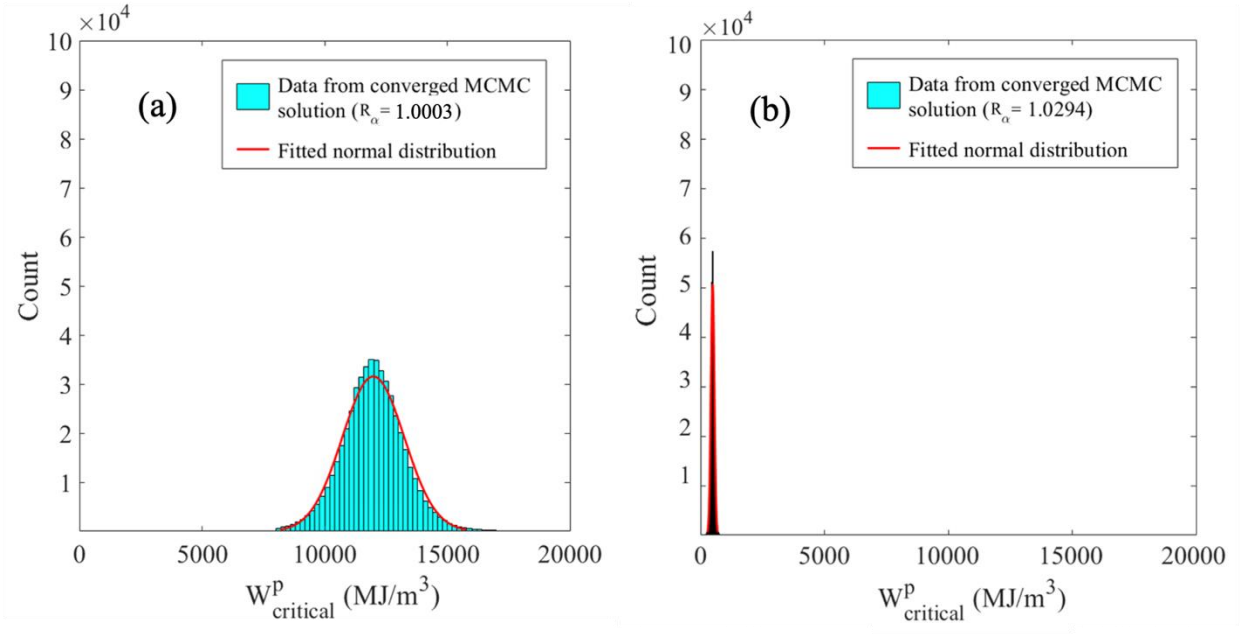

Figure 5.6. Posterior distributions of calibrated accumulated plastic strain energy density ($W^p_{critical}$) parameter for (a) fine grain microstructure and (b) coarse grain microstructure.

A probability of failure plot versus number of cycles to failure is shown for the simulations compared to the experimental results from [40], in Figure 5.7. The simulation based predicted life and experimental datasets compare well in terms of range and slope, and both follow a lognormal distribution.

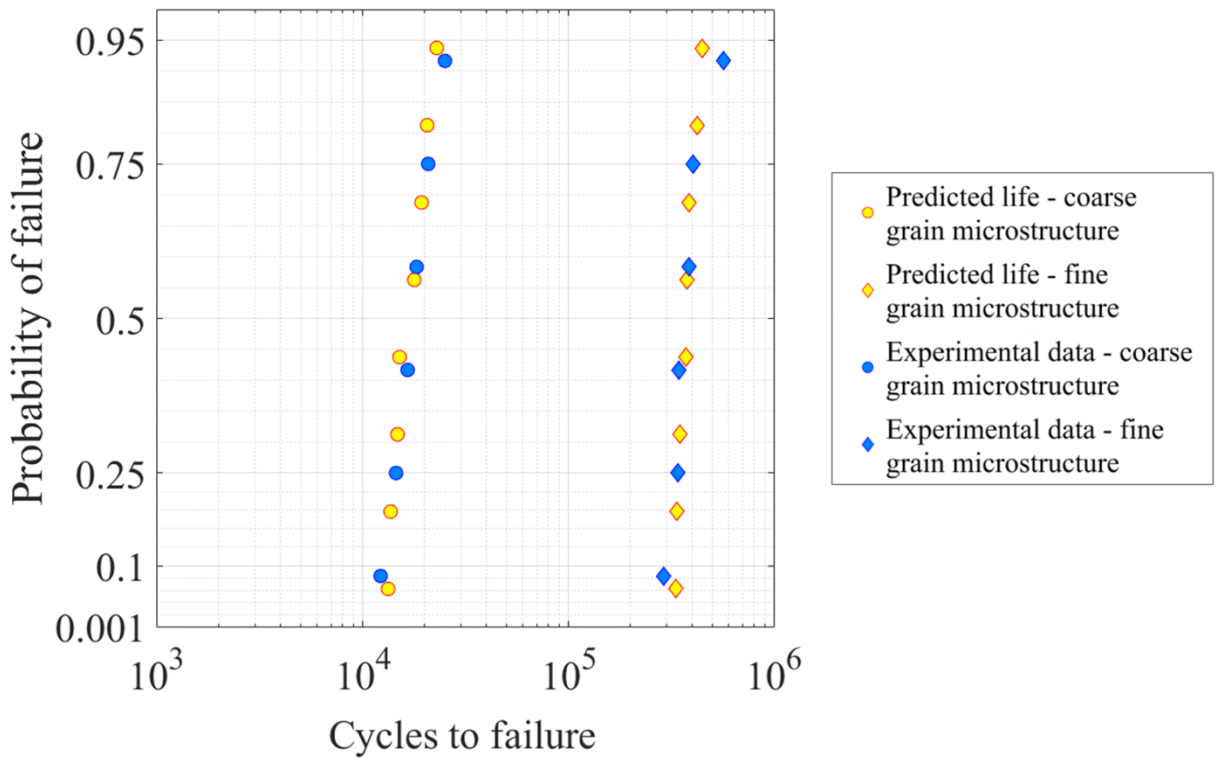

Figure 5.7. Probability of failure plot comparing experimental fatigue life data (at Δε=0.6 %, R=0, 427℃) from [40] and predicted fatigue life data (each data point corresponds to a SEM) using the calibrated values of $W^{p}_{critical}$ for fine grain and coarse grain microstructures.

5.4 Component-level FE analysis

The micromechanical fields of the DMHT turbine disk were modeled for in service conditions from rest to an overspeed at an operating temperature of 427℃. A static analysis has been performed on an axisymmetric section of the disk to acquire stresses and strains corresponding to the maximum loading condition, while assuming the minimum applied load to be zero (therefore, the fatigue stress ratio is R=0). A centrifugal load has been applied on the disk, with a spin speed of $\omega = 37500$ rpm. To enforce the constraints on the disk due to the shaft, a displacement constraint was applied on the inner surface of the disk in both the radial and axial direction. The analysis model with the mesh, applied loads, and boundary conditions are shown in Figure 5.8 (a). Linear quadrilateral elements are used with an average element size of 0.3 mm, based on a mesh sensitivity analysis.

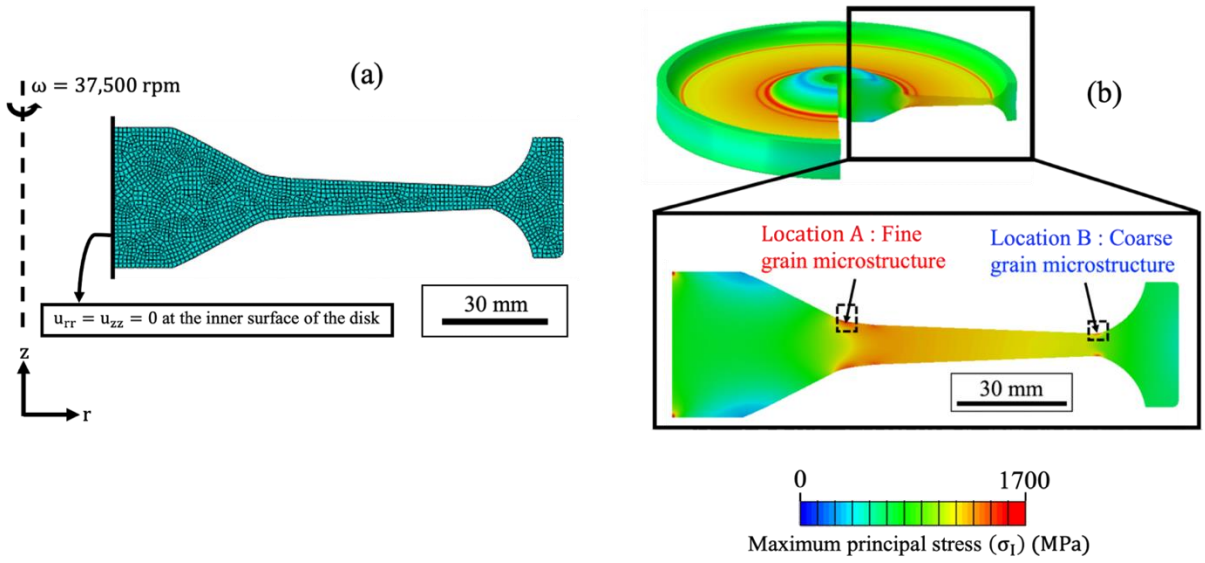

Figure 5.8. Finite element model of the disk: (a) axisymmetric model geometry with quadrilateral mesh elements, centrifugal load, and boundary conditions and (b) maximum principal stress distribution generated in the disk during service wherein the principal stresses are $\sigma_I = 1251$ MPa, $\sigma_{II} = 774$ MPa, $\sigma_{III} = 40$ MPa and principal strains are $\varepsilon_I = 0.0051$, $\varepsilon_{II} = 0.0021$, $\varepsilon_{III} = -0.0027$ at location A and $\sigma_I = 1206$ MPa, $\sigma_{II} = 939$ MPa, $\sigma_{III} = 39$ MPa, $\varepsilon_I = 0.0053$, $\varepsilon_{II} = 0.0033$, $\varepsilon_{III} = -0.003$ at location B.

An elastoplastic material model was used for the FE analysis following a Johnson-Cook [120] type hardening rule (Eq. (5.16)), wherein the flow stress ($\bar{\sigma}$) is a function of the equivalent plastic strain ($\bar{\varepsilon}$) and applied temperature (T). In Eq. (5.16), the parameters σ_{YS}, B, c_1, c_2, T_{ref} , T_{melt} refer to the yield stress, strain hardening coefficient, strain hardening exponent, temperature exponent, reference temperature and melting temperature, respectively.

$$\bar{\sigma} = (\sigma_{YS} + B\bar{\varepsilon}^{c_1})\left[1 - \left(\frac{T - T_{ref}}{T_{melt} - T_{ref}}\right)^{c_2}\right] \tag{5.16}$$

Additionally, we also utilize elastic model parameters, Young's modulus (E) and Poisson's ratio (ν) , as well as physical properties, mass density (ρ) [102]. The material properties assigned to different regions (bore region, transition region, and rim region) of the disk are based on the original average grain size definitions within the MFIN XML (Figure 5.2 (a)). For each element in the component FE model, the average grain size is extracted from the nearest point feature (as shown previously in Chapter 4). The material properties of LSHR were individually calibrated for

the bore region (fine grain microstructure) and the rim region (coarse grain microstructure) based on reference stress-strain data at 593℃ (Figure 5.4). The material property of LSHR corresponding to different regions of the disk are summarized in Table 5.2.

Using the calibrated Johnson-Cook plasticity parameters (B and c_1) and Young's modulus (E) for bore and rim region, the corresponding parameters for the transition region were determined through interpolation, based on the average grain size value of 38 μm. The physical, elastic, and plastic parameter values are stored in individual CSV files and linked to distinct regions of the DMHT disk, using the earlier created point features within the MFIN XML. Subsequently, the temperature dependent terms in Eq. (5.16) were used to conduct the FE analysis for the application temperature of 427℃.

Table 5.2. Material property values of LSHR at 427℃ which were utilized for the FE analysis, corresponding to the three regions (as shown in Figure 5.2 (a)) of the DMHT disk.

Material Properties	Bore region (Average grain size = 5.8 μm)	Transition region (Average grain size = 38 μm)	Rim region (Average grain size = 55 μm)
Density (ρ) (kg/m^3)	8359	8359	8359
Young's Modulus (E) (GPa)	199.595	181.736	176.484
Poisson's ratio (ν)	0.286	0.286	0.286
Yield stress (σ_{YS}) (MPa)	1209	1112	1101
Strain hardening coefficient (B)(MPa)	3641	3078	2697
Strain hardening exponent (c_1)	0.81	0.76	0.73
Temperature exponent (c_2)	1	1	1
Melting temperature (T_{melt})(℃)	1297	1297	1297

The principal stresses and strains across the component were calculated via the FE analysis and exported within a CSV file along with the corresponding element centroid location coordinates.

Thereby, point features are created within the MFIN XML of the DMHT disk, and the FE analysis results are linked to individual locations (Section 4.2). The maximum principal (σ_I) stress distribution across the disk is shown in Figure 5.8 (b). As expected, we observe high stresses in the region of the two locations of interest (i.e., the Locations A and B), due to the steep variation in cross section of the disk at these locations. Additionally, the discrete change in material properties associated to the three distinct regions of varying average grain sizes occurs at locations sufficiently far from the Locations A and B. The principal strains from Locations A and B are used to inform multiaxial displacement boundary conditions for the CPFE analysis, in a hierarchical fashion via the MFIN framework. The CPFE analysis tied to locations A and B are subsequently utilized for location-specific fatigue life predictions in the DMHT disk.

5.5 Results and discussion

The framework is used to systematically identify, store, and retrieve site specific material microstructure and associated properties across a component. The data is seamlessly exchanged to generate (i) CPFE simulations to identify material allowables through uniaxial loading conditions, (ii) component level FE analysis, and (iii) hierarchical CPFE simulations with site specific boundary and loading conditions from the component analysis.

5.5.1 Simulation based uniaxial minimum fatigue life for LSHR

For establishing the materials allowables by identifying the minimum fatigue life, this framework is beneficial to (i) complement experimental results with simulated predictions, thereby accounting for additional cases of extreme value statistics of microstructural features to identify the minimum life (as described in this section) and (ii) connect to component lifing analysis (Section 5.5.2). Here, we present the predicted fatigue life results obtained via CPFE simulations, while applying a constant uniaxial loading condition ($\Delta\varepsilon$=0.6 %, R=0, 427℃) for all the SEMs (akin to fatigue testing using virtual specimens). The probability of failure versus loading cycles plot is shown in Figure 5.9. In this plot, we have data points corresponding to the fine and coarse grain microstructures, representing the predicted fatigue life obtained from their respective SEMs. In addition, the lognormal fits of these datasets are included. The plot in Figure 5.9 provides: (i) the predicted life corresponding to the fine grain microstructure, (ii) the predicted life

corresponding to the coarse grain microstructure, and (iii) the predicted life for the combined dataset as a single distribution (i.e., similar to the traditional approach of assuming uniform microstructure across the component).

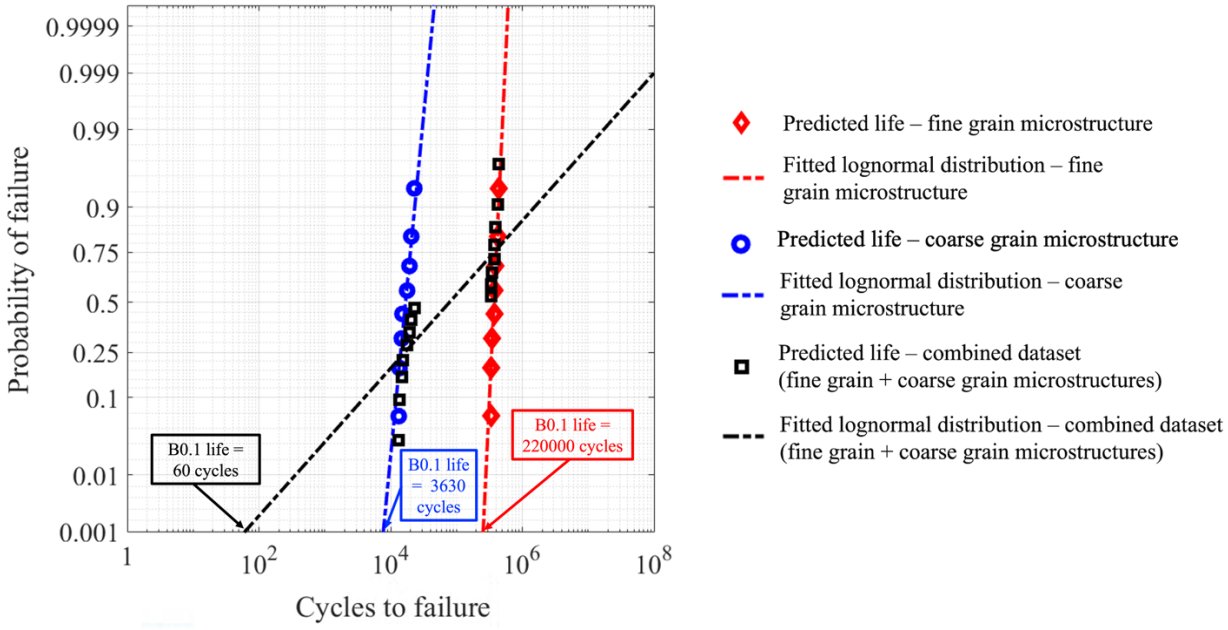

Figure 5.9. Probability of failure plot versus cycles to failure with B0.1 life values obtained by treating the datasets as individual samples per location based on the underlying microstructure (blue data points correspond to SEMs from coarse grain microstructure and red data points correspond to fine grain microstructure) compared to treating the entire dataset as one single sample (independent of the microstructure).

The significance of the presented result is two-fold. Firstly, the use of microstructure-sensitive life predictions presents opportunities to reduce the overall number of tests needed to identify the allowable material life. Secondly, we observe reduced uncertainties in the reported fatigue life by treating datasets corresponding to individual locations as separate distributions, which was enabled by the tracking capabilities of location-specific microstructures in the MFIN framework. For identifying the minimum allowable life of the material using the B0.1 approach, we utilized the lognormal fits and extrapolated the value corresponding to the probability of failure of 1/1000 for each of the three cases shown in Figure 5.9. The B0.1 life corresponding to the

coarse grain microstructure was estimated as 3,630 cycles, whereas the B0.1 life corresponding to the fine grain microstructure was estimated as 220,000 cycles. On the other hand, while using the traditional approach of treating all the fatigue life datasets from a single loading condition as one single distribution (assuming a monolithic component), we obtain a significantly lower minimum allowable B0.1 life of 60 cycles. Hence, by accounting for precise microstructure descriptions of the material (i.e. location-specific microstructures), while estimating the minimum allowable life of the material, we could potentially reduce uncertainties and shift our estimates to a higher minimum life. The analysis demonstrated in this work could be particularly beneficial while estimating the material allowable(s) for next-generation components with gradient microstructures.

5.5.2 Component level: Location-specific fatigue life predictions for the DMHT disk

Next, we describe the location-specific fatigue life predictions connected to the component (i.e., component lifing) by using pertinent location-specific loading conditions within CPFE simulations in a hierarchical fashion. As explained in Section 5.4, each of the SEMs, corresponding to Location A (fine grain microstructure) were simulated with multiaxial displacement boundary conditions, identified through the component scale FE analysis (Section 5.4) by using the principal strains, $\varepsilon_I = 0.0051$, $\varepsilon_{II} = 0.0021$, $\varepsilon_{III} = -0.0027$ and R = 0. Similarly, the SEMs corresponding to Location B (coarse grain microstructure) were simulated with $\varepsilon_I = 0.0053$, $\varepsilon_{II} = 0.0033$, $\varepsilon_{III} = -0.003$ and R = 0, based on the component FE results. The MFIN framework was utilized to track and retrieve the principal strains across the component from in-service type loading conditions at locations of interest, determined via component level FE analysis, and utilized to hierarchically inform the multiaxial displacement boundary conditions for the CPFE analysis (Figure 5.8 (b)).

The probability of failure versus loading cycles plot corresponding to Locations A (near bore) and B (near rim) in the component is shown in Figure 5.10. Each data point in the plot corresponds to the predicted life from a SEM simulation. The predicted life for each multiaxial SEM was computed using Eq. (5.11), wherein the corresponding $w^p_{N_s}(x^*)$ and $\Delta w^p_{N_s}(x^*)$ values were obtained from the CPFE analysis. Since $W^p_{critical}$ was shown to be applicable independent of loading conditions [49], we utilized the earlier calibrated $W^p_{critical}$ values, i.e. $W^p_{critical} = 11984.8\ MJ/m^3$ for SEMs corresponding to the fine grain microstructure (Location A) and

$W^{p}_{critical} = 488.6\ MJ/m^3$ for SEMs corresponding to the coarse grain microstructure (Location B) in Eq. (11). In Figure 5.10, to represent the uncertainties associated in our fatigue life predictions, we have included a prediction range corresponding to 95% confidence level. For calculating this prediction range, we incorporated two sources of variability [50], which include (i) the standard deviation of $W^{p}_{critical}$ from the posterior distribution obtained via the Bayesian calibration process (Section 5.3.3) and (ii) uncertainties associated with calibration of the CP model parameters propagating to the $w^{p}_{N_s}(x^*)$ values, as described in [121].

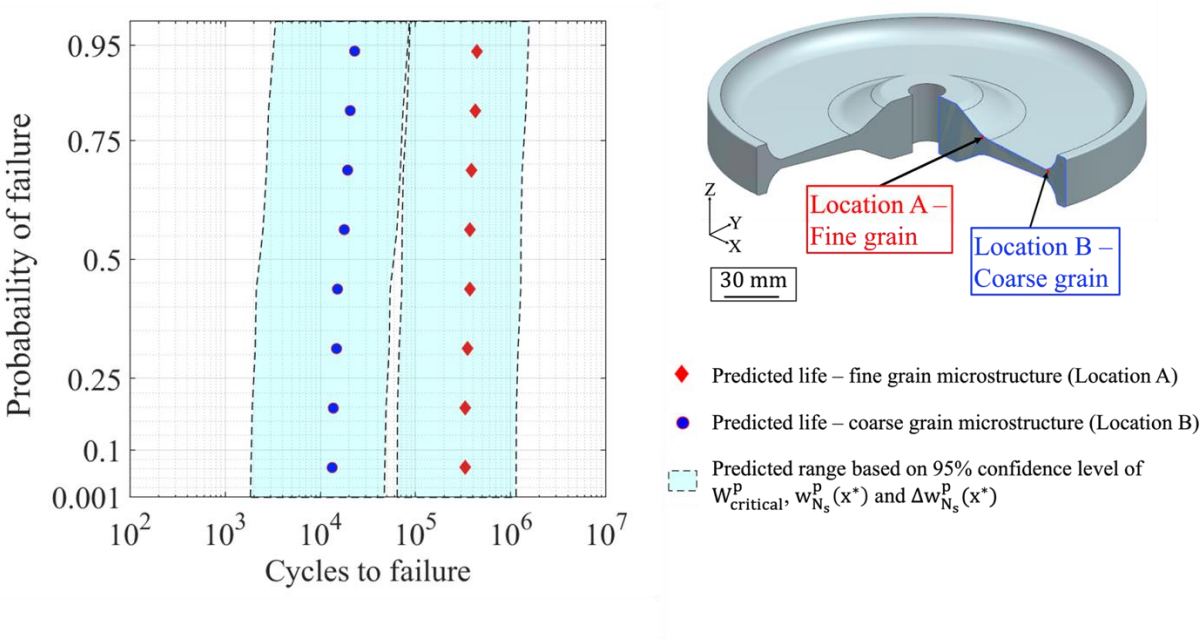

Figure 5.10. Probability of failure plot corresponding to location A (fine grain microstructure) and location B (coarse grain microstructure) obtained via crystal plasticity simulations (each data point in the plot corresponds to a SEM).

By identifying and tracking site-specific microstructures in the DMHT disk and conducting associated CPFE analysis via the MFIN framework, we were able to isolate fatigue life predictions connected to individual locations in the component, as shown in Figure 5.10. The result shown in Figure 5.10 is indicative of critical locations in the component from the context of fatigue crack initiation, thereby providing insights to the designer on when and where a crack initiates first, given the location-specific microstructural information and loading conditions. In the current demonstration, wherein we have conducted analysis at two distinct locations, it is evident that

Location B (in the rim region) is prone to crack initiation at an earlier cycle count. From the context of planning the maintenance and inspection schedules during the service of the disk, the site-specific likelihood of failure is useful information. Additionally, the predictive analysis approach presents opportunities to determine lifecycles, after which inspection and maintenance of a serialized component should be scheduled [122]. We would like to emphasize that the modeling framework used in this work focuses on fatigue life predictions for crack initiation. However, depending on the local microstructure and local geometric constraints at the site of crack initiation within the component, the crack growth rates will vary. In the near-threshold regime, coarse grain microstructures are typically more tolerant to crack growth as opposed to fine grain microstructures [123]. However, the presented MFIN framework and its location-specific tracking capabilities of local microstructure and loading states can be extended for evaluating the location-specific fatigue life via a damage tolerance analyses, including the incorporation of residual stress information (Section 3.4 and Section 4.3).

5.5.3 Considerations for the microstructure-sensitive location specific life predictions

The transition towards a physics-based, microstructure-sensitive approach for lifing components, as demonstrated via the DMHT study, presents numerous advantages. By including more physics-based predictive analysis via simulating multiple SEMs, we can improve our understanding of the cause-effect relationships in the material system. We can also reduce the number of experiments needed for determining the minimum fatigue life, thereby reducing the overall costs incurred in the material qualification process. For component lifing, we presented a hierarchical approach to utilize the stress/strain states from the component-level FE analysis within the microstructure-sensitive CPFE analysis. The approach is computationally tractable since it does not rely on modeling the entire component's microstructure. Based on the component geometry, applied loading conditions, as well as legacy records from the lifecycle of prior versions of the component, lifing engineers can determine critical locations to perform lower length scale CPFE simulations. Moreover, the approach does not rely on homogenization; hence we can directly incorporate microstructural variability at each component location of interest by simulating multiple SEMs and therefore account for extreme values of microstructural attributes while predicting fatigue life. The CPFE analysis used in this work utilized individual sets of model parameters corresponding to distinct microstructures. Further work can include strain gradient

CPFE approaches [124], which can explicitly capture grain size effects via a single set of crystal plasticity model parameters applicable to multiple locations in the component. Lastly, this modeling framework can be extended to include finer discretization in the microstructure attributes across the spatial regions or include more rich microstructural information, including precipitate distribution, the likelihood of porosity/inclusions, residuals stresses, or surface effects.

The capability of the MFIN framework has been presented for storing, tracking, and updating material microstructural information tied to individual locations in the component. The use of the data linking approach within the MFIN framework allows dynamically updating the material state of the component and its individual locations. Hence, the MFIN framework presents opportunities to continually update material microstructural description from characterizations conducted at different stages of the product lifecycle, such as during the individual stages of manufacturing, acceptance of material from various vendors, and during periodic inspections of the component accounting for time-dependent degradation or damage. By enabling the dynamic updating of data and seamless data exchange, the MFIN framework provides the use of precise microstructural descriptions within the subsequent microstructure-sensitive predictive analysis of a component, thereby further reducing uncertainties in the input microstructures and associated predicted life distributions. Hence, the MFIN framework presents opportunities to create the digital twin of a serialized component to assist in decision-making during the product lifecycle.

The use of the MFIN framework for fatigue life assessment of components via physics-based simulations provides new opportunities to design the component and tailor the microstructure simultaneously, thus aiding in understanding the fatigue tradeoffs upfront during the product design stage. The framework can be extended by developing new MFIN schemas and wrapper code(s) to link to process modeling-related code(s) for predicting residual stress distributions, precipitates, grain sizes, texture evolution as well as property code(s) to compute strength by using structure-property linkages. By assessing current design strategies and understanding location-specific minimum life, engineers can potentially utilize a fully model-based approach to iteratively redesign by modifying the geometry and/or the processing route to alter site-specific microstructures to optimize location-specific performance.

6. CREATING CONNECTIVITY BETWEEN GEOMETRIC INSPECTION AND STRUCTURAL ANALYSIS VIA MFIN FRAMEWORK FOR ASSESSING AS-BUILT AND AS-USED COMPONENTS

The contents of this chapter have been submitted for publication in Gopalakrishnan S, Hartman NW, Sangid MD. A digital engineering framework to facilitate automated data exchange between geometric inspection and structural analysis. Submitted, under review (2022).

In Chapters 4 and 5, we presented the use of the MFIN framework with the primary focus of tracking and using material information applicable to a component. However, during structural integrity analysis of components, we rely on estimating stress distributions within a component during service, and the use of the precise geometric description of the component (i.e., its current geometry) for such analyses is crucial. In this chapter, we utilize the MFIN framework to create a workflow for automated data exchange between geometric inspection and structural analysis tools. In Chapter 4, we presented an integration between the MFIN and structural analysis tools, to programmatically feed component geometry and materials information for the analysis. In this chapter, we expand the MFIN framework to utilize coordinate measurement data and update geometric features within the nominal CAD model of a component, thereby creating CAD models of manufactured components or after-use components. In Section 6.1, we present the data integration methods via MFIN used for developing this workflow. In Section 6.2, we present a use case to capture deviations in the surfaces of a turbofan component from a maintenance, repair, and overhaul (MRO) standpoint. In Section 6.3, we discuss the scope of this automated workflow to support engineering decision making for MRO and materials review board (MRB)

6.1 Data integration methodology and framework

For this work, we use the earlier developed integration between MFIN and structural analysis tools for supplying model geometry and material properties (Chapter 4). Additionally, in this section, we present the application of the framework for linking and retrieval of the coordinate measurement results applicable to geometric features (specifically surfaces), and the process of programmatically using this data within external surface fitting code(s) in Section 6.1.1. Next, we present a programmatic process (in Section 6.1.2) to update the surfaces within the nominal CAD

model with the fitted surfaces from measured data, thereby creating CAD models of manufactured components and capturing any geometric deviations to the surfaces.

To capture the deviations in the surfaces, we develop and use a programmatic workflow (Figure 6.1) to link and retrieve coordinate measurement datasets pertaining to individual surfaces in the component, thereby utilizing the measurement datasets to fit surfaces and update the nominal CAD model. Additionally, a summary of all the essential MFIN data elements, schemas and API functions used in the workflow is shown in Table 6.1.

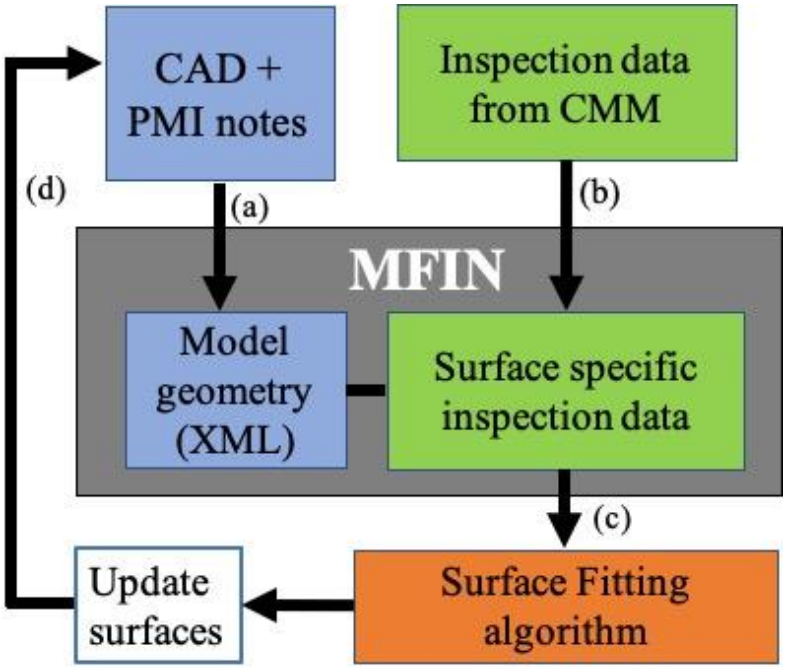

Figure 6.1 Process of creating CAD models of as-manufactured/in-service components by utilizing coordinate measurement data via the MFIN framework, wherein (a) the nominal CAD model (design model) along with the product manufacturing information (PMI) notes are translated into a derivative file format (MFIN XML), (b) measurement data procured from a coordinate measurement machine (CMM) is integrated with the corresponding scanned surfaces within the MFIN XML, (c) a surface fitting algorithm (external code) is applied to fit freeform surfaces onto the measurement data, and (d) the surfaces in the nominal CAD model are programmatically updated.

Table 6.1. Summary of essential data elements, schemas and API functions utilized within the workflow presented in Figure 6.1.

Name of the data elements/schemas/API functions	Purpose/Description	Connectivity to the workflow in Figure 6.1.
"*QIFDocument*"	The top-level data element of MFIN XML, which contains all the other data elements as its sub-elements.	Created in 6.1(a).
"*QIFDocument.xsd*"	Schema file defining the structure of "*QIFDocument"* element.	Used in 6.1(a).
"QIFDocument.py"	A Python class with API functions to facilitate programmatic linking and retrieval of data using MFIN XML.	Used throughout the workflow.
"QPId"	Data element to record universally unique identifier (UUID) assigned to each MFIN XML file.	Created in 6.1(a). Used throughout the workflow.
"*localId*"	Local identifiers of individual data elements within the MFIN XML for tracking and retrieval purposes.	Created in 6.1(a). Used in 6.1(b), 6.1(c).
"*QIFResults.xsd*"	Schema file defining data elements specific to inspection and measurements.	Used in 6.1(b) and 6.1(c).
"*MeasurementResultSet*"	Data element capturing information related to all measurement events in a product.	Created in 6.1(b) and used in 6.1(c).
"*MeasurementResult*"	Data element containing information related to a specific measurement event.	Created in 6.1(b) and used in 6.1(c).
"*featureId*"	Data element used for tracking measured geometric features within a MFIN XML instance and takes the value of a feature's *"localId".*	Created in 6.1(b) and used in 6.1(c).
"*ExternalFileReferences*"	Data element capturing the file paths of the measurement result datasets.	Created in 6.1(b) and used in 6.1(c).
"*MFINAnalysis.xsd*"	Schema file defining data elements to capture file linkages to analysis model geometry, input and output files.	Used at the end of the workflow.
"*MeasuredFeature*"	PMI note tag for tracking the measured features within the CAD model.	Created in 6.1(a) and used in 6.1(b), 6.1(c) and 6.1(d).
"*CreateBsurfThruPts*"	NX API function to generate NURBS surfaces in CAD tool by using the control point coordinates.	Used in 6.1(d).

6.1.1 Integration of coordinate measurement data with geometric features

For capturing coordinate measurement results applicable to geometric features within a product, the MFIN XML already consists of an element inherited from the QIF standard, namely the "*QIFResults.xsd*" [125]. However, the existing schema facilitates only storing the results directly within the MFIN XML, which has two associated challenges - (i) we could potentially end up with large sized files (especially for components with many features or with multiple instances of measurement results procured for individual features) and (ii) limits dynamic access to the most recent version and historically recorded measurement data. In this work, the MFIN schemas were modified to create linkages between a geometric entity in the model and externally stored CMM datasets. Hence, the "*QIFResults.xsd*" schema was modified to group file paths of externally stored measurement datasets with geometric features (using its corresponding "*localId*"). The updated "*QIFResults"* schema generates the following structure of data elements – "*MeasurementResultSet"* at the top level to group all the measurement result datasets applicable to the product and each measurement result recorded as sub-elements with the element name "*MeasurementResults*". Following the overall structure of the MFIN XML (Section 4.1), each "*MeasurementResults"* element consists of its own corresponding "*localId"* to track and retrieve the measurement result information from a specific measurement event. The "*MeasurementResults"* element comprises of two primary sub-elements namely, the "*featureId*" (which takes the value of a feature's "*localId"* and informs the geometric feature to which the measurement results were linked) and the "*ExternalFileReference*" (which records the file paths to the measurement results). Additionally, there are other sub-elements to capture metadata such as the file description, file type information, user who logs the measurement results, and measurement device identifier which was used for procuring the data.

A programmatic process has been developed for linking measurement datasets with relevant surfaces by utilizing the PMI notes. A pre-requisite step in the current process is to create PMI notes in the native CAD model with tags "*MeasuredFeature1*", "*MeasuredFeature2*", ... , "*MeasuredFeatureX*" corresponding to each geometric feature of interest, prior to generating an MFIN XML instance (Figure 6.1(a)). The programmatic process (Figure 6.1(b)) to create measurement result linkages follows: (a) reading the PMI note with the "*MeasuredFeature*" tag and recognizing the surface wherein the measurement dataset is linked (using its "*localId"* in the MFIN XML), (b) selecting CMM result files (could be one or multiple files) and (c) creating data

linkages in the "*MeasurementResult*" element within the MFIN XML. After iteratively linking the measurement results to each of the surfaces containing the "*MeasuredFeature*" tag, the datasets are available for downstream retrieval and usage via the MFIN XML.

6.1.2 Process of applying surface fitting and updating the CAD Model

For the retrieval of measurement datasets corresponding to specific surfaces and their use within an external surface fitting code, a programmatic method (Figure 6.1(c)) has been created and used. A wrapper code has been developed to search for the PMI note with the tag "*MeasuredFeature*" and identifying the surface (using the "*featureId"*) to which the note applies. Within the "*MeasurementResultSets*" element in the MFIN XML, the CMM dataset files linked to the surface is searched (for a specific "*featureId"*) and finally the data within the files are retrieved within the external surface fitting code (which was a MATLAB script in this present work). The process is iteratively repeated for each surface linked with measurement data.

After the surface fitting code is executed, in order to update the surfaces in the nominal CAD model with the fitted surface definitions, a wrapper code has been developed using the APIs provided with the CAD tool (we used Siemens NX APIs for the current work). For speeding up the process of creating a wrapper code, the macro code generation capability was utilized, which is prevalent in commercial CAD software(s). This involves, manually performing the CAD operations such as surface deletion and creating new surfaces for a single time, thereby enabling the creation of a wrapper code to repeat similar operations. The output from the surface fitting algorithm is utilized as inputs within the wrapper code, for updating the surfaces in the CAD model (Figure 6.1(d)). The PMI notes are used for tracking the surface, which is to be updated. The existing surfaces in the nominal CAD model with the PMI note are deleted, followed by creating new surfaces representative of the physical surface in the product. Finally, a new MFIN XML instance is generated using the updated CAD model and linked as a sub-element (using its UUID and MFIN XML file path) within the original MFIN XML corresponding to the nominal model. Hence, the geometric definitions within the updated CAD model informed by coordinate measurement data is readily available for structural analysis via the MFIN XML, which is illustrated with a use case in this work.

6.2 Use case: Analysis of a turbofan blade with foreign object damages during service

In this section, we demonstrate the developed process (presented in Section 6.1) to capture deviations in the surfaces of a component for a maintenance, repair, and overhaul (MRO) use case, however the methodology can be generally applied more broadly during the lifecycle, including materials review board decisions of a manufactured part.

During service, jet engine components such as the turbofan can be prone to possible collisions from foreign objects (Figure 6.2(a)), inducing damage to individual components and sub-assemblies. The blades in these turbofan assemblies incur geometric deviations (Figure 6.2 (b)), thereby necessitating the decision on their further usage – either use as-is, repair and re-use, or retire. Hence, in this study, we have undertaken a use case for the analyses of a turbofan assembly made of a titanium alloy, namely Ti-6Al-4V, subjected to foreign object damage of a single blade. We demonstrate the process of creating a CAD model of the turbofan assembly with its damaged blade, replicating the after-use state, by utilizing coordinate measurement scans and subsequently applying a NURBS-based surface fitting algorithm, via the MFIN framework. Further, we illustrate conducting structural analysis by utilizing the after-use geometric model and present the variations in the local stress fields in the region of damage compared to a case of using the nominal design geometry (or as-designed), which is the more conventional approach.

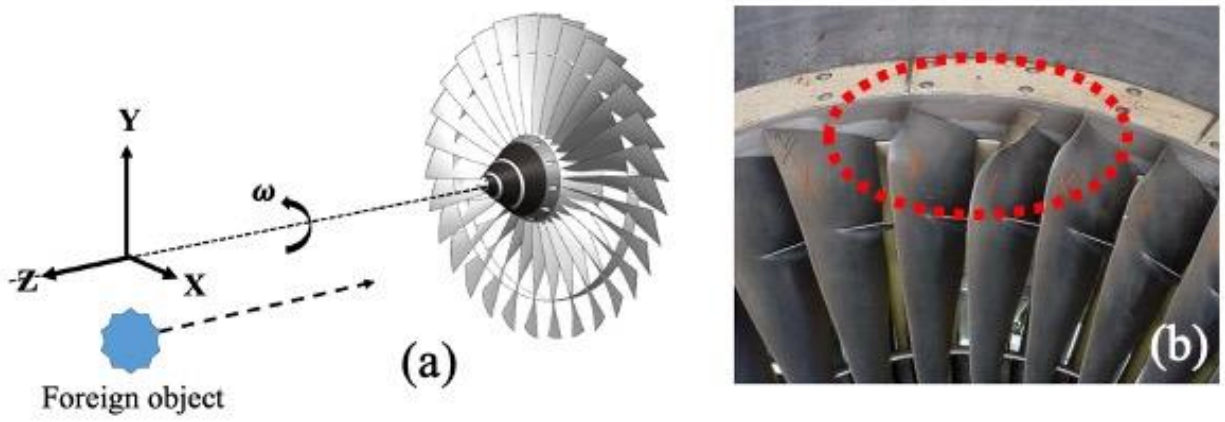

Figure 6.2. Foreign object damage induced in aircraft engine components during service: (a) a schematic of turbofan blades being exposed to a foreign object and (b) an example of damaged blades [126] with modified surface geometries.

6.2.1 CAD model of nominal turbofan assembly

First, we created a nominal CAD model for a turbofan assembly with 30 blades, with geometric dimensions from Ref. [127]. The turbofan assembly consists of the hub section and the blades(s) (Figure 6.3 (a)) (we have ignored the nose section of the turbofan in this use case for simplicity). Since the turbofan assembly is axisymmetric about the Z axis, a sector of the hub with an angle of 12° along with a single blade geometry was created (shown in Figure 6.3 (b)) and revolved about the Z-axis to create the entire turbofan assembly (Figure 6.3 (a) and Figure 6.3 (c)). The blade geometry comprises of four surfaces, which are referred to as the front surface, the back surface, and the two lateral surfaces in this chapter. For facilitating linking and retrieval of measurement data to the front and the back surfaces of the blade (Figure 6.3 (c)), PMI notes have been attached following the process presented in Section 6.1. Finally, the nominal CAD model of the turbofan assembly and the PMI notes associated to its surfaces are translated into the derivative MFIN XML file format.

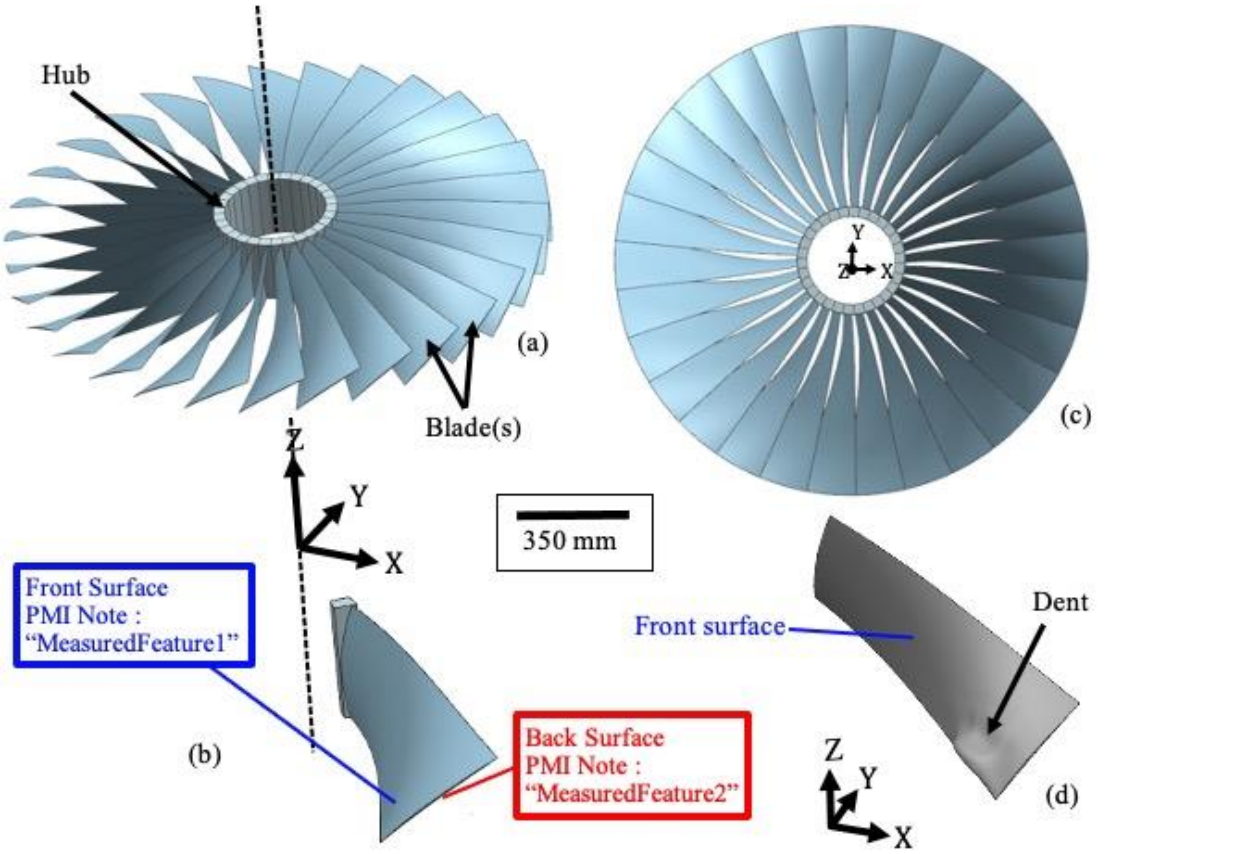

Figure 6.3. Geometry of the turbofan assembly considered for the use case: (a) CAD model of the nominal geometry, (b) 1/30th axisymmetric sector and PMI notes associated to the blade's surfaces, (c) top view of the nominal CAD model, and (d) a synthetically generated modification to the surface profile of the blade - representing a foreign object damage.

6.2.2 Foreign object damage – CMM data acquisition

To provide a general case of a damaged blade, we created synthetic datasets emulating CMM measurements from a blade with a dent. Firstly, we created coordinate measurements of the nominal blade using the CAD tool, by overlaying datum points on its surfaces. Datasets with 20-line scans corresponding to 20-curve sections were created for both the front and the back surfaces (similar to the example shown in Figure 6.4(a)). Along each line scan, we generated 400 pseudo coordinate measurement data points. A choice of 400 scanned points along each curve section would imply a scanned point for every 0.8 to 0.95 mm distance which is feasible to probe and measure using both contact and non-contact based CMMs. The position coordinates of points were manually modified to replicate a dent in the front surface similar to Figure 6.3(d). For each section curve, the scanned coordinate measurement datasets were stored in distinct files with a comma-

space value (CSV) file format. The CSV files were programmatically linked with the applicable surfaces (by utilizing the PMI notes) within the MFIN XML, by following the process presented in Section 6.1.1.

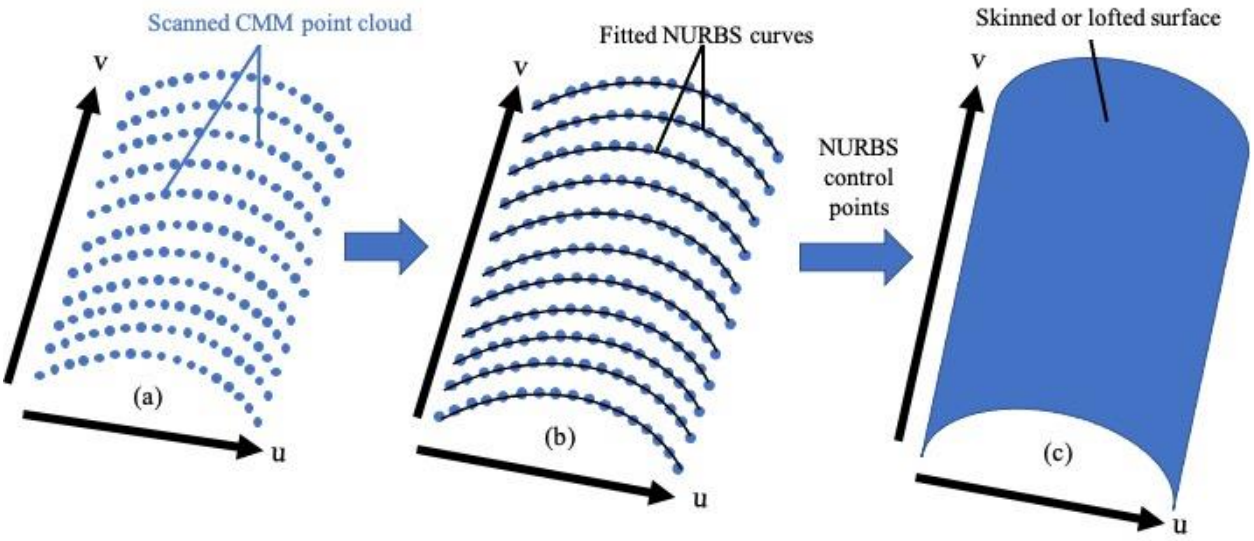

Figure 6.4. Schematic of the surface fitting procedure wherein (a) the CMM point cloud on a surface (shown in the parametric space (u-v)) is (b) fit with non-uniform rational B-spline (NURBS) curves (along u) and (c) a surface is generated by skinning or lofting across the curve sections (along v).

6.2.3 Surface fitting approach using NURBS

To create the surface geometries of a damaged blade using the coordinate measurement dataset, we apply a classical two-step surface fitting approach: (i) fitting NURBS curves to generate section curves of the blade, followed by (ii) skinning or lofting [128] across the section curves. The use of NURBS curves leverages local control on the shape of individual section curves, particularly useful for surfaces with complex curvatures such as in the case of a blade. The surface fitting code has been developed in MATLAB for the current use case. The set of 20 measurement datasets (CSV files) applicable to both the front and the back surfaces are programmatically fed into the MATLAB code (as described in Section 6.1.2), one surface at a time to conduct the surface fitting operation.

In step (i), our goal is to fit NURBS curves $C_r(u)$ to each line scan of CMM points along the u-direction as shown in Figure 6.4 (b). In our case we have 20-line scans per surface and hence

r ranges from 1 to 20. Firstly, we parameterize the scanned data points $Q_t = \{\overline{x_t}, \overline{y_t}, \overline{z_t}\}_{t=1,2,..,m}$ in the *u*-direction (Figure 6.4) for each curve section, by using centripetal parameterization scheme [129] as shown in Eq. (6.1). The use of centripetal parameterization is conventionally preferred for surfaces wherein the measured points could be non-uniformly spaced such as in a blade surface with complex curvatures, and therefore chosen for the current demonstration. Hence, for each of the line scans, coordinate measurement points range between 0 and 1 after parameterization.

$$u_1 = 0$$
$$u_t = u_{t-1} + \frac{\|Q_t - Q_{t-1}\|}{\sum_{j=1}^{m-1}\|Q_{j+1} - Q_j\|}, \quad 2 \le t \le m \tag{6.1}$$

A standard NURBS curve [130] made of piecewise polynomials of order *k* is defined as shown in Eq. (6.2). $C(u)$ represents the coordinates of the points on the NURBS curve, v_i represents the coordinates of the control points which control the shape of the piecewise polynomials forming the NURBS curve and w_i represents the scalar weights corresponding to each control point for providing additional local control on its shape.

$$C(u) = \frac{\sum_{i=1}^{n} w_i v_i B_{i,k}(u)}{\sum_{i=1}^{n} w_i B_{i,k}(u)} \tag{6.2}$$

The B-spline basis function ($B_{i,k}(u)$) for the *i*-th control point is defined as shown in Eq. (6.3), following De-Boor's recursive formula [130], which is a function of the parameter value (*u*) and the knot vector (*U).*

$$B_{i,k}(u) = \frac{(u - U_i)B_{i,k-1}(u)}{U_{i+k-1} - U_i} + \frac{(U_{i+k} - u)B_{i+1,k-1}(u)}{U_{i+k} - U_{i\_+1}}$$
$$B_{i,1}(u) = \begin{cases} 1, if\ U_i \le u \le U_{i+1} \\ 0, otherwise \end{cases} \tag{6.3}$$

The knot vector (*U*) comprises of parameter values, where the piecewise polynomials forming the NURBS curve join and are dependent on the choice of number of control points (*n*)

and degree of the piecewise polynomial (p). U can be computed using Eq. (6.4), where p is the spline degree, which is one less than the order of the piecewise polynomial k. We have used a conventional averaging method [56] (Eq. (6.4)) for generating the knot vector and utilized a constant value of $p = 3$ (i.e. $k = 4$) for this demonstration.

$$\begin{aligned} U_0 = \cdots = U_p &= 0 \\ U_n = \cdots = U_{n+p} &= 1 \\ U_{j+p} = \frac{1}{p}\sum_{i=j}^{j+p-1} u_i \quad &for\ j = 1, 2, \ldots, n-p \end{aligned} \tag{6.4}$$

In order to determine the NURBS curve, which fits the parameterized points u, the unknown control point coordinates ($v_i = \{x_i, y_i, z_i\}$) and weights ($\boldsymbol{w} = [w_i]$) must be identified. For programmatic convenience, we setup the NURBS formulation in a compact matrix form similar to [56]. The detailed formulation is shown in the Appendix E. The matrices defining the basis functions ($\boldsymbol{B}$), homogeneous coordinates of control points ($\boldsymbol{X,Y,Z}$) and weights ($\boldsymbol{w}$) are shown in Eq. (E.2), whereas the matrix arrangement of the coordinates of measured points ($\boldsymbol{\bar{X}, \bar{Y}, \bar{Z}}$) is shown in Eq. (E.6). Using the Eq. (E.7), we can solve for the unknown homogeneous coordinates of control points ($\boldsymbol{X,Y,Z}$) and the corresponding weights ($\boldsymbol{w}$) for a given choice for the number of control points (n). In our present study, for simplicity, we used a constant value of weights, $w = 1$, for every control point. Hence, we can re-arrange Eq. (E.7) to obtain Eq. (6.5), using which we can compute the unknown homogeneous coordinates of control points ($\boldsymbol{X,Y,Z}$).

$$\begin{aligned} \boldsymbol{B^T B X} &= \boldsymbol{\bar{X} B w} \\ \boldsymbol{B^T B Y} &= \boldsymbol{\bar{Y} B w} \\ \boldsymbol{B^T B Z} &= \boldsymbol{\bar{Z} B w} \end{aligned} \tag{6.5}$$

Once, $\boldsymbol{X,Y,Z}$ values are computed for a given choice of number of control points (n), the location coordinates of the control points are conventionally evaluated using Eq. (6.6). In our case, $w_i = 1$, the location coordinates are the same as the homogeneous coordinates of control points.

$$\begin{aligned} x_i &= X_i / w_i \\ y_i &= Y_i / w_i \quad \textit{for } i = 1, 2, \ldots, n \\ z_i &= Z_i / w_i \end{aligned} \tag{6.6}$$

After the control points are evaluated, we compute the fitting error using Eq. (6.7), wherein the root-mean square error (RMSE) of distances between the measured points and the points on the fitted curve are evaluated. The RMSE value is computed for each of the section curves and represents the average fitting error per curve.

$$RMSE = \sqrt{\frac{\sum_{t=1}^{m}\left(\overline{Q_t} - C(u_t)\right)^2}{m}} \tag{6.7}$$

The process is iteratively repeated for different choices of number of control points (n), in order to obtain an ideal choice of n for which the fitting error is reduced to a value below a user defined tolerance. The value of n could vary from $k = 4$ (i.e. order of the piecewise polynomial) to $m = 400$ (the number of measurement points). Typically, for computational efficiency, the choice of n is chosen as the smallest value at which the RMSE values of each of the section curves reaches a value lower than the tolerance value. In our use case, due to the relatively lower number of control points (less than or equal to 400 points per curve section), the execution time for the fitting process was within 10 minutes for all possible choices of n. The choice of tolerance value is user-defined, and we have chosen a value of 10^{-3} mm for this use case, which is a relatively small error margin, while considering all the points across a curve section, thereby ensuring a reasonable fit. The decrease in RMSE values versus number of control points has been plotted using the boxplot function [131] in MATLAB, as shown in Figure 6.5. For each choice for the number of control points, there are 20 RMSE data points corresponding to 20 curve sections. The box represents the values within the interquartile range with the line within the box representing the median value. RMSE values which are 1.5 times the interquartile range away from the top or bottom of the box are classified as outliers while using the boxplot function. As expected, the RMSE values decreases by increasing n for both the front (Figure 6.5 (a)) and the back (Figure 6.5 (b)) surfaces and reaches a value below 10^{-3} mm for all the curves at $n = 390$ for the front surface and $n = 350$ for the back surface, respectively, which are used for the present analysis. The coordinates of the control points are programmatically written into a CSV file and passed to the CAD tool. The fitting process is repeated for both the measured surfaces (i.e. the front surface and the back surface) of the blade in this use case.

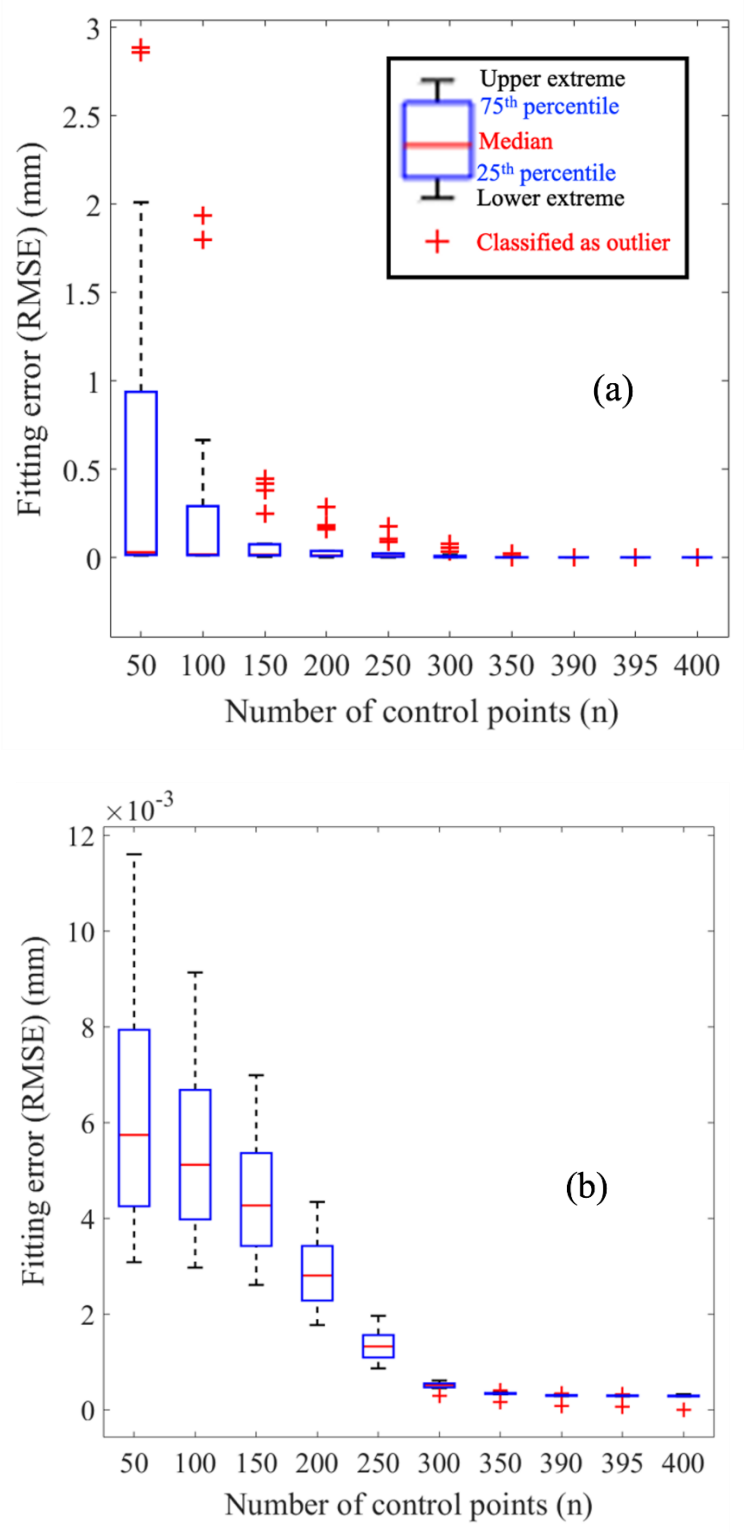

Figure 6.5. Decreasing fitting error (each boxplot consists of 20 data points corresponding to the RMSE values computed in each of the 20 curve sections) with increasing number of control points for (a) the front surface and (b) the back surface.

Finally, we apply a surface skinning approach [128,132] to interpolate a NURBS surface through the section curves by utilizing the control point coordinates, directly via a wrapper code developed using the NX APIs. A surface $S(u, v_r)$ is interpolated through the r section curves $C_r(u)$ such that $S(u, v_r) = C_r(u)$. A function to interpolate across the NURBS section curves was available via the NX APIs, namely "*CreateBsurfThruPts"*, which was used for importing the coordinates of control points and degree of the piecewise polynomials within the CAD tool and ultimately creating new front and back surfaces within the nominal CAD model. Additionally, the lateral surfaces were updated corresponding to the new front and back surfaces of the blade. The capability to track the relevant surfaces by means of the feature identifiers and the PMI notes within the MFIN (as explained in Section 6.1.2) was used to delete and update the appropriate nominal surfaces corresponding to the extracted measurement datasets.

6.2.4 Structural analysis of the turbofan assembly with damaged blade

After creating the MFIN XML instance of the after-use turbofan assembly with a damaged blade, we utilize the framework to conduct a finite-element analysis for evaluating the in-service stresses. We created two FE models – (i) with nominal design geometry or the "as-designed" case and (ii) with the updated geometry or the "after-use" case. The geometries for both the models were retrieved from their respective MFIN XML instances using programmatic methods (described in Section 4.1.2 in Chapter 4). In both the models, the turbofan assembly was simulated at the typical maximum rotational speeds during service. As shown in Figure 6.6, a static analysis was performed on the axisymmetric sector ($1/30^{th}$ of the turbofan) with the maximum load corresponding to ω = 3000 rpm at an inlet temperature of 288℃ [133]. To emulate the constraint imposed by a shaft on the turbofan, a displacement constrained boundary condition ($u_{rr} = u_{\theta\theta} = u_{zz} = 0$) was applied at the inner surface of the hub (Figure 6.6). The shrink fit loads between the hub and the shaft have been ignored for the current analyses. Due to the complexity of the geometries in each of the two models, they were meshed with quadratic tetrahedral elements in both the hub and the blade regions. The average element size chosen for the analyses was 10 mm, which was selected after conducting a mesh sensitivity analysis such that the maximum principal stresses did not change by further reducing the size of the mesh elements. Additionally, a tie constraint was applied at the intersecting nodes between the hub and the blade to prevent rigid body translation during the FE simulation.

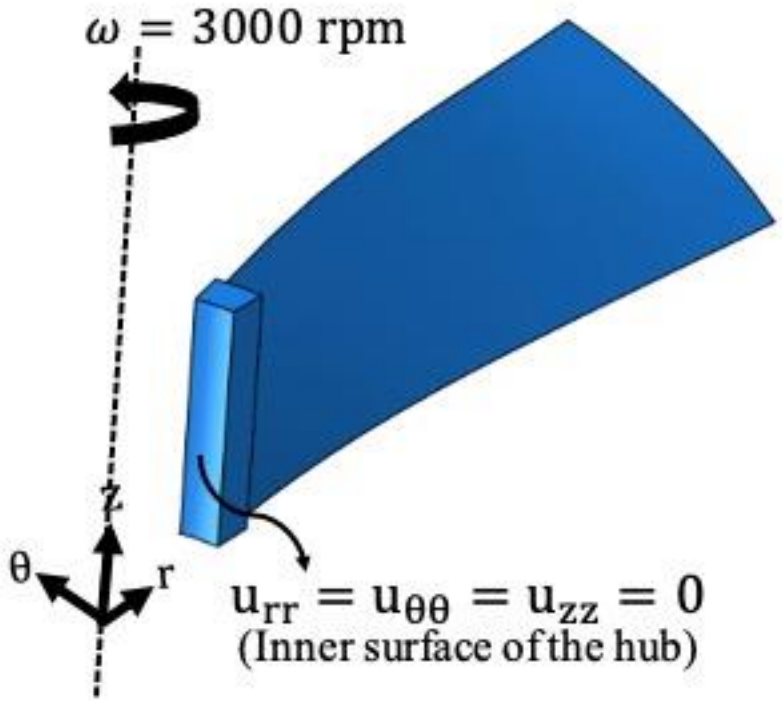

Figure 6.6. The applied loads and boundary conditions for the finite-element analysis model (shown here for the nominal geometry).

For the FE analysis, we used a classical elastoplastic material model following Johnson-Cook type hardening rule (Eq. (6.8)) [93], wherein the flow stress ($\bar{\sigma}$) is a function of the equivalent plastic strain ($\bar{\varepsilon}$) and temperature (T). The parameters A, B, c_1, c_2, T_{room} , T_{melt} in Eq. (6.8) correspond to the yield stress, strain hardening coefficient, strain hardening exponent, temperature exponent, room temperature and melting temperature, respectively. Additionally, the mass density (ρ) and the elastic properties, namely the Young's modulus (E) and the Poisson's ratio (ν) were utilized for the analysis. The values used for these properties for Ti-6Al-4V at the applied temperature (T=288℃) is shown in Table 6.2 [134]. After completing the analysis for both the as-designed and after-use cases, the maximum principal stress fields were exported in individual CSV files, comprising the element coordinates (i.e. corresponding to individual locations within the turbofan) followed by the magnitude of the maximum principal stress values and linked within the corresponding MFIN XML files for downstream access (Section 4.2).

$$\bar{\sigma} = (A + B\bar{\varepsilon}^{c_1})\left[1 - \left(\frac{T - T_{room}}{T_{melt} - T_{room}}\right)^{c_2}\right] \quad (6.8)$$

Table 6.2. Material properties of Ti-6Al-4V at 288 ℃ which were utilized for the FE analysis.[134]

Material properties	Values
Density (ρ) (kg/m^3)	4420
Young's Modulus (E) (GPa)	92.22
Poisson's ratio (ν)	0.357
Yield stress (A) (MPa)	728.7
Strain hardening coefficient (B) (MPa)	498.4
Strain hardening exponent (c_1)	0.28
Temperature exponent (c_2)	1
Melting temperature (T_{melt})(℃)	1599

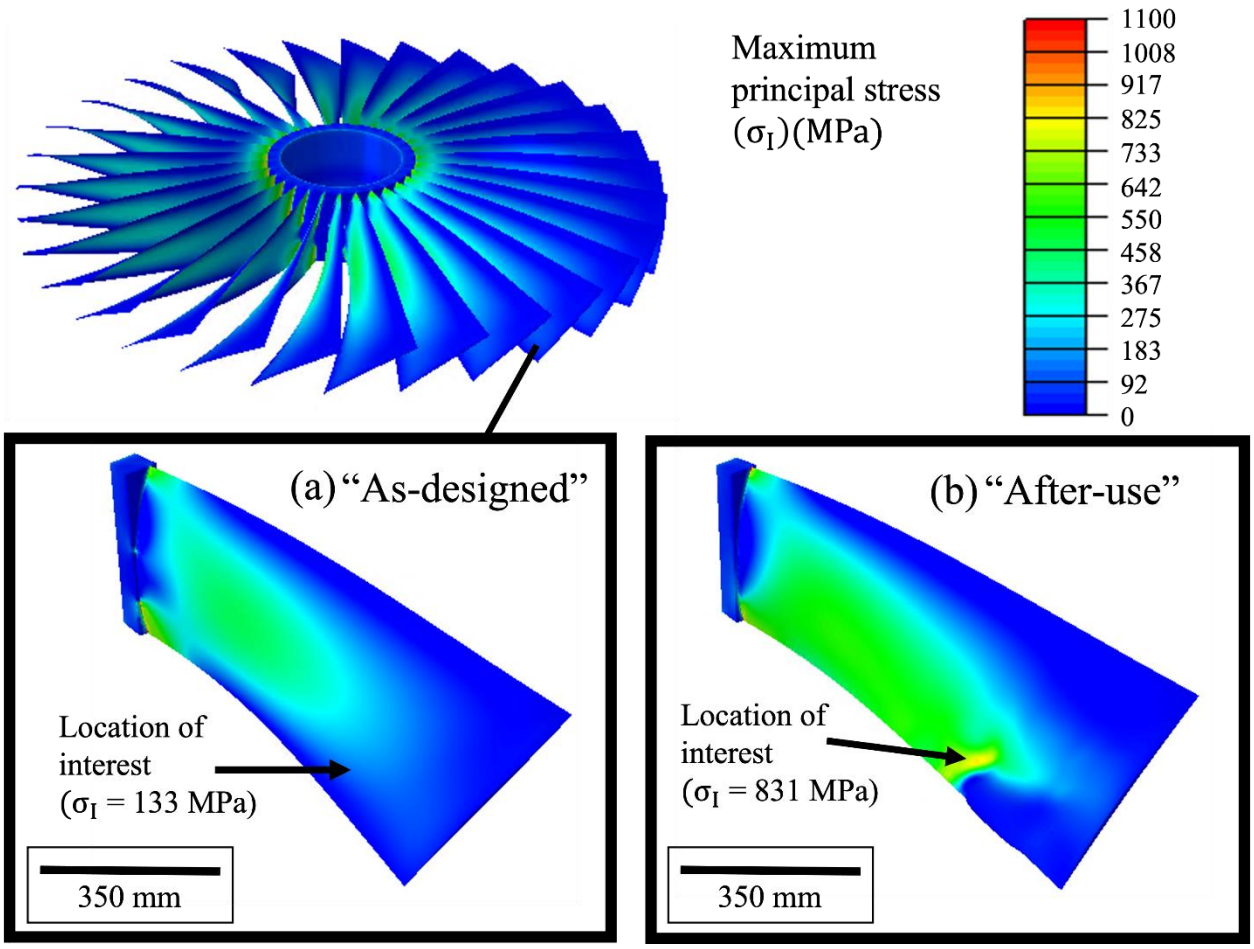

Figure 6.7. Maximum principal stress (σ_I) distribution in the turbofan assembly with variations observed in the local stresses (at regions within the blade) while using (a) the nominal geometry (or as-designed) versus (b) the updated geometry with FOD (or after-use).

Local variations in the maximum principal stress distribution were observed between the two models as shown in Figure 6.7. While using the after-use model, the maximum principal stress in the region of foreign-object damage is significantly larger in magnitude ($\sigma_I = 831$ MPa as shown in Figure 6.7(b)) as opposed to the as-designed model ($\sigma_I = 133$ MPa as shown in Figure 6.7(a)). The increased local stresses observed in the after-use model are due to the sharp geometric cusps leading to stress concentrations in the blade due to the foreign object damages on its surfaces, which was effectively captured in the analysis. The demonstration illustrates the importance of using the appropriate geometry in the stress analysis to capture the precise stress distribution. Conducting stress analysis is a crucial step for assessing the structural integrity of the component,

including conducting downstream high cycle fatigue, damage tolerance, and creep analyses, and ensuring that the component is fit for purpose under operating conditions. Failures often tend to originate when cracks develop at regions of high stresses and these regions are considered critical for estimating the remaining life of the entire component (Section 3.4.2 and Section 4.3). Hence, the process illustrated in this work to inform the after-use geometry for the analysis by effectively utilizing coordinate measurement datasets, enabled by the MFIN framework, presents opportunities to reduce errors in structural integrity analysis and effectively aid in decision-making during the MRO process. Moreover, the linking methodology utilized in the framework also enables dynamic access to the most recent measurement datasets, thereby capturing the current geometric state of the product - which can be subsequently utilized for downstream analysis. We would like to point out that the use case of FODs on turbofan blades presented in this work is an illustration, however, a similar workflow can be applied for in-service incidents with minor wear in the blades and systematic analysis can be conducted with minimal manual interventions - to make decisions regarding using the part as-is, repairing the part or retiring from service.

6.3 Discussion

We presented a use case for facilitating improved precision during the MRO decision stages of the lifecycle, but a similar approach can be applied during the MRB process during the acceptance and certification of as-manufactured components. The MFIN framework and the developed workflow can be used to capture geometric deviations in the manufactured components by utilizing the coordinate measurement datasets and for creating as-manufactured geometries to facilitate further analysis prior to decision-making regarding the disposition of individual components. Additionally, the framework and its programmatic process is setup in a way, which provides flexibility to replace the surface fitting algorithm code(s) utilized in the current work with another code depending on the product under consideration, requiring minimal changes to the overall workflow. To conduct structural analysis of components during MRB, a primary challenge has been that the geometric inspection data, material data, and performance requirements documents are scattered in multiple systems due to the involvement of multiple teams across the product lifecycle from both the supplier side as well as the original equipment manufacturers [122]. The MFIN framework acts as a portal to access pertinent datasets applicable to a component and can potentially enable MRB engineers to conduct analyses seamlessly on individual non-

conformal components and arrive at a more-informed decision (e.g. accepting the part as is, accepting with concessions, repairing the part with secondary manufacturing processes, or scrapping it altogether). The decisions made for each non-conformal component can be tracked using its MFIN UUIDs, which can provide knowledge for aiding engineers in decision-making when a similar non-conformance occurs again. Since MFIN starts to integrate the product lifecycle datasets for each serialized component, we start creating digital twins [2] of the components. Moreover, this work supports a digital engineering framework, whereas the automated flow of information within the analysis tools supports more informed decision-making during the various lifecycle stages of the individual components.

7. CONCLUSION AND FUTURE SCOPE

7.1 Chapter 3: Data Embedding approach

In Chapter 3, we presented a data embedding approach to store and retrieve spatially varying material definitions tied to a component, directly via CAD models. The approach uses point objects (or datum points) within CAD models as containers for storing the metadata. These points, defined by their location coordinates, act as spatial attribute markers and naturally provide context of where the stored metadata is applicable within the component domain. This capability was developed as a plug-in for the CAD software, thereby allowing engineers to use CAD models as a medium to exchange geometric and non-geometric data across the product lifecycle. Hence, by means of the data embedding tool, we expanded the model-based definitions (MBDs) capabilities to include spatially varying material behavioral information.

The key findings from this work can be summarized as follows:

1) The use of MBDs to store and exchange material behavioral data directly via the CAD model of a part can reduce the likelihood of error caused by more direct human interaction with the data.
2) A specific use case has been demonstrated using residual stress data, predicted via process modeling, and experimentally characterized, and stored spatially within the CAD model of a turbine disk. Part-to-part variations have been captured based on the uncertainty in the residual stress models and propagated to identify the subsequent variability in the predicted fatigue life, via a damage tolerance analysis, at specific locations within the turbine disk. Historically, this type of information would have been captured in textual form, often paper-based, with no direct ability to connect it consistently to the geometry to which it was related. By being able to capture this information digitally within the model, the designers (and other engineers) will be able to maintain the connectivity and provenance of information.
3) Lastly, this approach presents new opportunities to utilize location-specific material behavioral information as an additional design parameter during the product development stages and to explore newer performance-based designs.

7.2 Chapter 4: Data linking framework via MFIN

In Chapter 4, we developed a framework, namely a Model-based Feature Information Network (MFIN) for tracking, updating and retrieving material information applicable to a component throughout its product lifecycle, in order to ultimately realize a digital twin representation. The framework involves a data model in an XML file format (MFIN XML), defined by its schemas (MFIN application schemas), to create data linkages between the component's geometry and feature definitions originating from its CAD model and material definitions stored in a materials database software. For defining location-specific material definitions within a component, the framework has adopted the use of datum points to define distinct locations within its design model, wherein linkages to the applicable material datasets have been created. In order to create the linkages of material definitions or utilizing the existing linkages to extract material datasets applicable to a feature, programmatic methods or wrapper code(s) have been created by using application-program interface (API) functionalities of both the MFIN and material database software. These wrapper code(s) have been utilized to provide material definitions for structural analysis, thereby creating a data integration between the MFIN and FE analysis tool. Additionally, the MFIN application schemas have been created to capture the analysis model definition and analysis result datasets, for future usage and to make decisions during the product lifecycle. The key benefits from the presented work are as follows:

- The developed linking methodology creates dynamic linkages to the material data, thereby allowing continual updating of the material information applicable to the component and its features. The linkages provide access to the current material state information at a given point in its lifecycle, which can be retrieved and utilized to forecast the future performance of the component.
- The capability to include and exchange location-specific material definitions has been illustrated with a use case, wherein a linear friction welded Ti-6Al-4V compressor blisk component has been used. Within the regions in the blisk component, manufacturing process induced microstructure information (i.e. average grain size) and residual stress fields have been included and utilized for damage tolerance analysis. The variation in the estimated fatigue life, with and without including location-specific material information has been demonstrated. Hence, by including and utilizing location-specific

material state definitions, we can effectively improve precision in fatigue life estimates of the components.

- Furthermore, the demonstrated capability to track and retrieve processing-induced location-specific material information can also be extended for informing other sophisticated physics-based predictive models. This opens up newer opportunities to explore for improved precision in fatigue life estimates by applying information physics-based relationships.

Furthermore, the MFIN framework and methodology is expandable to meet other needs for realizing a digital twin as follows:

(1) The data integration between the MFIN and a commercial FE analysis code has been presented in this chapter, wherein the material information applicable to a component is provided using linkages in the MFIN, for the analysis. Similarly, the framework can be expanded to access and utilize other commercial software code(s), which could be useful for design and analysis of a component, by including necessary schemas and wrapper code(s) to create the data integration.

(2) The MFIN framework presented in this thesis has been limited with the focus on capturing material data applicable to the component. However, the same approach is expandable to form linkages to store and exchange other product lifecycle data which are applicable to the component and its features. While doing so, the MFIN starts to form a network of lifecycle data mapped to the features in the component, thereby creating a digital thread for data exchange. Hence, for each serialized component, there will be a MFIN file, containing the linkages to the lifecycle data from design to retirement. These data linkages, from a fleet of components, can be used to provide datasets for informing decision making during the design, manufacturing and sustainment stages of a newer version of the component.

7.3 Chapter 5: Enabling microstructure-sensitive location-specific fatigue life assessment via MFIN

In Chapter 5, we extend the MFIN framework to inform pertinent material state information of component within a physics-based fatigue life prediction model. Hence, a paradigm shift in component analysis is proposed through the development of a holistic framework for microstructure-sensitive, location-specific lifing of components. The MFIN framework was utilized for tracking and retrieval of processing-induced microstructural information and stress/strain states resulting from in service loading conditions at distinct locations in the component for use within a crystal plasticity fatigue life prediction model. A use case for lifing a dual-microstructure heat treated (DMHT) LSHR turbine disk component is demonstrated at two locations, near the bore (fine grains) and near the rim (coarse grains) regions. The conclusions from this chapter are twofold:

1) Identifying material allowable life by utilizing location-specific microstructural knowledge in the component:

- We demonstrated reduced uncertainties in the fatigue life distributions of LSHR in the DMHT turbine disk component and the associated minimum life (B0.1 life) by treating datasets corresponding to individual locations as separate distributions, which was enabled by the MFIN framework. The fatigue life predictions were obtained via crystal-plasticity finite element (CPFE) analysis, using statistically equivalent microstructures (SEMs) of the material, which were simulated under uniaxial loading conditions, akin to fatigue testing using virtual specimens. This approach presents opportunities to improve precision while determining the allowable minimum life by accounting for underlying microstructures at distinct locations in the component as opposed to the conventional approach of treating the entire component as a single monolithic structure with uniform microstructure.
- The use of the microstructure-sensitive predictive analysis demonstrated in this study also presents opportunities to (i) reduce the overall number of tests needed to identify the minimum life, (ii) better understand the process-structure-property-performance relationship in the material by simulating multiple SEMs and (iii) reduce time and costs associated with material testing during the product development stages.

2) A physics-based approach to assess fatigue life of components:

- A significant advancement in the present work is the extension of CPFE simulations to inform component scale life predictions. The principal strains from locations of interest in the component, calculated from component-level FE analysis, were precisely retrieved, and utilized in the MFIN framework to inform multiaxial displacement boundary conditions in the sub-scale CPFE analysis. The location-specific fatigue life predictions facilitate opportunities to determine the critical or life-limiting locations of components with gradient microstructures.
- The framework and the lifing approach presented in this work provides new opportunities to design the component and tailoring site-specific microstructures simultaneously, thereby evaluating the fatigue tradeoffs upfront during the product design stage. By identifying location corresponding to minimum life, one could potentially explore revisions to the design of the component geometry and/or the site-specific microstructure, for ultimately enhancing the performance of the overall component.
- The hierarchical modeling approach does not rely on performing CPFE simulations for the entire component, thus providing judicious use of computational resources. Based on the combination of the component geometry, applied loading state, process and microstructure information, as well as legacy records tied to prior versions of the component, lifing engineers can down-select the critical locations of components and utilize the proposed framework to perform higher fidelity CPFE simulations. Additionally, the framework inherently addresses for the microstructural variability via simulating multiple SEMs, avoiding microstructure homogenization approaches, thus accounting for extreme values of the microstructural attributes while lifing components.

7.4 Chapter 6: Creating connectivity between geometric inspection and structural analysis via MFIN

In Chapter 6, the MFIN framework was expanded to enable data connectivity between geometric inspection and stress analysis by facilitating automated flow of geometric information of a product within the structural analysis tools.

- The presented workflow is valuable for engineers to make more informed decisions during the product lifecycle (i) by assessing as-manufactured part geometries that fall out of

specifications during the materials review board (to decide whether to accept the part as is, accept with concessions, repairing the part with secondary manufacturing processes, or scrapping it altogether) and (ii) by inspecting in-service damages in parts during the maintenance, repair, or overhaul (MRO) process (to decide whether to use as-is, repair or retire). Often in these cases, the decision-making relies on engineering intuition (based on nominal designs) or one-off analyses that are time-intensive and costly. These barriers are removed by utilizing the automated workflow, which enables using the inspection data for informing current part geometries within the stress analysis.

- The use case presented in this work is based on aiding decision-making by an MRO engineer performing inspection on fielded turbofan blades, after an in-service usage experiencing foreign object damage (FOD). We utilize coordinate measurement datasets to capture deviations in the blade surfaces due to FOD and incorporate the after-use geometry within stress analysis, by means of the developed workflow, thereby demonstrating the implications of the FOD on the local stresses in the part. The use case illustrates the importance of using precise geometry of a product within the stress analysis for improving downstream decision-making, and the presented workflow enables seamlessly conducting these types of analyses.

For creating this workflow, the MFIN framework was utilized to link and retrieve coordinate measurement datasets applicable to individual geometric features within the component. Programmatic wrapper code(s) were utilized to access the pertinent measurement datasets and updating the nominal geometries in the CAD file with current geometric definitions of the part. For the use case presented in this chapter, we used a two-step surface fitting process to effectively capture the deviations in the surfaces of the blade with minimal errors, which involved fitting NURBS curves to the measurement datasets and generating section curves of the blade, followed by skinning or interpolating a surface across the section curves. The workflow is flexible to incorporate utilization of a different external code to inform the geometry instead of a NURBS surface fitting code, with minimal changes to the programmatic process. The MFIN framework enabled automating the process of creating the next instantiation of the CAD model for the specific fielded component by using the tracking capability and updating the appropriate surfaces within the nominal CAD model with the fitted surfaces. Finally, by using the programmatic connectivity

of MFIN to stress analysis tools, we inform the geometry data and the materials information for seamlessly performing the stress analysis.

Lastly, the MFIN framework presents opportunities for developing workflows to reduce manual intervention by engineers and speeding up the assessment of parts during the product lifecycle. Historically, the information accumulated during the product lifecycle is collected and stored in siloed databases, with no direct ability to maintain associativity to the serialized part and its geometry. By means of the presented framework, we can potentially maintain connectivity between lifecycle datasets and the geometric features within the design model of a serialized part, thereby allowing engineers to harness the information readily and use them for decision-making.

7.5 Future opportunities for component assessment via a digital twin approach

Based on the research presented in this thesis, the following future work is suggested:

(1) For the case studies presented in this work, we have utilized fatigue loading with a constant amplitude. However, we know that aerospace components encounter complex loads with varying amplitudes during service and each serialized component is exposed to distinct loading experience. By means of the MFIN framework and its unique identifier mechanism to track product lifecycle data pertinent to a component, we can start to record the loading spectrum tied to each serialized component during its service, and further use the information for fatigue life analysis via predictive models. In the approach presented in Chapter 5, we can conduct component-scale FE analysis with actual loads, to ultimately obtain more precise boundary conditions for the CPFE analysis. We could also use the MFIN framework to inform the variable amplitude loading for CPFE simulations. Hence, by using more realistic loading conditions, via the digital twin approach, we can explore further improvement in precision within life prediction analyses for (i) selecting number of lifecycles after which a specific component requires inspection and (ii) make improved decisions regarding life extension of the component.

(2) The MFIN framework is expandable to enable a fully model-based approach for assessing components upfront during the design stages. By creating necessary MFIN schemas and wrapper code(s), we can integrate process models and associated code(s), for predicting: (i) full field residual stress distributions in a component, and location-specific (ii) grain

size distributions, (iii) precipitate distributions, (iv) porosities, (v) inclusions, and (vi) surface treatments. Thereby, we can potentially start using the MFIN framework to inform additional microstructural descriptors within the microstructure-sensitive location-specific lifing framework and subsequently explore further improvement in the fatigue life predictions by accounting for additional physics-based knowledge. Furthermore, the integration of the MFIN framework with predictive process models, can facilitate new opportunities to optimize manufacturing process parameters for meeting targeted location-specific performance, upfront during product development stages.

APPENDIX A. DETERMINATION OF GEOMETRIC CORRECTION FACTOR EXPRESSION APPLICABLE FOR THE TURBINE DISK IN CHAPTER 3

In Chapter 3, a finite-element approach was used to determine the geometric correction factors (F(a/w)), that apply for cracks at locations 1 and 2 (shown in Figure 3.8(b)) of the turbine disk. The process involves simulating the nominal stresses without the presence of a crack in the model and simulating the stress response with explicitly insertion of cracks at these model locations. Simulations have been repeated with cracks of increasing lengths at each zone location to obtain the stress fields ahead of the crack in each simulation. The ratio of the maximum stress field ahead of the crack tip versus the stress present in the simulations without a crack (Section 3.4.2) forms the dataset for obtaining the geometric correction factor as a function of crack length for each location. A blunt tip crack with the shape of a U notch has been explicitly modeled in each location, with the initial crack length (a_i) of length $a = 0.10$ mm and constant width ($w = 0.5$ mm). Material properties applied to the crack section were E=10 Pa (several magnitudes lower than the material property in disk section), $\nu = 0.3$ and a density $\rho = 0.599$ kg/m^3 (density of air at 600 ℃). Linear, quadrilateral mesh elements have been used for the analysis. The mesh has been refined around the crack geometry and a mesh sensitivity analysis was performed to identify the appropriate resolution ahead of the crack tip. The simulations have been performed using the same loads and boundary conditions as described in Section 3.4.2 for six different increasing crack sizes in each zone to obtain the maximum principal stresses ahead of the crack tip. For each zone, the datasets are fit using a second-order and third-order polynomials to obtain the $F\left(\frac{a}{w}\right)_{\text{Zone 1}}$ and $F\left(\frac{a}{w}\right)_{\text{Zone 2}}$, respectively, as shown in Eq. (A. 1) and Eq. (A. 2).

$$F\left(\frac{a}{w}\right)_{Zone\ 1} = -107.9\left(\frac{a}{w}\right)^2 + 37.9\left(\frac{a}{w}\right) + 1 \qquad \text{(A. 1)}$$

$$F\left(\frac{a}{w}\right)_{Zone\ 2} = 134.2\left(\frac{a}{w}\right)^3 - 77.24\left(\frac{a}{w}\right)^2 + 25.33\left(\frac{a}{w}\right) + 1 \qquad \text{(A. 2)}$$

APPENDIX B. ACQUISITION OF RESIDUAL STRESS DATASETS FOR LINEAR FRICTION WELDED BLISK COMPONENT

For creating residual stress data in Chapter 4, the reported characterization data [89] obtained using energy dispersive X-ray diffraction (EDD) were used as a starting point. A sample of linear friction welded Ti-6Al-4V to Ti-6Al-4V plate was characterized by the diffracted intensity of high energy X-rays captured with detectors, by performing rotations to the sample, thereby obtaining the lattice strains in the α and β phases of Ti-6Al-4V corresponding to different families of planes along a series of scanned locations relative to the weld region. Using the acquired datasets, the elastic strain tensor at each scanned location has been computed and reported in [89]. This process was repeated for multiple locations spatially near the weld, by performing multiple line scans across the sample. From the reported residual strain tensors, for the present work, we acquired datasets corresponding to the α phase of Ti-6Al-4V, having family of planes with Miller indices (i.e. three digit Miller indices{h,k,l}) values of {102}. A coordinate mapping was performed to associate the reported residual strain datasets with the coordinate system used in the current work (i.e. $\varepsilon_{11}, \varepsilon_{22}, \varepsilon_{33}$ in [89] correspond to ε_{ZZ}, ε_{XX}, ε_{YY}, respectively). For each of the reported spatially varying residual strain components, data were extracted at 91 locations within the weld region (45 locations on each side of the weld interface and 1 location at the weld interface). The Young's modulus (E_{hkl}) and Poisson ratio (ν_{hkl}) corresponding to {102} were computed using Eq. (B.1) and Eq. (B.2) [135], which are necessary for computing the residual stress components.

$$E_{hkl} = \frac{\left[h^2 + \frac{(h+2k)^2}{3} + \left(\frac{a}{c}l\right)^2\right]^2}{\left[s_{11}\left(h^2 + \frac{(h+2k)^2}{3}\right)^2 + s_{33}\left(\frac{a}{c}l\right)^4 + (s_{44} + 2s_{13})\left(h^2 + \frac{(h+2k)^2}{3}\right)\left(\frac{a}{c}l\right)^2\right]} \tag{B.1}$$

$$\nu_{hkl} = \frac{\left[h^2 + \frac{(h+2k)^2}{3} + \left(\frac{a}{c}l\right)^2\right]\left[s_{12}\left(h^2 + \frac{(h+2k)^2}{3}\right) + s_{13}\left(\frac{a}{c}l\right)^2\right]}{\left[s_{11}\left(h^2 + \frac{(h+2k)^2}{3}\right)^2 + s_{33}\left(\frac{a}{c}l\right)^4 + (s_{44} + 2s_{13})\left(h^2 + \frac{(h+2k)^2}{3}\right)\left(\frac{a}{c}l\right)^2\right]} \tag{B.2}$$

In Eq. (B.1) and Eq. (B.2), the lattice parameters $a = 2.931$ Å and $c = 4.660$ Å for the α-phase were used [89]. The elastic compliance matrix terms (s_{ij}) were obtained from the elastic stiffness matrix (C_{ij}), for which $C_{11} = 169.66$ GPa, $C_{12} = 88.66$ GPa, $C_{13} = 61.66$ GPa, $C_{33} = 181$ GPa, $C_{44} = 42.50$ GPa, $C_{66} = 40.5$ GPa values corresponding to the α-phase of Ti-6Al-4V [136] have been used.

The residual stress components σ_{xx}, σ_{yy}, σ_{zz} were computed using the tensorial equation (Eq. (B.3)), wherein i, j are the free indices and λ_{ij} represents the Kronecker delta.

$$\sigma_{ij} = \frac{E_{hkl}}{1 + \nu_{hkl}} \varepsilon_{ij} + \frac{(E_{hkl}\, \nu_{hkl})}{(1 + \nu_{hkl})(1 - 2\nu_{hkl})}\, \varepsilon_{kk} \lambda_{ij} \tag{B.3}$$

After obtaining the residual stress components (in MPa) for each of the 91 locations within the weld region, a regression fit is applied, in order to create a functional form to define the residual stress distribution. A Fourier type fit was chosen to fit the residual stress data [137,138], and the function form of the residual components $\sigma_{XX}(X)$, $\sigma_{YY}(X)$, $\sigma_{ZZ}(X)$ used for the case study is shown below in Eqs. **(**B.4**)-(** B.6**)**. In the study [89], the symmetry of ε_{XX} and ε_{ZZ} components of residual strains across the weld center were reported, however, we observe an asymmetry in the σ_{XX}, σ_{YY} and σ_{ZZ} components of the residual stresses about the weld center (shown in Figure 4.3(b)), which is due to the contribution of the asymmetry in ε_{YY} component that is included while evaluating the stress components using Eq. (B.3).

$$\sigma_{XX}(X) = -8.296 + 16.23\cos(0.57X) + 30.6\sin(0.57X) - 11.83\cos(1.14X) - 0.29\sin(1.14X) \tag{B.4}$$

$$\sigma_{YY}(X) = 129.8 - 312.7\cos(0.3X) + 7.89\sin(0.3X) + 110.7\cos(0.6X) + 73.04\sin(0.6X) \tag{B.5}$$

$$\sigma_{ZZ}(X) = 215.6 + 361.2\cos(0.76X) + 21.76\sin(0.76X) \tag{B.6}$$

APPENDIX C. ESTIMATING INITIAL VALUES FOR CRYSTAL PLASTICITY MODEL PARAMETERS VIA A MACROSCOPIC OPTIMIZATION SCHEME USING THE KOCKS -MECKING FORMULATION

To obtain initial estimates for the crystal plasticity model parameters described in Chapter 5 initial reference stress g(0), initial dislocation density $\rho(0)$, constant corresponding to dislocation storage (k_1) and constant corresponding to dislocation annihilation (k_2), we adapted the formulation proposed in [107] and conducted a optimization process to calibrate against the macroscopic stress-strain data. This approach aids us in selecting reasonable model parameter values as starting points, which can be suitably modified via a trial-and-error approach to calibrate the final CP model parameters (presented in Section 5.3.1). This analysis also provides us insights on how the Kocks-Mecking parameters k_1 and k_2 vary based on the grain size in the microstructure. Additionally, the presented optimization scheme is computationally less intensive and allows us to run multiple iterations for selecting reasonable initial estimates. This process was repeated for calibration of CP model parameters for both the fine and the coarse grain microstructures of LSHR in the present work.

Let us consider the evolution of total dislocation density (ρ) with incremental plastic strain (ε_{pl}) via a Kocks-Mecking type expression [107], with a dislocation storage term and a dislocation annihilation term. The terms k_1 and k_2 are constants corresponding to dislocation storage and dislocation annihilation, respectively.

$$\frac{d\rho}{d\varepsilon_{pl}} = k_1\sqrt{\rho} - k_2\rho \tag{C.1}$$

Upon integrating Eq. (C.1), we can obtain an analytical expression of the dislocation density (ρ) as a function of plastic strain (ε_{pl}), initial dislocation density ($\rho(0)$), and the terms k_1 and k_2 as shown in Eq. (C.2). The initial dislocation density ($\rho(0)$) was obtained as the integration constant, by substituting $\varepsilon_{pl} = 0$.

$$\rho\left(\varepsilon_{pl}, k_1, k_2, \rho(0)\right) = \frac{\exp\left(-k_2\varepsilon_{pl}\right)\left(\sqrt{\left(k_1 - k_2\sqrt{\rho(0)}\right)^2} - k_1\exp\left(\frac{k_2\varepsilon_{pl}}{2}\right)\right)^2}{k_2^2} \quad \text{(C.2)}$$

Next, we utilized the expression obtained for $\rho(\varepsilon_{pl}, k_1, k_2, \rho(0))$ and substituted it within the Taylor hardening description as shown in Eq. (C.3). The macroscopic flow stress evaluated using Eq. (C.3) is denoted as σ_{model}. The constant term α is referred to as the interaction constant, which is typically of the order of unity and is dependent on the strength of dislocation-dislocation interactions [109]. The term $\rho(0)$ represents initial resistance to yielding and μ is the shear modulus.

$$\sigma_{model} = \sigma_0 + \alpha\mu b\sqrt{\rho(\varepsilon_{pl}, k_1, k_2, \rho(0))} \quad \text{(C.3)}$$

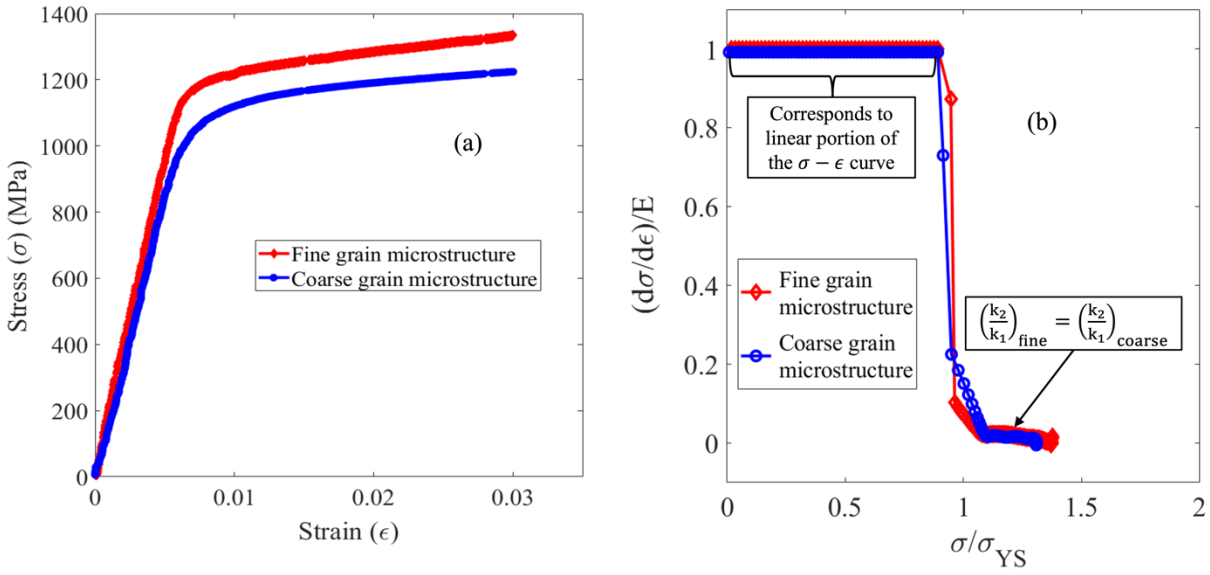

Figure C.1. Uniaxial tension test data for LSHR at 593℃ corresponding to the fine grain and coarse grain microstructures: (a) stress-strain data and (b) tangent modulus ($d\sigma/d\epsilon$) scaled over Young's modulus (E) versus stress (σ) scaled over yield stress (σ_{YS}).

To determine the unknowns $\sigma_0, \rho(0), k_1$ and k_2, we setup an optimization scheme. We utilize the stress strain data obtained from uniaxial tension tests (shown in Figure C.1.(a)) for this

purpose. The objective is to minimize the error (denoted as f(x)) between σ_{model} from Eq. (C.3) and the flow stress (σ_{exp}) from the uniaxial tension tests, as shown in Eq. (C.4).

$$\text{Minimize}: \quad f(\varepsilon_{pl}, k_1, k_2, \rho(0)) = \| \sigma_{exp} - \sigma_{model} \|_2 \tag{C.4}$$

For solving the optimization problem described in Eq. (C.4), the initial guesses for the unknown parameters were chosen as follows. The values of macroscopic yield stress were used as initial guesses for σ_0. For fine grain microstructure, an initial guess of $\sigma_0 = 1209$ MPa was used whereas for the coarse grain microstructure, an initial guess of $\sigma_0 = 1074$ MPa was used. In Ni-based superalloys, we typically expect $\rho(0)$ on the order of $10^5 - 10^6$ ($\frac{1}{mm^2}$). For both the fine grain and coarse grain microstructures, we assume a starting value of 10^6 ($\frac{1}{mm^2}$) in this analysis. Based on [107], a reasonable initial estimate for k_1 is $1/100\alpha b$. We utilized a value of 2.54 Å for the Burger's vector (b). Since, α typically ranges between 0.1 and 1 [109], we assumed a constant value of $\alpha = 0.3$. Finally, since we know from previous works [50,139], the value of k_2 is in the order 10, we assume a starting value of $k_2 = 10$, for both the microstructures. For accommodating a broader search space, random perturbations were applied to the initial guesses and 1000 optimization iterations were repeated.

Finally, using the optimization routine, we obtained the following estimates for the unknown quantities $\sigma_0, \rho(0), k_1$ and k_2 that minimized the error function $f(\varepsilon_{pl}, k_1, k_2, \rho(0))$. For the fine grain microstructure, we determined $\sigma_0 = 1183$ MPa , $\rho(0) = 10^6 \ \frac{1}{mm^2}$, $k_1 = 2.85 \text{ X } 10^6 \frac{1}{mm}$ and $k_2 = 30.38$. For the coarse grain microstructure, the values of $\sigma_0 = 1120$ MPa, $\rho(0) = 10^6 \frac{1}{mm^2}$, $k_1 = 1.68 \text{ X } 10^6 \frac{1}{mm}$ and $k_2 = 19.77$ were identified. We observe that the values of k_1 and k_2 for the fine grain microstructure is greater than the values obtained for the coarse grain microstructure. It was reported in [107] that k_1 is typically proportional to shear modulus μ. In our analysis, we utilize $\mu = 77.273$ GPa for fine grain microstructure and μ = 68.324 GPa for coarse grain microstructure, hence, the trends observed for k_1 were in accordance. Since, LSHR constitutes random texture, we can obtain initial resistance at the slip system level for the CP model parameter g_0 from σ_0, by dividing with the Taylor factor, which is 3.06. Hence, we obtain an initial estimate of $g_0 = 387$ MPa for the fine grain microstructure and

$g_0 = 366$ MPa for the coarse grain microstructure. The chosen initial estimates for $g(0), \rho(0), k_1$ and k_2 are summarized in Table C.1.

Table C.1. Initial estimates for crystal plasticity (CP) model parameters $g_0, \rho(0), k_1, k_2,$ for both the fine grain and the coarse grain microstructures of LSHR.

Parameters	Fine grain microstructure	Coarse grain microstructure
$g(0)$ (MPa)	386	366
$\rho(0)$ $(\frac{1}{mm^2})$	10^6	10^6
k_1 $(\frac{1}{mm})$	2.85 X 10^6	1.68 X 10^6
k_2	30.38	19.77

In addition to the parameters listed in Table C.1, we require choosing reasonable values for the constant parameters Γ_{act}, D, h_n in the expression which relates k_1 and k_2 (Eq. (5.7)). The term h_n is related to the interaction constant α, i.e., $h_n = \alpha^2$. Hence, we assign $h_n = 0.09$ for the present work. For the purposes of determining Γ_{act} and D, we utilize the values of $\frac{k_2}{k_1}$ for both the fine grain and coarse grain microstructures and substitute the values within Eq. (5.7) in Section 5.3.1. We obtained $\frac{k_2}{k_1} = 1.12\ X\ 10^{-5}$ for the fine grain microstructure and $\frac{k_2}{k_1} = 1.06\ X\ 10^{-5}$ for the coarse grain microstructure. Hence, we determine a combination of values for $\Gamma_{act} =$ 2.88 X 10^{-3} and $D = 53280$ MPa by trial and error, which satisfies the estimates of the ratios $\frac{k_2}{k_1}$ for both the microstructures, in Eq. (5.7). Lastly, it is worth noting that the values $\frac{k_2}{k_1}$ from our initial estimates were approximately equal in magnitude. The equal values of the ratio of $\frac{k_2}{k_1}$ observed in our analysis is further supported by Figure C.1(b). By using the experimental dataset and plotting the $(d\sigma/d\epsilon)/E$ (wherein E is the Young's modulus) versus σ/σ_{YS} (wherein σ_{YS} is the

yield stress) for both the microstructures, we can observe that the slope $d\sigma/d\epsilon$ eventually becomes equal, as pointed out in Figure C.1(b). Physically, this was in also in accordance to the expected behavior [109], i.e., as the material is strained, the rate of dislocation annihilation or removal eventually becomes equal to the rate of dislocation storage such that a steady state dislocation density is reached.

APPENDIX D. MARKOV CHAIN MONTE-CARLO SAMPLING AND METROPOLIS-HASTINGS ALGORITHM APPROACH FOR BAYESIAN INFERENCE ANALYSIS

To overcome the computational challenges in evaluating the integral of the likelihood function in Eq. (5.13), we resort to using Markov chain Monte-Carlo (MCMC) sampling approach, originally implemented in [49]. A Markov chain comprises a series of random variables wherein z^{th} term in the series depends only on the $(\mathrm{z}-1)^{th}$ term. We use Monte-Carlo sampling to identify the z^{th} term, which is chosen based on a proposal distribution. Finally, the Metropolis-Hastings algorithm is utilized to evaluate whether the proposed candidate will be accepted as the z^{th} term of the series. The algorithm involves computing a parameter p using Eq. (D.1). The term $\alpha_{\mathrm{r}}^{\mathrm{z}-1}$ is the $(\mathrm{z}-1)^{th}$ term in the Markov chain and corresponds to r^{th} parameter (r = 1 represents to $\mathrm{W}_{\mathrm{critical}}^{\mathrm{p}}$ and r = 2 represents hyperparameter s) and the term α_{r}^{*} represents the proposed candidate for the z^{th} term.

$$\mathrm{p}=\min\left(1,\frac{\pi(\mathrm{D}|\alpha_{\mathrm{r}}^{*})\pi_{0}(\alpha_{\mathrm{r}}^{*})\pi(\alpha_{\mathrm{r}}^{*}|\alpha_{\mathrm{r}}^{\mathrm{z}-1})}{\pi(\mathrm{D}|\alpha_{\mathrm{r}}^{\mathrm{z}-1})\pi_{0}(\alpha_{\mathrm{r}}^{\mathrm{z}-1})\pi(\alpha_{\mathrm{r}}^{\mathrm{z}-1}|\alpha_{\mathrm{r}}^{*})}\right) \tag{D.1}$$

The term $\pi(\alpha_{\mathrm{r}}^{*}|\alpha_{\mathrm{r}}^{\mathrm{z}-1})$ is the proposal distribution, which is proposes a candidate α_{r}^{*} based on $\alpha_{\mathrm{r}}^{\mathrm{z}-1}$. We can simplify the Eq. (D.1) to obtain Eq. (D.2), by assuming that $\pi(\alpha_{\mathrm{r}}^{*}|\alpha_{\mathrm{r}}^{\mathrm{z}-1})$ is symmetric.

$$\mathrm{p}=\min\left(1,\frac{\pi(\mathrm{D}|\alpha_{\mathrm{r}}^{*})\pi_{0}(\alpha_{\mathrm{r}}^{*})}{\pi(\mathrm{D}|\alpha_{\mathrm{r}}^{\mathrm{z}-1})\pi_{0}(\alpha_{\mathrm{r}}^{\mathrm{z}-1})}\right) \tag{D.2}$$

The Metropolis-Hastings relies on comparing the value of p obtained from Eq. (D.2) with a random number $\emptyset$ which takes the value between 0 and 1. The proposed candidate α_{r}^{*} is selected as the z^{th} term if $\emptyset \leq \mathrm{p}$. Otherwise, the $z-1^{th}$ term is assigned as the z^{th} term. The process is repeated until a convergence is achieved.

The convergence is determined by running M Markov chains in parallel. The variance of α_r between the Markov chains and within a Markov chain is described using W_{α_r} and B_{α_r}, respectively. Hence, a net variance (V_{α_r}) tied to the parameter α_r is determined by using Eq. (D.3).

$$V_{\alpha_r} = \frac{(M-1)}{M} W_{\alpha_r} + \frac{1}{M} B_{\alpha_r} \tag{D.3}$$

Finally, we evaluate the convergence metric R_{α_r}, by utilizing the values for V_{α_r} and W_{α_r}, as shown in Eq. (D.4). As the value of R_{α_r} approaches unity, a converged posterior distribution of the parameter α_r is obtained.

$$R_{\alpha_r} = \sqrt{\frac{V_{\alpha_r}}{W_{\alpha_r}}} \tag{D.4}$$

For the Bayesian inference analyses in this work, we utilized two Markov chains in parallel (i.e., M=2) and continued MCMC simulations up to $5 \text{ X } 10^5$ iterations. The calibration results for $W^p_{critical}$ is shown in Figure 5.6. The calibrated hyperparameters(s) followed lognormal distributions for both the microstructures. For fine grain microstructure, the mean value of the hyperparameter (s) was identified as 1,11,540 cycles and the corresponding standard deviation was 32184 cycles. Whereas, for the coarse grain microstructure, the mean value of the hyperparameter (s) was identified as 6710 cycles and the corresponding standard deviation was 1980 cycles.

APPENDIX E. COMPACT MATRIX FORM TO DESCRIBE NURBS CURVE FITTING PROBLEM

To satisfy the objectives in Chapter 6, to identify the modifications to the as-designed geometry based on the metrology measurements post-manufacturing, a framework is needed to mathematically define the surface geometry. For mathematical and programmatic convenience, we setup the NURBS curve fit in a compact matrix form similar to the approach proposed in [56]. Let the coordinates of points on the NURBS curve $C(u)$ be denoted with $x(u_i)$, $y(u_i)$, $z(u_i)$. By re-writing the terms in Eq. (2) in matrix form, followed by moving the denominator to the other side and swapping the left and right sides of the equation, we obtain Eq. (E.1).

$$\begin{aligned} \mathbf{b^T(u_i).X} &= x(u_i).\mathbf{b^T(u_i).w} \\ \mathbf{b^T(u_i).Y} &= y(u_i).\mathbf{b^T(u_i).w} \qquad \text{for i= 1, 2, …, n} \\ \mathbf{b^T(u_i).Z} &= z(u_i).\mathbf{b^T(u_i).w} \end{aligned} \tag{E.1}$$

X, **Y**, **Z** are vectors of size n x1 representing the homogeneous coordinates of control points and **w** represents a n x 1 vector with scalar weights corresponding to control points as shown in Eq. (E.2). The basis functions corresponding to each control point are organized in a vector **b** of size n x 1 as shown in Eq. (E.2).

$$\begin{aligned} \mathbf{X} &= [x_1w_1, x_2w_2, \dots., x_nw_n]^T \\ \mathbf{Y} &= [y_1w_1, y_2w_2, \dots., y_nw_n]^T \\ \mathbf{Z} &= [z_1w_1, z_2w_2, \dots., z_nw_n]^T \\ \mathbf{w} &= [w_1, w_2, \dots., w_n]^T \\ \mathbf{b} &= [B_1(u), B_2(u), \dots\dots\dots\dots B_n(u)]^T \end{aligned} \tag{E.2}$$

For fitting the measurement data $Q_t = \{[\bar{x}_t, \bar{y}_t, \bar{z}_t]^T\}_{t=1,2,..,m}$ with a NURBS curve, we replace $x(u_i)$, $y(u_i)$, $z(u_i)$ in Eq. (A.1) with $\bar{x}_t$, $\bar{y}_t$, $\bar{z}_t$, respectively, to obtain Eq. (E.3).

$$\mathbf{b^T(u_t).X} = \bar{x}_t.\mathbf{b^T(u_t).w}$$

$$\mathbf{b^T(u_t).Y} = \bar{y}_t.\mathbf{b^T(u_t).w} \qquad \text{for t= 1, 2, …, m} \qquad \text{(E.3)}$$
$$\mathbf{b^T(u_t).Z} = \bar{z}_t.\mathbf{b^T(u_t).w}$$

By expanding the matrices in Eq. (E.3) and grouping the known and unknown terms, we can re-write the problem in a compact matrix form as shown in Eq. (E.4). Hence, by using Eq. (E.4), we can solve for the least-squares solutions for **X**, **Y**, **Z** and **w**.

$$\begin{bmatrix} \mathbf{B} & \mathbf{0} & \mathbf{0} & -\bar{\mathbf{X}}.\mathbf{B} \\ \mathbf{0} & \mathbf{B} & \mathbf{0} & -\bar{\mathbf{Y}}.\mathbf{B} \\ \mathbf{0} & \mathbf{0} & \mathbf{B} & -\bar{\mathbf{Z}}.\mathbf{B} \end{bmatrix}_{3mX4n} . \begin{bmatrix} \mathbf{X} \\ \mathbf{Y} \\ \mathbf{Z} \\ \mathbf{w} \end{bmatrix}_{4nX1} = [\mathbf{O}]_{4nX1} \qquad \text{(E.4)}$$

The matrices **B** and $\bar{\mathbf{X}}$**,** $\bar{\mathbf{Y}}$**,** $\bar{\mathbf{Z}}$ are shown in Eqs. (E.5) and (E.6), respectively.

$$\mathbf{B} = \begin{bmatrix} B_1(u_1) & B_2(u_1) & \cdots & B_n(u_1) \\ B_1(u_2) & B_2(u_2) & \cdots & B_n(u_2) \\ \vdots & \vdots & \ddots & \vdots \\ B_1(u_m) & B_2(u_m) & \cdots & B_n(u_m) \end{bmatrix}_{mXn} \qquad \text{(E.5)}$$

$$\begin{aligned} \bar{\mathbf{X}} &= \text{diagnol}\{\bar{x}_1, \bar{x}_2, \ldots., \bar{x}_m\} \\ \bar{\mathbf{Y}} &= \text{diagnol}\{\bar{x}_1, \bar{x}_2, \ldots., \bar{x}_m\} \\ \bar{\mathbf{Z}} &= \text{diagnol}\{\bar{z}_1, \bar{z}_2, \ldots., \bar{z}_m\} \end{aligned} \qquad \text{(E.6)}$$

Based on the choices of m and n, Eq. (E.4) can be an overdetermined or underdetermined system. For convenience, we pre-multiple the Eq. (E.4) with the transpose of the coefficient matrix, followed by simplification using row operations to obtain Eq. (E.7)

$$\begin{bmatrix} \mathbf{B^TB} & \mathbf{0} & \mathbf{0} & -\mathbf{B^T}\bar{\mathbf{X}}\mathbf{B} \\ \mathbf{0} & \mathbf{B} & \mathbf{0} & -\mathbf{B^T}\bar{\mathbf{Y}}\mathbf{B} \\ \mathbf{0} & \mathbf{0} & \mathbf{B} & -\mathbf{B^T}\bar{\mathbf{Z}}\mathbf{B} \\ \mathbf{0} & \mathbf{0} & \mathbf{0} & \mathbf{M} \end{bmatrix}_{4nX4n} . \begin{bmatrix} \mathbf{X} \\ \mathbf{Y} \\ \mathbf{Z} \\ \mathbf{w} \end{bmatrix}_{4nX1} = [\mathbf{O}]_{4nX1} \qquad \text{(E.7)}$$

where,

$$\mathbf{M} = \mathbf{M_x} + \mathbf{M_y} + \mathbf{M_z} \tag{E.8}$$

$$\begin{aligned} \mathbf{M_x} &= \mathbf{B^T \bar{X}^2 B} - (\mathbf{B^T \bar{X} B})(\mathbf{B^T B})^{-1}(\mathbf{B^T \bar{X} B}) \\ \mathbf{M_y} &= \mathbf{B^T \bar{Y}^2 B} - (\mathbf{B^T \bar{Y} B})(\mathbf{B^T B})^{-1}(\mathbf{B^T \bar{Y} B}) \\ \mathbf{M_z} &= \mathbf{B^T \bar{Z}^2 B} - (\mathbf{B^T \bar{Z} B})(\mathbf{B^T B})^{-1}(\mathbf{B^T \bar{Z} B}) \end{aligned} \tag{E.9}$$

Hence, using Eq. (E.7), we can solve for the unknown homogeneous coordinates of control points (**X,Y,Z**) and the corresponding weights (**w**) for a given choice of number of control points (n).

REFERENCES

[1] Tuegel, E. J., Kobryn, P., Zweber, J. V., and Kolonay, R. M., 2017, "Digital Thread and Twin for Systems Engineering: Design to Retirement," 55th AIAA Aerospace Sciences Meeting, (January), pp. 1–26.

[2] Tuegel, E. J., Ingraffea, A. R., Eason, T. G., and Spottswood, S. M., 2011, "Reengineering Aircraft Structural Life Prediction Using a Digital Twin," International Journal of Aerospace Engineering, **2011**.

[3] Glaessgen, E. H., and Stargel, D. S., 2012, "The Digital Twin Paradigm for Future NASA and U.S. Air Force Vehicles," *53rd AIAA/ASME/ASCE/AHS/ASC Structures, Structural Dynamics and Materials Conference & 20th AIAA/ASME/AHS Adaptive Structures Conference 14th AIAA*, Honolulu, Hawaii, p. 1818.

[4] Grieves, M., and Vickers, J., 2017, "Digital Twin: Mitigating Unpredictable, Undesirable Emergent Behavior in Complex Systems," Transdisciplinary Perspectives on Complex Systems, pp. 85–113.

[5] Fuchs, H. O., Stephens, R. I., and Saunders, H., 1981, *Metal Fatigue in Engineering (1980)*.

[6] Findlay, S. J., and Harrison, N. D., 2002, "Why Aircraft Fail," Materials Today, **5**(11), pp. 18–25.

[7] Christodoulou, L., and Larsen, J. M., 2004, "Using Materials Prognosis to Maximize the Utilization Potential of Complex Mechanical Systems," JOM, **56**(3), pp. 15–19.

[8] National Research Council, 2008, *Integrated Computational Materials Engineering: A Transformational Discipline for Improved Competitiveness and National Security. National Academies Press*.

[9] Furrer, D. U., Dimiduk, D. M., Cotton, J. D., and Ward, C. H., 2017, "Making the Case for a Model-Based Definition of Engineering Materials," Integrating Materials and Manufacturing Innovation, **6**(3), pp. 249–263.

[10] Sangid, M., Matlik, J. F., Keskin, A., Thacker, B. H., Bichon, B. J., Ball, D. L., Engelstad, S. P., Ward, C., Venkatesh, V., Kim, H. A., Saraf, V., and Gorham, R., 2017, "Integrating ICME Practices into Design Systems and Structural Analysis," 55th AIAA Aerospace Sciences Meeting, (January), pp. 1–8.

[11] Ramalhete, P. S., Senos, A. M. R., and Aguiar, C., 2010, "Digital Tools for Material Selection in Product Design," Materials and Design, **31**(5), pp. 2275–2287.

[12] Arnold, S. M., Holland, F. A., Bednarcyk, B. A., and Pineda, E. J., 2015, "Combining Material and Model Pedigree Is Foundational to Making ICME a Reality," Integrating Materials and Manufacturing Innovation, **4**(1), pp. 37–62.

[13] Bolcavage, A., Brown, P. D., Cedoz, R., Cooper, N., Deaton, C., Hartman, D. R., Keskin, A., Ma, K., Matlik, J. F., Modgil, G., and Stillinger, J. D., 2014, "Integrated Computational Materials Engineering from a Gas Turbine Engine Perspective," Integrating Materials and Manufacturing Innovation, **3**(1), p. 13.

[14] Briggs, C., Brown, G. B., Siebenaler, D., Faoro, J., and Rowe, S., 2010, "Model-Based Definition," *AIAA/ASCE/AHS/ASC Structures, Structural Dynamics, and Materials Conference, 2010*, pp. 12–15.

[15] Ruemler, S. P., Zimmerman, K. E., Hartman, N. W., Hedberg, T., and Barnard Feeny, A., 2017, "Promoting Model-Based Definition to Establish a Complete Product Definition," Journal of Manufacturing Science and Engineering, Transactions of the ASME, **139**(5), pp. 1–7.

[16] Hedberg, T., Lubell, J., Fischer, L., Maggiano, L., and Feeney, A. B., 2016, "Testing the Digital Thread in Support of Model-Based Manufacturing and Inspection," Journal of Computing and Information Science in Engineering, **16**(2), pp. 1–10.

[17] Quintana, V., Rivest, L., Pellerin, R., Venne, F., and Kheddouci, F., 2010, "Will Model-Based Definition Replace Engineering Drawings throughout the Product Lifecycle? A Global Perspective from Aerospace Industry," Computers in Industry, **61**(5), pp. 497–508.

[18] Sangid, M. D., and Matlik, J. F., 2016, "A Better Way to Engineer Aerospace Components," Aerospace America, pp. 40–43.

[19] Qian, L., and Gero, J. S., 2010, "Function–Behavior–Structure Paths and Their Role in Analogy-Based Design," Artificial Intelligence for Engineering, Design, Analysis and Manufacturing, **10**(04), p. 289.

[20] Ruemler, S. P., Zimmerman, K. E., Hartman, N. W., Hedberg, T., and Barnard Feeny, A., 2016, "Promoting Model-Based Definition to Establish a Complete Product Definition," Journal of Manufacturing Science and Engineering, **139**(5), p. 051008.

[21] Hedberg, T., Lubell, J., Fischer, L., Maggiano, L., and Barnard Feeney, A., 2016, "Testing the Digital Thread in Support of Model-Based Manufacturing and Inspection," Journal of Computing and Information Science in Engineering, **16**(2), p. 021001.

[22] Gonzalez, C., 2016, "MachineDesign: What's the Difference Between Turbine Engines" [Online]. Available: www.machinedesign.com/motorsdrives/what-s-difference-between-turbine-engines.

[23] Gonzalez, C., 2016, "MachineDesign: What's the Difference Between Turbine Engines."

[24] Camba, J., and Contero, M., 2015, "Assessing the Impact of Geometric Design Intent Annotations on Parametric Model Alteration Activities . Computers in Industry . 71 : 35-45 . Copyright Elsevier," Computers in Industry, **71:35**–**45**, pp. 35–45.

[25] Feeney, A. B., Frechette, S. P., and Srinivasan, V., 2014, "A Portrait of an ISO STEP Tolerancing Standard as an Enabler of Smart Manufacturing Systems," Journal of Computing and Information Science in Engineering, **15**(2), p. 021005.

[26] Furrer, D. U., Dimiduk, D. M., Cotton, J. D., and Ward, C. H., 2017, "Making the Case for a Model-Based Definition of Engineering Materials," Integrating Materials and Manufacturing Innovation, **6**(3), pp. 249–263.

[27] Miller, A. M., Hartman, N. W., Feeney, A. B., and Zahner, J., 2017, "Towards Identifying the Elements of a Minimum Information Model for Use in Model-Based Definition," *Proceedings of ASME 2017 12th International Manufacturing Science and Engineering Conference MSEC2017*, Los Angeles, CA, USA.

[28] Hedberg, T., Feeney, A. B., Helu, M., and Camelio, J. A., 2017, "Toward a Lifecycle Information Framework and Technology in Manufacturing," Journal of Computing and Information Science in Engineering, **17**(2), pp. 1–13.

[29] Hedberg, T. D., Bajaj, M., and Camelio, J. A., 2020, "Using Graphs to Link Data Across the Product Lifecycle for Enabling Smart Manufacturing Digital Threads," Journal of Computing and Information Science in Engineering, **20**(1), pp. 1–15.

[30] Schleich, B., Anwer, N., Mathieu, L., and Wartzack, S., 2017, "Shaping the Digital Twin for Design and Production Engineering," CIRP Annals - Manufacturing Technology, **66**(1), pp. 141–144.

[31] Webster, G. A., and Ezeilo, A. N., 2001, "Residual Stress Distributions and Their Influence on Fatigue Lifetimes," International Journal of Fatigue, **23**(0), pp. 375–383.

[32] Withers, P. J., and Bhadeshia, H. K. D. H., 2001, "Residual Stress. Part 2 – Nature and Origins," Materials Science and Technology, **17**(4), pp. 366–375.

[33] Rolph, J., Preuss, M., Iqbal, N., Hofmann, M., Nikov, S., Hardy, M. C., Glavicic, M. G., Ramanathan, R., and Evans, A., 2012, "Residual Stress Evolution during Manufacture of Aerospace Forgings," *Superalloys 2012: 12th International Symposium on Superalloys*, pp. 881–891.

[34] Gayda, J., 2001, "The Effect of Heat Treatment on Residual Stress and Machining Distortions in Advanced Nickel Base Disk Alloys," NASA/TM-2001-210717, (January).

[35] Ma, K., Goetz, R., and Svrivatsa, S. K., 2010, "Modeling of Residual Stress and Machining Distortion in Aerospace Components," American Society for Metals (ASM) Handbook, **88**ABW-**2010**, pp. 1–41.

[36] "DEFORM, Software Package, Scientific Forming Technologies Corporation, Columbus, OH."

[37] Nelson, D., 1982, "Effects of Residual Stress on Fatigue Crack Propagation," Residual Stress Effects in Fatigue, ASTM STP 776, American Society for Testing and Materials, pp. 172–194.

[38] Lammi, C. J., and Lados, D. A., 2012, "Effects of Processing Residual Stresses on Fatigue Crack Growth Behavior of Structural Materials: Experimental Approaches and Microstructural Mechanisms," Metallurgical and Materials Transactions A, **43**(1), pp. 87–107.

[39] McClung, R., Enright, M., Liang, W., Chan, K., Moody, J., Wu, W.-T., Shankar, R., Luo, W., Oh, J., and Fitch, S., 2012, "Integration of Manufacturing Process Simulation with Probabilistic Damage Tolerance Analysis of Aircraft Engine Components," (April), pp. 1–13.

[40] Gabb, T. P., Kantzos, P. T., Telesman, J., Gayda, J., Sudbrack, C. K., and Palsa, B., 2011, "Fatigue Resistance of the Grain Size Transition Zone in a Dual Microstructure Superalloy Disk," International Journal of Fatigue, **33**(3), pp. 414–426.

[41] Gayda, J., Gabb, T. P., and Kantzos, P. T., 2004, "The Effect of Dual Microstructure Heat Treatment on an Advanced Nickel-Base Disk Alloy," Proceedings of the International Symposium on Superalloys, pp. 323–329.

[42] Mitchell, R. J., Lemsky, J. A., Ramanathan, R., Li, H. Y., Perkins, K. M., and Connor, L. D., 2008, "Process Development & Microstructure & Mechanical Property Evaluation of a Dual Microstructure Heat Treated Advanced Nickel Disc Alloy," Proceedings of the International Symposium on Superalloys, (Figure 1), pp. 347–356.

[43] Larsen, J. M., Jha, S. K., Szczepanski, C. J., Caton, M. J., John, R., Rosenberger, A. H., Buchanan, D. J., Golden, P. J., and Jira, J. R., 2013, "Reducing Uncertainty in Fatigue Life Limits of Turbine Engine Alloys," International Journal of Fatigue, **57**, pp. 103–112.

[44] Furrer, D. U., Shankar, R., and White, C., 2003, "Optimizing the Heat Treatment of Ni-Based Superalloy Turbine Discs," Jom, **55**(3), pp. 32–34.

[45] McDowell, D. L., and Dunne, F. P. E., 2010, "Microstructure-Sensitive Computational Modeling of Fatigue Crack Formation," International Journal of Fatigue, **32**(9), pp. 1521–1542.

[46] Anahid, M., Samal, M. K., and Ghosh, S., 2011, "Dwell Fatigue Crack Nucleation Model Based on Crystal Plasticity Finite Element Simulations of Polycrystalline Titanium Alloys," Journal of the Mechanics and Physics of Solids, **59**(10), pp. 2157–2176.

[47] Wan, V. V. C., Maclachlan, D. W., and Dunne, F. P. E., 2014, "A Stored Energy Criterion for Fatigue Crack Nucleation in Polycrystals," International Journal of Fatigue, **68**, pp. 90–102.

[48] Chen, B., Jiang, J., and Dunne, F. P. E., 2018, "Is Stored Energy Density the Primary Meso-Scale Mechanistic Driver for Fatigue Crack Nucleation?," International Journal of Plasticity, **101**(September 2017), pp. 213–229.

[49] Bandyopadhyay, R., Prithivirajan, V., Peralta, A. D., and Sangid, M. D., 2020, "Microstructure-Sensitive Critical Plastic Strain Energy Density Criterion for Fatigue Life Prediction across Various Loading Regimes," Proceedings of the Royal Society A: Mathematical, Physical and Engineering Sciences, **476**(2236).

[50] Bandyopadhyay, R., and Sangid, M. D., 2021, "A Probabilistic Fatigue Framework to Enable Location - Specific Lifing for Critical Thermo - Mechanical Engineering Applications," Integrating Materials and Manufacturing Innovation, (0123456789).

[51] Prithivirajan, V., and Sangid, M. D., 2020, “Examining Metrics for Fatigue Life Predictions of Additively Manufactured IN718 via Crystal Plasticity Modeling Including the Role of Simulation Volume and Microstructural Constraints,” Materials Science and Engineering A, **783**(March), p. 139312.

[52] Acko, B., McCarthy, M., Haertig, F., and Buchmeister, B., 2012, “Standards for Testing Freeform Measurement Capability of Optical and Tactile Coordinate Measuring Machines,” Measurement Science and Technology, **23**(9).

[53] Várady, T., Martin, R. R., and Cox, J., 1997, “Reverse Engineering of Geometric Models - An Introduction,” CAD Computer Aided Design, **29**(4), pp. 255–268.

[54] Kruth, J. P., and Kerstens, A., 1998, “Reverse Engineering Modelling of Free-Form Surfaces from Point Clouds Subject to Boundary Conditions,” Journal of Materials Processing Technology, **76**(1–3), pp. 120–127.

[55] Berger, M., Tagliasacchi, A., Seversky, L., Alliez, P., Levine, J., Sharf, A., Silva, C., Berger, M., Tagliasacchi, A., Seversky, L., Alliez, P., Guennebaud, G., and Sur-, A., 2016, “A Survey of Surface Reconstruction from Point Clouds To Cite This Version : HAL Id : Hal-01348404 A Survey of Surface Reconstruction from Point Clouds,” Computer Graphics Forum.

[56] Ma, W., and Kruth, J.-P., 1998, “NURBS Curve and Surface Fitting for Reverse Engineering,” The International Journal of Advanced Manufacturing Technology, pp. 918–927.

[57] Brujic, D., Ristic, M., and Ainsworth, I., 2002, “Measurement-Based Modification of NURBS Surfaces,” CAD Computer Aided Design, **34**(3), pp. 173–183.

[58] Miller, A. M. D., Alvarez, R., and Hartman, N., 2018, “Towards an Extended Model-Based Definition for the Digital Twin,” Computer-Aided Design and Applications, **15**(6), pp. 880–891.

[59] John, R., Larsen, J. M., Buchanan, D. J., and Ashbaugh, N. E., 2001, “Incorporating Residual Stresses in Life Prediction of Turbine Engine Disks,” Proceedings from NATO RTO (AVT) Symposium on Monitoring and Management of Gas Turbine Fleets for Extended Life and Reduced Costs, **079**(October), pp. 8–11.

[60] Enright, M.P., and Chan, K. S., 2004, “Extension of a Microstructure-Based Fatigue Crack Growth Model for Predicting Fatigue Life Variability,” ournal of ASTM International, **1**(No. 8, Paper JAI11566).

[61] Venkatesh, V., Green, R., O’Connell, J., Cernatescu, I., Goetz, R., Wong, T., Streich, B., Saraf, V., Glavicic, M., Slavik, D., Sampath, R., Sharp, A., Song, B., and Bocchini, P., 2018, “An ICME Framework for Incorporating Bulk Residual Stresses in Rotor Component Design,” Integrating Materials and Manufacturing Innovation, **7**(4), pp. 173–185.

[62] Cernatescu, I., Venkatesh, V., Glanovsky, J. L., Landry, L. H., Green, R. N., Street, M., and Hartford, E., 2015, “Residual Stress Measurements Implementation for Model Validation as Part of Foundational Engineering Problem Program on ICME of Bulk Residual Stress in Ni Rotors,” AIAA Journal Proceedings, SciTech Conference Proceedings 0387, (January), pp. 1–9.

[63] Cowles, B. A., Backman, D. G., and Dutton, R. E., 2015, “Update to Recommended Best Practice for Verification and Validation of ICME Methods and Models for Aerospace Applications,” Integrating Materials and Manufacturing Innovation, **4**(1), pp. 16–20.

[64] Cláudio, R. A., Branco, C. M., Gomes, E. C., and Byrne, J., 2002, “Life Prediction of a Gas Turbine Disc Using the Finite Element Method,” 8as Jornadas de Fractura, pp. 131–144.

[65] Cook, C. H., Spaeth, C. E., Hunter, D. T., and Hill, R. J., 1982, “Damage Tolerant Design of Turbine Engine Disks,” Proceedings of the ASME Turbo Expo, **5**.

[66] Irwin, G. R., 1957, “Analysis of Stresses and Strains Near the End of a Crack Traversing a Plate,” Journal of Applied Mechanics, **24**, pp. 361–364.

[67] Sangid, M. D., Stori, J. A., and Ferriera, P. M., 2010, “Process Characterization of Vibrostrengthening and Application to Fatigue Enhancement of Aluminum Aerospace Components—Part II: Process Visualization and Modeling,” The International Journal of Advanced Manufacturing Technology, **53**(5–8), pp. 561–575.

[68] James, L. A., and Mills, W. J., 1985, “Effect of Heat-Treatment and Heat-to-Heat Variations in the Fatigue-Crack Growth Response of Alloy 718,” Engineering Fracture Mechanics, **22**(5), pp. 797–817.

[69] Walker, K., 1970, “The Effect of Stress Ratio During Crack Propagation and Fatigue for 2024-T3 and 7075-T6 Aluminum,” Effects of Environment and Complex Load History on Fatigue LifeASTM International, 1970), 1-14. https://doi.org/10.1520/STP32032S.

[70] James, L. A., 1989, “Fatigue Crack Propagation in Alloy 718: A Review,” *Superalloy 718: Metallurgy and Applications*, Warrendale, PA, pp. 499–515.

[71] Glaessgen, E., and Stargel, D., 2012, “The Digital Twin Paradigm for Future NASA and U.S. Air Force Vehicles,” 53rd AIAA/ASME/ASCE/AHS/ASC Structures, Structural Dynamics and Materials Conference
20th AIAA/ASME/AHS Adaptive Structures Conference
14th AIAA, pp. 1–14.

[72] Annis, C. G., Cargill, J. S., Harris, J. A., and Van Wanderham, M. C., 1981, “Engine Component Retirement-for-Cause: A Nondestructive Evaluation (NDE) and Fracture Mechanics-Based Maintenance Concept,” JOM: Journal of The Minerals, Metals & Materials Society, **33**(7), pp. 24–28.

[73] Morse, E., Heysiattalab, S., Barnard-Feeney, A., and Hedberg, T., 2016, “Interoperability: Linking Design and Tolerancing with Metrology,” Procedia CIRP, **43**, pp. 13–16.

[74] “Siemens NX 12.0 CAD Documentation” [Online]. Available: https://docs.plm.automation.siemens.com/tdoc/nx/12/nx_help/#uid:index [Accessed date : October 2020].

[75] “MBDVidia 4.0 Software (Capvidia)” [Online]. Available: https://www.capvidia.com/products/mbdvidia [Accessed date : October 2020].

[76] 2020, *ISO 23952:2020 Automation Systems and Integration — Quality Information Framework (QIF) — An Integrated Model for Manufacturing Quality Information*, International Organization of Standardization (https://www.iso.org/standard/77461.html).

[77] Leach, P., Mealling, M., and Salz, R., 2005, “RFC 4122: A Universally Unique Identifier (UUID) URN Namespace.,” (https://www.ietf.org/rfc/rfc4122.txt).

[78] Bigot, P. A., 2014, “PyXB: Python XML Schema Bindings” [Online]. Available: http://pyxb.sourceforge.net/. [Accessed date : October 2020].

[79] Astheimer, R., Re, K. Del, Gopalakrishnan, S., Hartman, N., and Sangid, M., 2019, “Extending Model Based Definition to Capture Product Behavior and Contextual Information Using a Model Based Feature Information Network,” pp. 253–257.

[80] “Granta Design” [Online]. Available: https://www.grantadesign.com/industry/products/granta-mi/ [Accessed date : April 2nd 2020].

[81] “MSC MaterialCenter” [Online]. Available: https://www.mscsoftware.com/product/materialcenter [Accessed date : October 2020].

[82] “NASTRAN, Version 2016.0, MSC Software” [Online]. Available: http://www.mscsoftware.com/product/msc-nastran [Accessed date : October 2020].

[83] “PATRAN, Version 2016.0, MSC Software” [Online]. Available: http://www.mscsoftware.com/product/patran [Accessed date : October 2020].

[84] 2012, “Abaqus 6.12 Documentation - Simulia, Dassault Systemes. Providence, Rhode Island, US (2012).” [Online]. Available: http://130.149.89.49:2080/v6.12/index.html [Accessed date : October 2020].

[85] 2010, “ISO 10303-214, 2010. Industrial Automation Systems and Integration – Product Data Representation and Exchange – Part 214: Application Protocol: Core Data for Automotive Mechanical Design Process. International.”

[86] Li, W., Vairis, A., Preuss, M., and Ma, T., 2016, “Linear and Rotary Friction Welding Review,” International Materials Reviews, **61**(2), pp. 71–100.

[87] Turner, R., Gebelin, J. C., Ward, R. M., and Reed, R. C., 2011, “Linear Friction Welding of Ti-6Al-4V: Modelling and Validation,” Acta Materialia, **59**(10), pp. 3792–3803.

[88] Grujicic, M., Arakere, G., Pandurangan, B., Yen, C. F., and Cheeseman, B. A., 2012, “Process Modeling of Ti-6Al-4V Linear Friction Welding (LFW),” Journal of Materials Engineering and Performance, **21**(10), pp. 2011–2023.

[89] Bandyopadhyay, R., Rotella, J., Naragani, D., Park, J. S., Eff, M., and Sangid, M. D., 2019, “Residual Strain Analysis in Linear Friction Welds of Similar and Dissimilar Titanium Alloys Using Energy Dispersive X-Ray Diffraction,” Metallurgical and Materials Transactions A: Physical Metallurgy and Materials Science, **50**(2), pp. 704–718.

[90] Pan, Z., Shih, D. S., Tabei, A., Garmestani, H., and Liang, S. Y., 2017, “Modeling of Ti-6Al-4V Machining Force Considering Material Microstructure Evolution,” International Journal of Advanced Manufacturing Technology, **91**(5–8), pp. 2673–2680.

[91] Li, Y., Wang, H., and Gong, D., 2012, “The Interrelation of the Parameters in the Paris Equation of Fatigue Crack Growth,” Engineering Fracture Mechanics, **96**, pp. 500–509.

[92] Spasic, I., 2012, “Www.Grabcad.Com/Library/Blisk [Accessed : August 2019].”

[93] Johnson, G. R., and Cook, W. H., 1985, "Fracture Characteristics of Three Metals Subjected to Various Strains, Strain Rates, Temperatures and Pressures," Engineering Fracture Mechanics, **21**(1), pp. 31–48.

[94] Hall, E. O., 1951, "The Deformation and Ageing of Mild Steel: II Characteristics of the Lüders Deformation," Proceedings of the Physical Society. Section B, **64**(9), pp. 742–747.

[95] Petch, N. J., 1953, "The Cleavage Strength of Polycrystals.," The Journal of the Iron and Steel Institute, **173(5)**, pp. 25–28.

[96] Annis, C. G., VanWanderham, M. C., Harris, J. A., and Sims, D. L., 1980, "Gas Turbine Engine Disk Retirement-for-Cause: An Application of Fracture Mechanics and NDE," The American Society of Mechanical Engineers, **80-GT-127**.

[97] Pan, J., and Lin, S. H., 2005, "Fracture Mechanics and Fatigue Crack Propagation," *Fatigue Testing and Analysis*, Elsevier Inc., pp. 237–284.

[98] Kraft, E. M., 2016, "The Air Force Digital Thread/Digital Twin - Life Cycle Integration and Use of Computational and Experimental Knowledge," 54th AIAA Aerospace Sciences Meeting, (January), pp. 1–22.

[99] Lee, S. G., Ma, Y. S., Thimm, G. L., and Verstraeten, J., 2008, "Product Lifecycle Management in Aviation Maintenance, Repair and Overhaul," Computers in Industry, **59**(2–3), pp. 296–303.

[100] Gabb, T. P., Kantzos, P. T., Palsa, B., Telesman, J., Gayda, J., and Sudbrack, C. K., 2012, "Fatigue Failure Modes of the Grain Size Transition Zone in a Dual Microstructure Disk," Superalloys 2012, pp. 63–72.

[101] Gayda, J., and Furrer, D., 2003, "Dual Microstructure Heat Treatment.," Adv Mater Processes, **7**(36–9.).

[102] Gabb, T. P., Gayda, J., Telesman, J., and Kantzos, P. T., 2005, "Thermal and Mechanical Property Characterization of the Advanced Disk Alloy LSHR - Technical Memorandum," (June), p. 82.

[103] Collins, D. M., and Stone, H. J., 2014, "A Modelling Approach to Yield Strength Optimisation in a Nickel-Base Superalloy," International Journal of Plasticity, **54**, pp. 96–112.

[104] Groeber, M. A., and Jackson, M. A., 2014, "DREAM.3D: A Digital Representation Environment for the Analysis of Microstructure in 3D," **3**, p. 5.

[105] Prithivirajan, V., and Sangid, M. D., 2018, “The Role of Defects and Critical Pore Size Analysis in the Fatigue Response of Additively Manufactured IN718 via Crystal Plasticity,” Materials and Design, **150**, pp. 139–153.

[106] Physics, A., 1976, “Bounds and Self-Consistent Estimates for Creep of Polycrystalline Materials,” Proceedings of the Royal Society of London. A. Mathematical and Physical Sciences, **348**(1652), pp. 101–127.

[107] Mecking, H., and Kocks, U. F., 1981, “Kinetics of Flow and Strain-Hardening,” Acta Metallurgica, **29**(11), pp. 1865–1875.

[108] Kocks, U. F., and Mecking, H., 2003, “Physics and Phenomenology of Strain Hardening: The FCC Case,” Progress in Materials Science, **48**(3), pp. 171–273.

[109] Beyerlein, I. J., and Tomé, C. N., 2008, “A Dislocation-Based Constitutive Law for Pure Zr Including Temperature Effects,” International Journal of Plasticity, **24**(5), pp. 867–895.

[110] Cheng, J., Shahba, A., and Ghosh, S., 2016, “Stabilized Tetrahedral Elements for Crystal Plasticity Finite Element Analysis Overcoming Volumetric Locking,” Computational Mechanics, **57**(5), pp. 733–753.

[111] Boyce, D., Shade, P., Musinski, W., Obstalecki, M., Pagan, D., Bernier, J., and Turner, T., 2020, “Estimation of Anisotropic Elastic Moduli from High Energy X-Ray Data and Finite Element Simulations,” Materialia, **12**, p. 100795.

[112] Morrow, J., 1965, “Cyclic Plastic Strain Energy and Fatigue of Metals.,” *Internal Friction, Damping, and Cyclic Plasticity*, B. Lazan, ed., ASTM International, West Conshohocken, PA, pp. 45–87.

[113] Prithivirajan, V., Ravi, P., Naragani, D., and Sangid, M. D., 2021, “Direct Comparison of Microstructure-Sensitive Fatigue Crack Initiation via Crystal Plasticity Simulations and in Situ High-Energy X-Ray Experiments,” Materials and Design, **197**, p. 109216.

[114] Nicolas, A., Co, N. E. C., Burns, J. T., and Sangid, M. D., 2019, “Predicting Fatigue Crack Initiation from Coupled Microstructure and Corrosion Morphology Effects,” Engineering Fracture Mechanics, **220**(August), p. 106661.

[115] Sangid, M. D., Maier, H. J., and Sehitoglu, H., 2011, “An Energy-Based Microstructure Model to Account for Fatigue Scatter in Polycrystals,” Journal of the Mechanics and Physics of Solids, **59**(3), pp. 595–609.

[116] Thompson, A. W., and Backofen, W. A., 1971, “The Effect of Grain Size on Fatigue,” Acta Metallurgica, **19**(7), pp. 597–606.

[117] Thompson, A. W., 1971, “The Comparison of Yield and Fatigue Strength Dependence on Grain Size,” Scripta Metallurgica, **5**(10), pp. 859–863.

[118] Morrison, D. J., and Moosbrugger, J. C., 1997, “Effects of Grain Size on Cyclic Plasticity and Fatigue Crack Initiation in Nickel,” International Journal of Fatigue, **19**(SUPPL.1).

[119] Sangid, M. D., Maier, H. J., and Sehitoglu, H., 2011, “A Physically Based Fatigue Model for Prediction of Crack Initiation from Persistent Slip Bands in Polycrystals,” Acta Materialia, **59**(1), pp. 328–341.

[120] Johnson G.R., C. W. H., 1983, “A Constitutive Model and Data for Metals.Pdf,” Proceedings of the seventh international symposium, pp. 541–547.

[121] Bandyopadhyay, R., Prithivirajan, V., and Sangid, M. D., 2019, “Uncertainty Quantification in the Mechanical Response of Crystal Plasticity Simulations,” Jom, **71**(8), pp. 2612–2624.

[122] Kobryn, P., Tuegel, E., Zweber, J., and Kolonay, R., 2017, “Digital Thread and Twin for Systems Engineering: EMD To Disposal,” AIAA SciTech Forum - 55th AIAA Aerospace Sciences Meeting, (January), pp. 1–13.

[123] James, L. A., 1986, “The Effect of Grain Size upon the Fatigue-Crack Propagation Behavior of Alloy 718 under Hold-Time Cycling at Elevated Temperature,” Engineering Fracture Mechanics, **25**(3), pp. 305–314.

[124] Acharya, A., and Beaudoin, A. J., 2000, “Grain-Size Effect in Viscoplastic Polycrystals at Moderate Strains,” Journal of the Mechanics and Physics of Solids, **48**(10), pp. 2213–2230.

[125] Zhao, Y. F., Horst, J. A., Kramer, T. R., Rippey, W., and Brown, R. J., 2012, *Quality Information Framework - Integrating Metrology Processes*, IFAC.

[126] Maragakis I, 2009, *Bird Population Trends and Their Impact on Aviation Safety 1999-2008 (European Aviation Safety Agency)*.

[127] Shakal, C., 2013, “Https://Grabcad.Com/Library/High-Bypass-Fan-Conventional [Accessed : October 2020].”

[128] Piegl, L., and Tiller, W., 1996, “Algorithm for Approximate NURBS Skinning,” CAD Computer Aided Design, **28**(9), pp. 699–706.

[129] Lee, E. T. Y., 1989, “Choosing Nodes in Parametric Curve Interpolation,” Computer-Aided Design, **21**(6), pp. 363–370.

[130] Piegl, L., and Tiller, W., 1997, *The NURBS Book*, Springer.

[131] De Sá, J. P. M., 2007, *Applied Statistics Using SPSS, Statistica, MatLab and R.*, Springer Science & Business Media.

[132] Koch, K. R., 2010, "Three-Dimensional NURBS Surface Estimated by Lofting Method," International Journal of Advanced Manufacturing Technology, **49**(9–12), pp. 1059–1068.

[133] Rademaker, E. R., Sijtsma, P., and Tester, B. J., 2001, "Mode Detection with an Optimised Array in a Model Turbofan Engine Intake at Varying Shaft Speeds," 7th AIAA/CEAS Aeroacoustics Conference and Exhibit, (February 2019).

[134] Tabei, A., F. H. Abed, G. Z. Voyiadjis, and H. G., 2017, "Constitutive Modeling of Ti-6Al-4V at a Wide Range of Temperatures and Strain Rates.63 (2017): 128-135.," European Journal of Mechanics-A/Solids, **63**, pp. 128–136.

[135] Zhang, J. M., Zhang, Y., Xu, K. W., and Ji, V., 2007, "Anisotropic Elasticity in Hexagonal Crystals," Thin Solid Films, **515**(17), pp. 7020–7024.

[136] Kasemer, M., Quey, R., and Dawson, P., 2017, "The Influence of Mechanical Constraints Introduced by β Annealed Microstructures on the Yield Strength and Ductility of Ti-6Al-4V," Journal of the Mechanics and Physics of Solids, **103**, pp. 179–198.

[137] Kartal, M. E., 2013, "Analytical Solutions for Determining Residual Stresses in Two-Dimensional Domains Using the Contour Method," Proceedings of the Royal Society A: Mathematical, Physical and Engineering Sciences, **469**(2159).

[138] Bouchard, P. J., Budden, P. J., and Withers, P. J., 2012, "Fourier Basis for the Engineering Assessment of Cracks in Residual Stress Fields," Engineering Fracture Mechanics, **91**, pp. 37–50.

[139] Bandyopadhyay, R., and Sangid, M. D., 2019, "Crystal Plasticity Assessment of Inclusion- and Matrix-Driven Competing Failure Modes in a Nickel-Base Superalloy," Acta Materialia, **177**, pp. 20–34.

LIST OF PUBLICATIONS

1) S. Gopalakrishnan, S., N.W. Hartman, M.D. Sangid. "Integrating materials model-based definitions into design, manufacturing, and sustainment: a digital twin demonstration of incorporating residual stresses in the lifecycle analysis of a turbine disk." Journal of Computing and Information Science in Engineering 21, no. 2 (2021).

2) S. Gopalakrishnan, S., N.W. Hartman, M.D. Sangid. "Model-based feature information network (MFIN): a digital twin framework to integrate location-specific material behavior within component design, manufacturing, and performance analysis." Integrating Materials and Manufacturing Innovation 9, no. 4 (2020): 394-409.

3) S. Gopalakrishnan, S., N.W. Hartman, M.D. Sangid. “A digital engineering framework to facilitate automated data exchange between geometric inspection and structural analysis.” (2022) (Under review).

4) S. Gopalakrishnan, S., R. Bandyopadhyay, M.D. Sangid. “A framework to enable microstructure-sensitive location-specific fatigue life analysis of components and connectivity to the product lifecycle.” (2022) (Under review)